

Diss. ETH NO. 24790

**Morphology Control of Porous Polymeric Materials via Primary Particle
Architecture**

A thesis submitted to attain the degree of
DOCTOR OF SCIENCES of ETH ZURICH
(Dr. sc. ETH Zurich)

presented by

Alberto Cingolani

MSc. Chemical and Bioengineering, ETH Zurich

born on 16.01.1990

citizen of Italy

Accepted on the recommendation of
Prof Dr. Massimo Morbidelli, examiner
Prof Dr. Lucio Isa, co-examiner

2017

Summary

Since its development by Marti et al. in 2005, Reactive Gelation established itself as a robust and efficient method to produce porous polymeric materials suitable for different applications, allowing high control of the final morphology. In this technique, colloidal polymer nanoparticles (in form of latex) swollen with additional monomer and initiator are destabilized and aggregated in a controlled way, forming a porous network. Afterwards, a post post-polymerization step is carried out, providing mechanical stability to the structure. Playing with the aggregation kinetics and regime (electrolyte addition or shear-induced) enables the production of porous polymers in different forms, such as monoliths, particles and hollow shells. As the primary nanoparticles are the building blocks of these porous materials, the major aim of the thesis was to explore the effect of their features on the resulting framework. Indeed, as soon as they exhibit complex characteristics, such as advanced functionality and composition or core/shell architecture, the final resulting porous structure and its characteristics are affected.

In the first part of the work, the study has been focused on polymeric monoliths produced via stagnant aggregation. The effect of the primary particle characteristics, namely the core-shell architecture and the initial solid content of the latex, on the properties of the final materials was investigated using two different sizes of nanoparticles. It was found that the first parameter affects the pore size distribution in the small range (0.01 to 1 μm) whereas the second one allows a precise tuning of the pores in the larger range (1 to several μm), independently of the primary particle size. As a result, rigid and mechanically stable monoliths with very well-defined pore structures and pore size distributions have been obtained.

In the second part, a simple method for producing highly porous materials suitable for chromatographic applications was developed taking advantage of shear-induced aggregation. Thanks to their fractal geometry, these aggregates exhibit highly porous structures, with uniform pore size distribution ranging from 0.1 to several micrometers. Once again, particle architecture, namely the ratio between the hard, highly crosslinked core and the soft, poorly crosslinked shell, resulted to be the most important parameter to be tuned in order to obtain highly porous and mechanically resistant clusters. In comparison to other commercial stationary phases, the final materials showed, not only much lower pressure drops at very high flow rates, but also HETP profiles independent of fluid velocity. Since the contribution of convection to internal transport dominates at all flow rates this novel class of materials has been named as Ultra-Perfusive.

In the third part of the work, Reactive Gelation was combined with microfluidics in order to produce monodisperse, rigid hollow spheres with tunable porosity of the crust, taking advantage of a peculiar self-organization of the primary nanoparticles in a jammed state. A possible explanation of the physical mechanism controlling the aforementioned behavior is also presented with a simplified model at atomic scale, by means of molecular dynamics simulations. The identification of the nature of the process, enabled the access to capsules with rather open or compact shells, playing with the solid dry content of the initial nanoparticles latex. Furthermore, this last parameter was correlated with the capsules accessibility by tracking intra-particle diffusion of probe fluorescent molecules.

In the last part of the work, experiments with *ad-hoc* polymer colloidal particles have been devised with the specific objective of highlighting material transfer and clarifying the role of the softness of the particle surface during aggregation under shear. To achieve this goal, polymer particles with a core-shell structure comprising of fluorescent groups have been prepared. This way, the surface softness could be tuned by addition of monomer acting as plasticizer and the percentage of fluorescent particles could be recorded over time via confocal microscopy. For the first time, material exchange occurring on the soft surface of

the core-shell polymer micro-particles upon aggregation under shear was observed and proved. More aptly, starting from a 50% labelled/not labelled mixture, an increase in the percentage of particles showing a fluorescent signature was recorded over time, reaching after 5 hours a fraction of 70%

Sommario

Fin dal suo sviluppo ad opera di Marti *et al.* nel 2005, la tecnica della “Reactive Gelation” si è affermata come metodo robusto ed efficiente per produrre materiali polimerici porosi, impiegabili in molteplici settori, grazie al facile ed accurato controllo sulla loro morfologia. Secondo questa procedura, nanoparticelle colloidali di polimero (in forma di lattice) vengono rigonfiate di monomero ed iniziatore aggiuntivi e aggregate in maniera controllata. In questo modo si genera un reticolo polimerico interconnesso, i cui spazi interstiziali costituiscono delle porosità. Successivamente, si procede con una postpolimerizzazione che fissa la struttura e ne garantisce la stabilità meccanica. Grande versatilità nell'apparenza e nella forma finale dei materiali porosi è garantita dai diversi meccanismi e cinetiche di aggregazione (elettrostatica o sotto sforzo di taglio), che permettono una differenziazione dei derivati in monoliti, corpuscoli e gusci cavi. Poiché le nanoparticelle primarie sono gli effettivi blocchi costitutivi di questi materiali porosi, il focus principale di questo lavoro di tesi è stato posto sullo studio sistematico degli effetti delle loro proprietà sulla morfologia finale dei prodotti. Difatti, le precedenti caratteristiche complesse, come funzionalità superficiali e composizione differenziata nucleo/guscio (detta anche architettura “core/shell”), si riflettono direttamente nella morfologia della macrostruttura porosa ottenuta. Nella prima parte del lavoro, ci si è concentrati sulla produzione di monoliti tramite aggregazione stagnante. In particolare, due diverse dimensioni di particelle sono state impiegate per studiare l'effetto sui successivi prodotti delle caratteristiche della dispersione colloidale originaria, rappresentate dall'architettura “core/shell” e dal contenuto di solido iniziale. Si è riscontrato che il primo parametro

determina la distribuzione dei pori sulla piccola scala (da 0.01 – fino a 1 μm) mentre il secondo permette un preciso controllo su scale più grandi (da 1 fino a parecchi micrometri), indipendentemente dalla dimensione iniziale delle particelle. Di conseguenza, è stato possibile ottenere monoliti rigidi e meccanicamente stabili con un preciso controllo della loro distribuzione dei pori.

Nella seconda parte, una metodologia innovativa ma semplice per produrre materiali cromatografici altamente porosi è stata sviluppata controllando un'aggregazione sotto sforzo di taglio. Gli aggregati generati, sotto forma di corpuscoli, in dipendenza della loro organizzazione frattale, presentano una struttura altamente porosa, con ampia distribuzione di pori, che si articola da 0.1 a parecchi micrometri. Come nel caso precedente, l'architettura delle nanoparticelle primarie, quantificato nel rapporto tra le dimensioni di un nucleo duro e reticolato ("core") e quelle di un rivestimento più plastico ("shell") è risultata essere il parametro più importante per ottenere materiali altamente porosi e meccanicamente stabili. Il prodotto finale, rispetto ad altri analoghi commerciali, è risultato in grado non solo di presentare, perdite di carico nettamente inferiori ad alti flussi, ma anche profili di HETP ("height equivalent to theoretical plate") indipendenti dalla velocità lineare. Poiché il contributo convettivo al trasporto interno di materia è risultato dominante in qualsiasi regime, si è deciso di assegnare questi materiali ad una nuova classe, attraverso la denominazione di Ultra-Perfusivi.

Nella terza parte del lavoro, la tecnica della Reactive Gelation è stata combinata con alcune conoscenze di microfluidica per produrre sfere monodisperse, rigide ma al contempo cave e controllarne la porosità della crosta superficiale. Il principio si basa sulla spontanea tendenza delle nanoparticelle primarie ad arrangiarsi, con disposizione disordinata, in uno stato simil-solido con geometria a guscio sferico. Inoltre, attraverso l'utilizzo di simulazioni di dinamica molecolare, si è cercato di individuare una possibile spiegazione eziologica per il suddetto comportamento. L'identificazione, almeno parziale, del meccanismo responsabile del processo, ha permesso di accedere a gusci più o meno compatti e/o porosi, attraverso la regolazione del contenuto iniziale di solido nel lattice.

Nell'ultima parte del lavoro, con l'intenzione di chiarificare il ruolo della plasticità superficiale delle particelle durante aggregazione sotto sforzo di taglio, è stato sviluppato un metodo per rilevare lo scambio di materiale superficiale tra diverse particelle polimeriche sintetizzate *ad hoc*, con architettura "core/shell" e marcatura con componenti fluorescenti. Le precedenti caratteristiche permettono di variare la plasticità superficiale delle particelle, rigonfiandone il guscio con monomero addizionale, e tracciare gli elementi fluorescenti attraverso l'osservazione con un microscopio confocale. In questo modo è stato possibile, per la prima volta, rilevare e provare lo scambio di materia durante aggregazione sotto sforzo di taglio, per particelle polimeriche con superficie sufficientemente plastica. Nello specifico, a partire da una dispersione inizialmente composta da particelle di cui solo il 50% risultava marcato fluorescente, si è osservato un incremento di quest'ultima percentuale fino al 70% dopo cinque ore di aggregazione sotto sforzo di taglio.

Acknowledgments

This thesis is the result of roughly three years of hard work. Of course, such a huge effort could not have been achieved alone and therefore it is important to mention and thank here the people that directly or indirectly contributed to it.

First of all, I would like to thank Professor Morbidelli, not only for offering me a PhD position in his group in Zurich, but also for convincing me in taking this opportunity as a personal challenge in the frame of my future career, though my initial hesitation.

The second person that I would definitely like to thank is Professor Storti, with whom I interacted basically every day over this last years. His constant support and endless patience have been extremely important and helped me in facing all the issues that occurred during my PhD. I can certainly say that thanks to his supervision I managed to develop unique skills that I will always bring with myself.

A special thanks goes also to my “added” supervisor Dr. Hua Wu and his advice in many situations. I always appreciated the possibility of just dropping by his office and ask very difficult questions.

Another special thanks goes again to my other “added” supervisor Dr. Alessandro Buttè, with whom we “customized” the chemical engineering thermodynamic course at ETH and have always found nice topic of discussions, beside science.

The list of added supervisors would not be complete without mentioning at least other four people: Marco Lattuada, Davide Moscatelli, Paolo Arosio and Stavros Stavrakis. The possibility of interacting with them directly and discuss day by day scientific as well as personal issues will never be acknowledged enough. Certainly, a major part of my growth as a scientist as well as a person is dependent on them.

Last but not least, another great thanks goes to my co-advisor Prof. Lucio Isa for the careful revision of this thesis and the nice inputs and discussions.

Of course, there are many other people that I would like to thank: I will try to more or less group them, to make it more appropriately.

I will start with the easiest category to nominate: the students. Therefore, I would like to thank: Stefano, Marc, Jonas, Abi, Carolina and Oliver. It was a great pleasure to supervise all of you (some more and some less) and the results shown in this thesis will not be possible without your effort.

I will move further with the colleagues: Marcel, Daniel, Lu, Antoine, Anna, Denise, Nicole, Sebastian, Peter, Paula, Tianjin, Iannis, Baptiste (who taught me mostly everything), Delong, Xinxin, Jichang, David H., Ivo, Richard B., Fulvio, Miriam, the whole Morbidelli Group, the whole De Mello Group, the whole Mazzotti Group and the whole Arosio Group. Moreover, I have to certainly thank Christine for all the advice over this years. I am also really thankful to Annette Röthlisberger, Marion Rothaupt and Michael Plötze for the help with Hg intrusion measurements.

I will go on with other friends: Marco B., Alessandro F., Lauriane, Michele, Matteo, Vasco, Leonardo, Nicolò and Amin. A special mention goes to John and Eugenio for their endless support and for being always present in the difficult moments. Another special mention goes to Giuseppe for having shared very special “diners”. A thanks goes also to all the friends of ZIGSS, with whom, I hope, we have started something very important for the future years.

L'ultima categoria è certamente quella degli amici italiani (o italofofi) con i quali ho condiviso praticamente tutto il mio percorso di dottorato. Un grazie speciale va a Claudio, Stefano, Ruben, Luca C., Luca D., Danilo e Simone. Dei ringraziamenti speciali sono sicuramente dovuti a Raffaele per tutto quello che mi ha insegnato, fin dalla prima supervisione a Milano, e certamente a Tommaso ed Ernesto per i momenti colmi di contributi eccellenti.

Ringrazio infine anche la mia famiglia per il grande supporto durante tutti questi anni.

Table of Content

Summary	I
Sommario	IV
Acknowledgments.....	VII
Table of Content.....	IX
Chapter 1 Introduction	1
1.1 Colloidal Systems and Aggregation Phenomena	1
1.1.1 Stagnant Aggregation.....	4
1.1.2 Shear-Induced Aggregation	5
1.1.3 Self-assembly and Other Aggregation Methods	7
1.2 Colloidal Approach for the Synthesis of Porous Polymer: The Reactive Gelation Process and its Application.....	9
1.3 Synthesis of Functional Nanoparticles: Surface Features and Core/Shell Architecture	11
1.4 Characterization of Porous Materials.....	13
1.4.1 Light Scattering Techniques	14
1.4.2 Intrusion and Adsorption Methods	15
1.4.3 Chromatography	18
1.4.4 Microscopy	19
1.5 Aim and Outline of the Present Work.....	21

Chapter 2 Control of Pore Structure in Polymeric Monoliths Prepared from Colloidal Dispersions.....	22
2.1 Introduction.....	22
2.2 Experimental.....	24
2.2.1 Materials.....	24
2.2.2 Reactive Gelation.....	24
2.2.3 Monolith Characterization.....	26
2.3. Result and Discussion.....	27
2.3.1 The Reactive Gelation Process.....	27
2.3.2 Effect of Particle Architecture.....	28
2.3.3 Effect of initial dry content.....	37
2.4. Conclusion.....	40
Chapter 3 Preparation of Ultra-Perfusible Chromatographic Materials via Shear-Induced Reactive Gelation.....	42
3.1 Introduction.....	42
3.2 Experimental.....	45
3.2.1 Materials.....	45
3.2.2 Synthesis of the Primary Particles.....	45
3.2.3 Reactive Gelation.....	47
3.2.4 Packing.....	48
3.2.5 Product Characterization.....	49

3.3 Results and Discussion	51
3.3.1 Production of Porous Materials	51
3.3.2 Structure Characterization.....	52
3.3.3 Chromatographic Characterization	59
3.4 Conclusion	62
Chapter 4 Synthesis of Monodisperse, Porous, Rigid, Hollow and Spherical Polymeric Capsules Combining Microfluidics and Reactive Gelation	64
4.1 Introduction.....	64
4.2 Experimental	66
4.2.1 Materials.....	66
4.2.2 Emulsion Polymerization.....	67
4.2.3 Capsules Formation	69
4.2.4 Capsules Characterization.....	72
4.2.5 Simplified Model for Individual Primary NPs.....	74
4.3 Results and Discussion	74
4.3.1 Preparation of Porous Capsules	74
4.3.2 Computational Study of the Ether-SDS Interaction.....	79
4.3.3 Particles Features	82
4.4 Conclusions.....	85
Chapter 5 Tracking of Fluorescently Labeled Polymer Particles Reveals Surface Effects during Shear- controlled Aggregation	87

5.1 Introduction.....	87
5.2 Experimental	89
5.2.1 Materials.....	89
5.2.2 Synthesis of Colloidal Core-Shell Polymer Nano-particles.....	90
5.2.3 Synthesis and Purification of Rhodamine B - HEMA Precursor.....	93
5.2.4 Synthesis of Core-Shell Polymer Micro-particles	93
5.2.5 Processing of the Particles	95
5.2.6 Characterization Methods	96
5.3. Results and Discussion	97
5.3.1 Shear-controlled Aggregation.....	97
5.3.2 Aggregation of Nano-particles.....	98
5.3.3 Aggregation of Micro-particles.....	100
5.4. Conclusion	105
Chapter 6 Conclusions	107
Appendices.....	112
Appendix A - Chapter 2.....	113
Appendix B - Chapter 3	120
Appendix C - Chapter 4	124
References.....	145
Curriculum Vitae.....	156

Publications.....	157
Conferences.....	158

Chapter 1

Introduction

1.1 Colloidal Systems and Aggregation Phenomena

A colloidal system is defined as an heterogeneous mixture in which one phase is uniformly distributed or dispersed into another in a finely divided state, generally in the form of nano or micron sized particles¹. Four major types of interactive forces acting within them can be identified:² hard sphere, steric, soft (electrostatic) and van der Waals. Hard spheres interactions, which are repulsive, are not commonly encountered and become significant only when particles approach each other at distances slightly less than twice the hard sphere radius. Steric interactions are caused by macromolecules protruding from the particles surface that start interacting when they overlap¹. The soft (electrostatic) and van der Waals interparticle forces are described in the well-established theory developed independently by Derjaguin and Landau³ and Verwey and Overbeek⁴ in 1941, known as DLVO Theory, in which a balance between repulsive and attractive potential energies of interaction of the dispersed particles is assumed. Repulsive interactions are due either to the similarly charged electrical double layers surrounding the particles or to particle-solvent interactions. Attractive interactions are due mainly to the van der Waals forces between the particles. In order to obtain a stable dispersion and avoid particles aggregation, the repulsive interactions must overcome the attractive ones; on the other hand, to make them aggregate, the opposite

condition must be achieved. The total potential energy of interaction V_{tot} is the sum of the potential energy of attraction V_A and that of repulsion V_R :

$$V_{tot} = V_A + V_R \quad (1)$$

The potential energy of attraction in vacuum for similar spherical particles of radius a , whose centers are separated by a distance R is given by the expression (Hamaker 1937)⁵:

$$V_A = \frac{-Aa}{12h} \quad (2)$$

where A is the Hamaker constant and h is the nearest distance between the surfaces of the particles ($R = 2a$) when h is small ($R/a \leq 5$). The attractive potential energy is always negative because its value at infinity is zero and decreases as the particles approach each other. The potential energy of repulsion V_R depends on the size and shape of the dispersed particles, the distance between them, their surface potential ψ_0 , the dielectric constant ϵ_r of the dispersing liquid and the effectiveness thickness of the electrical double layer $1/\kappa$, where

$$\frac{1}{\kappa} = \left(\frac{\epsilon_r \epsilon_0}{4\pi F^2 \sum_i c_i z_i^2} \right)^{\frac{1}{2}} \quad (3)$$

For two spherical small particles and a relatively thick electrical double layer (Lyklema, 1968)⁶:

$$V_R = \frac{\epsilon_r a^2 \psi_0^2}{R} e^{-\kappa h} \quad (4)$$

For large particles and a relatively thin electrical double layer ⁶:

$$V_R = \frac{\epsilon_r a \psi_0^2}{2} \ln(1 + e^{-\kappa h}) \quad (5)$$

The potential energy of repulsion is always positive, since its value at infinity is zero and increases as the particles approach each other. Thus, for a general colloidal dispersion a situation as the one described in Figure 1.1 is obtained. As it can be seen, in order to have a positive force towards aggregation, an energy barrier has to be overcome. If the kinetic energy of the particles is not sufficient, repulsion prevails. On the other hand, when the kinetic energy is high enough, aggregation occurs and, due to the

strong attractive forces, this process is considered to be irreversible. The bonding between aggregated particles, in fact, is typically located in the deep well of interaction potential and therefore it is very hard to overcome the disaggregation energy barrier. The energy barrier can be reduced through addition of an electrolyte that screens the repulsive electrostatic forces, allowing effective aggregation between two particles upon collision due to Brownian motions, or by increasing the kinetic energy of the system (e.g. by stirring or applying high shear).

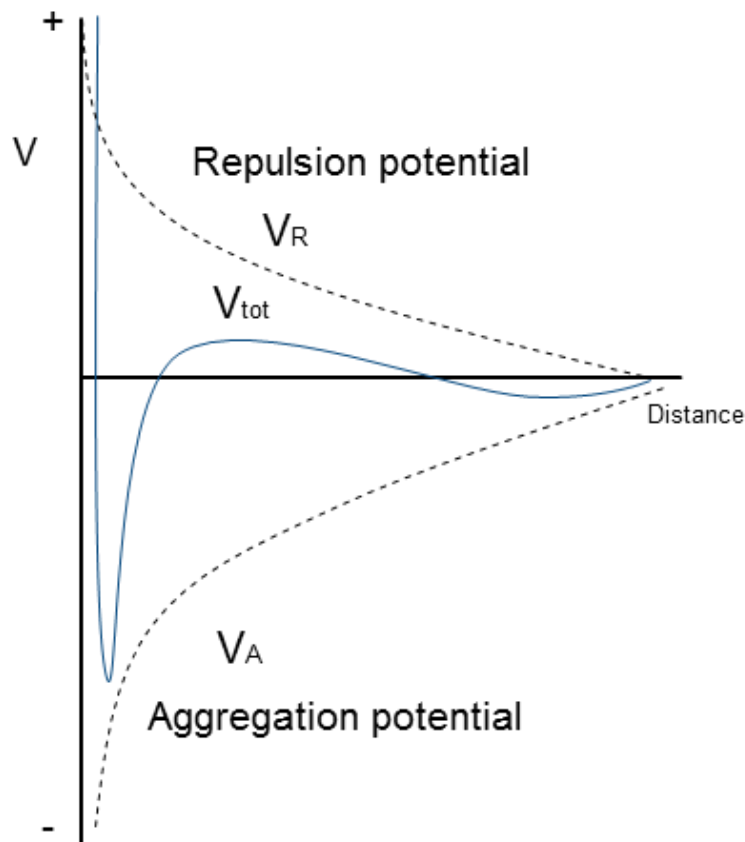


Figure 1.1. Total potential energy diagram according to DLVO Theory¹.

The investigation of these phenomena was pioneered by Smoluchowski^{7,8} at the beginning of twentieth century, who successfully proposed the first quantitative model for describing the aggregation of spherical particles in fully destabilized systems. Afterwards, Fuchs⁹ included the effect of interparticle (mainly repulsive) interaction in the Smoluchowski model, which resulted in a correction term in the

expression for the rate constant, the so-called Fuchs stability ratio W , defined as the ratio of the rate constants in the absence and presence of an energy barrier, respectively. From theoretical considerations, $\log(W)$ has been shown (Fuchs, 1934⁹; Reerink and Overbeek, 1954¹⁰) to be approximately linear function of the log of the concentration of the electrolyte in the liquid phase during the initial phase of slow coagulation at constant surface potential. Values of W are usually calculated by determining the particle concentration over time either by counting directly the particles via microscopy¹¹, measuring optical density changes using a spectrophotometer¹² or through the simultaneous use of static and dynamic light scattering¹³. In the eighties, Forrest and Witten¹⁴ realized that large clusters formed during aggregation processes can be considered as fractal object. Thank to this concept, their description can be done using a simple power law expression that correlates the mass of the cluster to its size. The corresponding exponent, referred to as the fractal dimension, indicates substantially how open or how compact the structure of the cluster is. For a fractal object, its mass, i , with respect to its radius, R , follows the scaling $i \sim R^{d_f}$, where d_f is the fractal dimension, with a value between 1 and 3, where 1 represent a linear alignment of particles and 3 a fully coalesced sphere.

1.1.1 Stagnant Aggregation

Under stagnant condition, colloidal aggregation can be classified into two classes, characterized with universal features, based on the interaction energy barrier between particles¹⁵. Generally, this last condition is defined by the amount of added electrolyte. In this sense, a critical coagulation concentration (ccc) which represents the minimum concentration of electrolyte leading to a zero energy barrier is defined¹. When no interaction energy barrier is present, the colloidal particles are completely destabilized, and the aggregation takes place upon every collision occurring because of Brownian motion. This means that the rate of the aggregation is fully controlled by the particle diffusion rate within the media. This kind of aggregation is referred to as diffusion-limited cluster aggregation (DLCA)¹⁵. In the

case of presence of a small interaction energy barrier, only a small fraction of collisions results in successful aggregation, and the aggregation rate is significantly slower with respect to the DLCA process. Thus, it is called reaction-limited cluster aggregation (RLCA)¹⁵. The classical d_f value of DLCA clusters is always in the range between 1.75 and 1.85, independently of the materials of the particles and electrolytes, while that of the RLCA clusters is in the range between 1.9 and 2.2. Thus, the RLCA clusters are more compact with respect to the DLCA ones. When the aggregation of colloidal particles is carried out at relatively high particle volume fractions, since the growth of the clusters follows the fractal scaling and the density of the clusters decreases as the size increases, at a certain degree of aggregation the available space would be fully occupied by the clusters¹⁶. At some point they will start interconnecting, until they will percolate, forming a solid network in a jammed, disordered arrested state. This moment is therefore named arrest time and the overall process is referred to as colloidal gelation. The formed solid-like state is called a gel. A precise control on this aforementioned dynamic arrest, specifically on the final resulting structure after the percolation is a fundamental issue in soft matter physics¹⁶⁻¹⁸. Indeed, as gels behave similarly to a solid but with a very low dry volume content, they are extremely valuable for the development of novel and functional porous materials¹⁹⁻²³.

1.1.2 Shear-Induced Aggregation

In the presence of shear, even in the case of no energy barrier, the aggregation process is not only driven by Brownian motion but it is also controlled by the entity of the shear. Indeed, it is a common observation that coagulation rates are influenced by the stirring of the suspension, as particles are thrown together at rates much greater than a normal diffusion rate¹. Therefore, shear-flow has a strong accelerating effect on the aggregation kinetics. Moreover, even for colloidal systems that are well stabilized by electrostatic repulsive forces²⁴, monodisperse and in quasi-equilibrium, application of shear might lead to non-trivial clustering phenomena and gelation transition dominated by the complex interplay between DLVO

interactions and shear flow^{21,25,26}. In addition, also the morphology and the size of the formed clusters are considerably affected, as the imposed high shear is able to break the clusters²⁷ and to induce rearrangements generally leading to more compact structures^{25,28,29}. Indeed, during processes involving aggregation and breakage, the cluster size evolution is regulated by two key non-dimensional quantities, the Peclet number (Pe) and the Fragmentation number (Fa)³⁰. Pe represents the ratio of the convective transport rate (i.e. the shear) and the diffusive transport rate (generally represented by the particles thermal energy). Fa describes the ratio of the viscous shear stress to the strength of the clusters.

$$Pe_{i,j} = \frac{3\pi\eta_c\dot{\gamma}R_iR_j(R_i+R_j)}{2k_B T} \quad (6)$$

$$Fa = \frac{\eta_c\dot{\gamma}}{T_{S,j}} \quad (7)$$

where η_c is the viscosity of the continuous phase, $\dot{\gamma}$ is the shear rate, R_i the radius of the i -sized cluster, k_B the Boltzmann constant and $T_{S,j}$ the characteristic cohesive strength of the aggregate. This last parameter is generally inversely proportional to the cluster radius, in dependence on the fracture mechanism. From their expression, it is possible to notice that two main parameters influence both the Pe number and the Fa number: the shear rate and the cluster radius. Accordingly, the interplay between aggregation and breakage in shear depends strongly on them and, consequently, also the resulting cluster d_f ²⁸. Moreover, depending on the strength of electrostatic repulsion among particles, the rate of aggregation between small clusters might be insensitive to shear and dominated by repulsion as in a reaction-limited aggregation process. On the contrary, the aggregation of large clusters is insensitive to repulsive interaction and is purely controlled by shear²⁵.

Similar to the gelation process under stagnant conditions, shear driven gelation can also occur when the aggregation reaches a degree at which the generated fractal clusters can fill the whole available space and percolate¹⁶. Shear-driven, self-accelerating aggregation kinetics can be well applied to explain the jamming phenomena of well-stabilized colloidal systems activated by shear in concentrated condition.

At the colloid-particle level, these systems have a unique behavior. As long as the shear forces are not providing sufficient energy to overcome the barrier, the presence of repulsive interaction stabilizes the particles. On the other hand, above that point, the aggregation rate raises up to very high levels, comparable to those of fully destabilized particles. This peculiar effect, which has been addressed both theoretically and experimentally²⁵, manifests itself with an explosive-like, runaway behavior in the growth rate of the cluster size²⁵. At that point, also the breakage effect becomes not negligible anymore and affects the gelation process as well. In general, a description of the criticalities for shear-induced gelation to happen can be expressed in the definition of breakage number, written as³¹:

$$Br = \frac{\eta_c \dot{\gamma} R_p}{V_b} \quad (8)$$

where η_c is the viscosity of the continuous medium, $\dot{\gamma}$ the shear rate, R_p the primary particle radius and V_b the difference in potentials at the primary minimum and the energy barrier. It represents the ratio between the shearing energy and the interparticle bonding energy. The critical volume fraction for gelation to happen is a function of the primary particle radius and of the shear rate. Moreover, the radius of gyration of clusters constructing the gel network and the primary particle radius at criticality decreases as Br increases, following a power law.

1.1.3 Self-assembly and Other Aggregation Methods

Apart from classical colloidal gels, other solid-like structures can be obtained thanks to the self-assembly of colloidal particles into highly ordered and organized systems^{32–34}. In these processes, the driving force is generally a local interaction among the components themselves, without any external influence. Therefore, they occur in a spontaneous way, as a result of the reduction of the system's free energy. Classical examples are colloidal crystals³³ and particles adsorbing at fluid-fluid interface³⁵. These phenomena are also very useful for the production of micro and nanostructured materials^{36–40}.

Colloidal crystals are formed when particles self-organize into periodic arrays and regular arrangements. They have been first identified and described by Stanley in the first half of the last century by observation of the ordered and repetitive structures formed by certain tobacco and tomato viruses^{41,42}. Moreover, particles self-organization might also be forced with external action such as capillary forces due to evaporation of the dispersion media⁴³, phase separation⁴⁴ or solvent removal⁴⁵. Bulk properties of the colloidal crystals depend on composition, particle size, packing arrangements and degree of regularity^{40,46}. In general, these structures, both in the bulk or supra-spheres form, might act as natural diffraction gradient for incident light, making these systems of utmost interest in optics and photonics⁴⁵. Assembly and trapping of solid particles at a fluid-fluid interface is in general driven by the reduction of total surface area⁴⁷. When a particle of radius a goes at the oil-water interface, it reduces the interfacial surface area of a value equal to its cross-section and at the same time it generates two solid-water and solid-oil interfaces, with an actual free energy reduction. This way, particles are bound at the interface, since the trapping energy is much higher than the thermal kinetic energy, $k_B T$, where k_B is the Boltzmann constant and T the temperature. The major related phenomenon is the one of Pickering emulsion³⁵, in which solid colloidal particles stabilize emulsion by displacing at the interface of the droplets of the dispersed phase. Particle wetting properties are of high importance: hydrophilic colloids stabilize water continuous (oil-in-water) emulsions, while water-in-oil emulsions are better stabilized by oil-wettable ones^{47,48}. Due to their specific arrangement, particles adsorbed on the surface of a droplet offers a valuable template^{49,50} for the production of hollow microcapsules and shells, often referred to as colloidosomes⁵¹. Generally, quite ordered, homogeneous layers are observed, provided that the concentration of the particles is low enough. On the other hand, when the particles adsorb at interface with enough high concentration, interfacial jamming^{52,53} might occur and more irregular surface morphologies have been recorded. In this sense, also promoted capture of the particles on fluid droplets, induced via the dispersed phase flow, generates jammed shells. In those systems, surface tension provides two-

dimensional isotropic compressive stress and as a result shear-induced liquid-to-solid transition is observed⁵⁴.

Other unconventional gel-like networks can be generated by capillary forces, resulting after addition of a small amount of secondary fluid, immiscible to the continuous phase of the colloidal suspension⁵⁵.

Moreover, another very interesting example to mention is the one of bicontinuous interfacially jammed emulsion or simply bijels⁵⁶, hypothesized and then experimentally obtained by Clegg and Cates in 2005, which are interpenetrating, continuous domains of two immiscible fluids, maintained in a rigid state by a jammed layer of colloidal particles at their interface.

1.2 Colloidal Approach for the Synthesis of Porous Polymer: The Reactive Gelation Process and its Application

In the frame of what has been previously discussed, the colloidal approach represents a strong and versatile method to obtain porous polymeric materials, since solid-like networks with extremely low dry content can be achieved from the initial suspension. On the other hand, mechanical stability represents a major issue for the obtained porous frameworks and techniques have to be developed in order to harden them. Indeed, right after aggregation polymer gels or self-assembled structures are hold together only by physical interactions and typically present low mechanical strength and no resistance to solvation in organic solvents. In general, reactive molecular species, already present on the particle surface or added via coating, are used to glue the individual particles together via reaction or thermal annealing^{19,57} Another option in this sense is represented by a novel method developed in our group and named Reactive Gelation²². It is composed of different individual steps: starting from a stable colloidal suspension of polymer particles (the so called “latex”), additional monomer and initiator are added in order to further

swell them. Afterwards, the system is destabilized, either via electrolyte addition or via shear. Depending on the aggregation method, monoliths or clusters of primary particles are obtained. The last step comprises the hardening of the formed structures by post-polymerization reaction of the previously added monomer, to covalently link polymer chains by heating the system. This way, mechanical resistance is enhanced and functional porous materials can be developed⁵⁸. Owing to the peculiar structure that these porous polymers can exhibit and to the control that Reactive Gelation allows on the final morphology, they find major application in liquid chromatography^{21,22,59,60}. As commonly known, small polymer particles guarantee optimal separation performance (in terms of height equivalent of theoretical plates) but at the same time result in high backpressure per column length. On the other hand, large particles exhibit higher bed permeability and lower pressure drops but longer intra-particles diffusion pathways and limited performance^{61,62}. An alternative to overcome the trade-off between the two aforementioned parameters is represented by macro-porous materials both in the form of monoliths or particles. In the first case, all pore space can be assumed to be essentially convectively accessible, thus avoiding diffusion limitation to mass transfer^{63,64}, whereas in the second one large enough particles will guarantee low back-pressure, whilst at the same time the presence of huge pores ensures high permeability, as the flow can easily pass through them^{62,65}. This last phenomenon is known as perfusion⁶². Efficient macro-porous, mechanically stable, convective and perfusive materials can be produced by Reactive Gelation^{21,60}, showing distribution of large (bigger than 200 nm) interconnected pores. On the other hand, this morphology has a major limitation, which resides in the reduction of surface area. This issue may be overcome when brushes⁶⁶ or nanoparticles⁶⁷ are chemically introduced into the pores, effectively increasing the bind capacity⁶⁰.

1.3 Synthesis of Functional Nanoparticles: Surface Features and Core/Shell Architecture

Studies on the synthesis of polymer nanoparticles are nowadays of utmost importance as they play an extremely important role, not only in research but also in large-scale production⁶⁸. Indeed, an important number of commercial polymer derivatives are used or synthesized as dispersions. Although different preparation methods exist, it is of major interest to focus on the largely most common one: emulsion polymerization⁶⁹. Developed by Dinsmore in 1927⁷⁰ and fully described by Smith and Ewart⁷¹ in the forties, in the conventional formulation, water, monomers of low water solubility, a water-soluble initiator and a surfactant are present. Moreover, also surfactant free-emulsion polymerization has been proposed and described^{68,72}. The major advantage over other methodologies resides in the different kinetic from conventional polymerization reaction and more specifically in the concept of radical segregation, which allows high productivity of high molecular weight chains⁶⁹. Moreover, for most of the emulsion polymerization process, the concentration of monomer within the growing particles remains constant and thus, the reaction occurs always under similar conditions. This statement, in combination with conventional techniques to control polymer compositions in copolymerization (starved operation) makes very easy to obtain nanoparticles with desired final characteristics. As such, in an easy, scalable way (*i.e.* starved fed batch reactor or seeded polymerization) an extremely high control over the process is possible⁷³, allowing the product to present peculiar chemistry⁷⁴⁻⁷⁶, morphology⁷⁷ and architecture⁷⁸. Playing with the sequence of addition, reactive group⁷⁴ or inorganic components⁷⁹, can be introduced in the particle domain or brought on the surface for subsequent functionalization⁸⁰. Moreover, when dealing with copolymerization, also the reactivity ratio between the two monomers, the relative compatibility of the polymers, their interfacial tension and their different hydrophilicity strongly influence the

outcome^{77,81}. In general, blends of two kinds of polymer have a two-phase structure because most polymer pairs are not compatible. In practice, generally heterogeneous structures such as core-shell, polymeric-oil-in-oil (polymer 1 is dispersed in segregated domain all over polymer 2) and partially-localized (polymer 1 is segregated all in a single part of the particle) are recorded. The produced nanoparticles might therefore present patches or surface patterning that provide different and peculiar specificity to the particle-particle interaction generally observed in conventional colloidal gelation, making the prediction of their behavior all but easy⁸². Another last possibility is the one of tuning the particle physical properties by adjusting mixtures of compatible polymers. In this sense, coalescence^{83,84} within the polymer particles represent a major point. For this to occur it is necessary that the particle material, or at least the one on its surface, exhibits finite viscosity at the working temperature. This is achieved if the glass transition temperature T_g is below that temperature^{78,85}. Coalescence has a significant impact on both stagnant and shear-induced gelation. Indeed, it allows the particles to interpenetrate and form more compact clusters, with the result of a delayed gelation as the occupied volume fraction decreases⁸⁵. On the other hand, this interpenetration also reinforces significantly the adhesion energy within the particles and consequently the formed structures, which are then able to grow larger before breaking apart under shear stress⁷⁸. Combining the control over coalescence and primary particle architecture, it is possible to obtain clusters with peculiar morphology³⁰. Indeed, it is possible to grow on a hard, highly crosslinked core, a much softer, poorly crosslinked shell, allowing only partial coalescence and interpenetration. A representative parameter, defining this core/shell architecture is the ratio between the radius of the core and the one of the whole particle, or in formulas:

$$R_{cp} = \frac{\text{core radius}}{\text{particle radius}} \quad (9)$$

1.4 Characterization of Porous Materials

Still now, there is an intense research activity on the characterization of porous materials, because of the intrinsic difficulty of describing medias that are highly heterogeneous in pore size, pore shape and pore network organization^{86,87}. First, a major distinction is necessary regarding their form, as they can present themselves as bulk (i.e. monoliths or membrane) or as particles (i.e. porous beads). In this second case, an additional difficulty in the characterization is introduced by the inter-particles porosity, especially when the beads are heterogeneous and/or polydispersed. At this point, it becomes crucial to know the particles size distribution and this can be achieved via light scattering techniques⁸⁸ or microscopy. Moreover, both methods⁸⁸⁻⁹⁰ allow deriving the fractal dimension as a measurement of the compactness of the particles themselves. Even though a clear relationship between this parameter and porosity is far from being established, it is anyhow reasonable to believe that less compact clusters expose more surface area and pore volume³⁰. Regarding the pore morphology, some methods like nitrogen adsorption-desorption⁹¹, mercury intrusion⁹² and solvent imbibition⁹³ are considered as standards and many models are available to derive pore size distributions, surface area or total porosity from corresponding data⁹³. Generally, gas adsorption is limited to pores with radii smaller than 100 nm, whereas mercury porosimetry gives access to a large range of pore size, i.e. from 3.5 nm to 500 μm ⁸⁷. Unfortunately, these methods are based on capillary phenomena, which may induce stress on the walls of the material and lead to collapse. Moreover, mercury intrusion porosimetry is generally a destructive method and imbibition can be performed provided that a compatible fluid is available. A valid, non-destructive alternative is represented by inverse size-exclusion chromatography (ISEC)⁹⁴, because it is an in situ method mostly applicable at the same conditions as the separation process and independently to packed or bulk materials. Here, the pore size is deduced from the variation of the pore volume being inaccessible to a molecule of given size. The set of probe molecules, generally polymers or polysaccharides, must not

be adsorbed by the material. The experimental drawbacks of ISEC are the duration of experiment, the need of long columns for attaining appreciable resolution among different sized probes and the difficulties in finding very big (above 100 nm of hydrodynamic radius) not-interacting standards. When the pores are enough big, also microscopy techniques, such as TEM or SEM can anyhow provide useful information as long as conclusions are drawn from a statistically relevant number of samples. In general, it is always difficult to get reliable information from a single technique and it is useful to compare different results⁸⁷.

1.4.1 Light Scattering Techniques

These techniques allow the characterization of the particle size and of their fractal internal morphology. Moreover it is a non-destructive method and therefore of utmost importance in colloidal system analysis. Light scattering is due to the interaction of electromagnetic waves with matter. When the incident beam hits the sample, its electrons feel the interaction and an oscillating dipole is formed, which emits an electromagnetic radiation in all directions. The intensity of the scattered light strongly depends on the difference in refractive index between the specimen and the surrounding medium. The scattered light intensity can be used to evaluate the average structure factor of the cluster population⁹⁵:

$$\langle S(q) \rangle = \frac{I(0)P(q)}{I(q)} \quad (10)$$

where $I(0)$ is the intensity at zero angle, $I(q)$ is the angle-dependent scattered intensity, $P(q)$ is the form factor of the primary particles measured using the same instrument, q is the magnitude of the scattering vector, defined as

$$q = \frac{4\pi n}{\lambda} \sin\left(\frac{\theta}{2}\right) \quad (11)$$

where n is the refractive index of the continuous phase, λ is the laser wavelength in vacuum and θ is the scattering angle.

In order to relate the average structure factor to the radius of gyration, it is possible to use the Guinier^{88,96} approximation:

$$\langle S(q) \rangle = \exp \left(-\frac{q^2 \langle R_g^2 \rangle_{S(q)}}{3} \right), \text{ for } q \langle R_g \rangle_{S(q)} < 1 \quad (12)$$

The root-mean square radius of gyration of an aggregated population and the radius of gyration of the primary particles are evaluated with the following equations:

$$\langle R_g^2 \rangle = \langle R_g^2 \rangle_{S(q)} + \langle R_{g,p}^2 \rangle \quad (13)$$

$$R_{g,p} = \sqrt{\frac{3}{5}} R_p \quad (14)$$

As such, indications concerning the average cluster size can be obtained from the position of the bending of the curve when plotting the average structure factor $\langle S(q) \rangle$ as a function of q in a double logarithmic plot. It is important to highlight the fact that the contribution of primary particles is significant only for aggregates of small size. When multiple scattering is neglected, (i.e. the radiation illuminating every part of the sample is only the incident radiation) the Rayleigh-Debye-Gans (RDG) theory⁹⁵ may be applied. In accordance to that, additional information regarding the internal structure and the fractal dimension of formed aggregates can be derived from light scattering analysis³⁰. Again, plotting the average structure factor $\langle S(q) \rangle$ as a function of q in a double logarithmic plot, yields a straight line whose slope is equal to the fractal dimension d_f as reported in the following:

$$\langle S(q) \rangle \propto q^{-d_f}, \text{ for } \frac{1}{\langle R_g \rangle} < q < \frac{1}{R_p} \quad (15)$$

1.4.2 Intrusion and Adsorption Methods

Mercury Intrusion

Mercury intrusion porosimetry is an extremely useful analysis technique as it provides the most complete set of information about the pore size distribution of the tested material. Indeed, not only it covers pore

sizes over a range of 5 orders of magnitude (from 500 micron to 3.5 nm) but it enables to derive the pore size distribution, the total pore volume, the total porosity, the skeletal and the apparent density and the specific surface area of a sample⁹². In general, the probe is housed into a holder, called penetrometer, which is evacuated to remove air and residual moisture. Afterwards the filling procedure starts, first at lower pressure, intruding only the very large pores and slowly reaching values approximately of 400 MPa. This way the mercury is pushed also into very small pores and the minimal sizes are tested. Despite the aforementioned strengths, this technique has also some limitations as it is able to measure only the largest entrance towards a pore and not the actual inner size and it cannot be used to analyze closed pores, since the mercury has no way of entering them. Moreover, using such a high pressure, samples have to be able to withstand it without collapsing or changing their shape. Another very delicate point is the one of the model that is used to derive the pore shape: most instruments assume cylindrical pore geometry using the Washburn equation, which relates the pressure difference (ΔP) across the curved mercury interface to the corresponding pore size (r_{pore}) using the surface tension of mercury (γ) and the contact angle between the solid and the mercury (θ) and it is written as following:

$$\Delta P = \frac{2\gamma \cos\theta}{r_{pore}} \quad (16)$$

On the other hand, it is true that the shape of the total intrusion volume curve and of the extrusion one can give information about the shape of the pores, and specifically purely cylindrical, conical and ball-like pores can be detected⁹⁷.

As one can see in the Washburn equation, the contact angle is a parameter that clearly affects the analysis result. Even though huge work has been done in order to determine the different contact angles between mercury and different materials, it is anyhow true that in most practical situation a value between 130° and 140° is used, independently of the sample. Considering the many variables that affect the measurements itself, it is important to highlight that pore size distribution data generated by mercury

porosimetry are useful in comparative studies of similar materials⁹². This way, even if the accuracy of the data depends on various assumptions and experimental factors, they remain the same for all the samples.

Data from mercury intrusion porosimetry can also be used to estimate the particle size of a powder material. In general, geometric models^{98,99} can be used. Anyhow, the extraction of this information is all but easy when particles are not spherical but rather amorphous. As a rule of thumb, the particle size arrests on two to four times larger than the measured pore size⁹².

Nitrogen Adsorption (BET)

BET theory uses data obtained from multilayer nitrogen adsorption measurements to determine the specific surface area of a material. Moreover, also the total nano- to meso-pores volume of the samples can be evaluated⁸⁶. Adsorption is defined as the adhesion of atoms or molecules of gas to a surface. Generally, these two values are proportionally correlated. On the other hand, other parameters, such as temperature, pressure and specific interactions between the gas and the solid might affect the amount of gas adsorbed on the exposed surface. In BET surface area analysis⁹¹, nitrogen is commonly used because of its availability in high purity and its strong interaction with most solids. Before starting the actual measurement, the sample, housed into a tube or a cell, needs to be degassed to remove water and other contaminants. At this point, known amounts of nitrogen gas are released stepwise into the sample cell with a calibrated piston. In general, the surface is kept cool with liquid nitrogen in order to promote the interaction between the gas and the solid phase and obtain detectable amounts of adsorption. Pressure is increased until the saturation one (P_0) is reached and the adsorption layers are formed. At this point no more adsorption occurs, regardless of any further increase in pressure. Therefore, the sample is removed from the nitrogen atmosphere and heated to cause the adsorbed gas to be released from the material and quantified. It is possible to plot the amount of gas adsorbed as a function of the relative pressure⁹¹. The

resulting curve is called adsorption isotherm and can assume different shapes. The BET equation uses the information from the isotherm to determine the surface area of the sample. It has the following form⁹¹:

$$\frac{1}{X((P_0/P)-1)} = \frac{1}{X_m C} + \frac{C-1}{X_m C} \left(\frac{P}{P_0}\right) \quad (17)$$

where X is the weight of nitrogen adsorbed at a given relative pressure (P/P_0), X_m is the monolayer capacity, which is the volume of gas adsorbed at standard temperature and pressure (273 K and 1 atm), and C is the BET constant⁹¹. As long as the working range is $0.05 < (P/P_0) < 0.35$, it is possible to plot Equation 17 as a straight line with $\frac{1}{X((P_0/P)-1)}$ on the y-axis and $\left(\frac{P}{P_0}\right)$ on the x-axis. In that way, it will assume the general form $y = Ax + B$. Therefore, with the experimental data it is possible to derive the values of the slope A and of the intercept B and use them to calculate the monolayer adsorbed gas quantity X_m and the BET constant C . In particular, we have:

$$X_m = \frac{1}{A+B} \quad (18)$$

$$C = 1 + \frac{A}{B} \quad (19)$$

Once the monolayer capacity is determined, the total surface area S_t can be calculated with the following equation:

$$S_t = \frac{X_m N A_m}{v} \quad (20)$$

where N is the Avogadro number, A_m is the cross sectional area of the adsorbate (0.162 nm² for a nitrogen molecule) and v is the molar volume⁹¹. The BET surface area, which is generally reported, is obtained by dividing S_t by the initial mass of the dry sample and is expressed in m²/g.

1.4.3 Chromatography

Inverse-size exclusion chromatography (ISEC) is used to determine the accessible porosity and the surface area of materials⁹⁴. Differently from intrusion and adsorption methods, which generally require

dry samples and may deform or damage the material, ISEC utilizes standard probe molecules (*i.e.* of defined molecular mass and size) to evaluate the intra-particle pore volume of a wet sample either in a packed volume (*i.e.* a column) or in bulk¹⁰⁰. This method was developed in 1978 by Halasz¹⁰¹ and constantly improved in the following years. In general, when molecules of a defined size are eluted through the sample, their retention volume can be experimentally determined and characterized in terms of size exclusion distribution coefficient K_d :

$$K_d = \frac{V_R - V_0}{V_T - V_0} \quad (21)$$

where V_R is the solute elution volume, V_0 the interparticle void volume and V_T is the total mobile phase volume. K_d is generally 0 for a totally excluded compound and 1 for compounds able to access and penetrate the whole pore volume. The K_d values for the standards are typically plotted against the log of their molecular size, and a calibration curve is obtained. Dextrans or other polysaccharides are the most common calibration standards, as several correlations between their molecular weight and hydrodynamic radius are available^{94,102}. In ISEC, the pore size distribution is estimated from the calibration curve, assuming that the pore volume is constituted by pores with a uniform shape but different cross-sectional dimension. The most used functional form in this sense is the Gaussian relation, even though it can be physically unrealistic in permitting negative values of the cross-sections⁹⁴. Therefore, alternative distributions have also been developed. Moreover, the calculation of K_d for a given distribution is model-dependent, as an assumption over the pore and the standard shape has to be taken. The standard description is of spherical probe and cylindrical pore, but other shapes have been examined¹⁰³.

1.4.4 Microscopy

Depending on the nature of the incident radiation, microscopy techniques allow the visualization of small object at different scales. In general, optical microscopy can be used to obtain images of small samples

through the usage of visible light with a maximum resolution of $0.2 \mu\text{m}^{104}$. As such, it is very useful in the determination of the particle size distribution and morphology when coupled with conventional image analysis programs such as Fiji or Image J¹⁰⁴. Together with conventional systems, also confocal microscopy¹⁰⁴ represent an extremely useful technique in visualization of samples, as it allows very small axial resolutions. The way through which an image is formed differs from the conventional one as light invests the object in a single point at a time and a scan of the whole sample is required to obtain the final image. This way, the images are formed as optical sections and it is possible to inspect the sample in three dimensions in a non-invasive way. This technique can also be coupled with fluorescence, and become extremely sensitive, allowing the detection of single molecules¹⁰⁴. When a much higher resolution is required, it is necessary to switch from visible light to an electron beam with a far smaller wavelength. The resulting technique is named electron microscopy and the used systems are those of TEM (Transmission Electron Microscopy) and SEM (Scanning Electron Microscopy)¹⁰⁵. In the first one, the electromagnetic lenses focus electrons into a thin beam, which interacts with the observed specimen. The electrons scattered by the samples reach a fluorescent screen and result in the creation of an image. The mass-thickness and the diffraction contrast agent affect the shades of the darkness of the image. This technique is capable of imaging at a significantly higher resolution than light microscopes and thus, observation even of individual primary nanoparticles is possible¹⁰⁵. In the second one, the sample is scanned with a focused high-energy beam of electrons in order to produce an image. The latter is a result of the interaction of the electrons with the specimen and, depending on the angle with which the beams hit the surface, this technique enables to gather information about the surface topography, compositions and size of the samples¹⁰⁶. In general, microscopy is considered to be a non-destructive technique, even though many times samples have to be dried in order to be prepared for visualization.

1.5 Aim and Outline of the Present Work

In the present work, porous polymeric materials in different forms have been produced via Reactive Gelation and characterized in terms of final porous structure and mechanical properties, as a function of the primary particle core/shell architecture. The versatility of the used technique resides in the control over different mechanisms of colloidal aggregation, which have been also studied and described in light of the aforementioned particle characteristics.

In Chapter 2, performing stagnant aggregation, monoliths with very well defined pore size distribution have been developed, by playing with primary particles architecture and initial latex concentration.

In Chapter 3, purely shear-induced aggregation is used in order to prepare a base scaffold for chromatographic application, which, in comparison to current commercial resins, exhibits not only extremely low-pressure drops even at very high flow rates, but also constant efficiency for tracers in size range of common bio-macromolecules.

In Chapter 4, Reactive Gelation and microfluidics are combined for the production of robust hollow microcapsules, with tunable surface porosity and permeability.

In Chapter 5, finally, a fundamental study on surface effect in aggregation under shear is presented. Starting from peculiar and unexpected behavior, experimentally recorded when particle with specific architecture are aggregated under shear, an *ad hoc* solution has been developed and it enabled to identify material transfer within individual particles as a possible responsible for the aforementioned unusual observations.

Chapter 2

Control of Pore Structure in Polymeric Monoliths Prepared from Colloidal Dispersions

2.1 Introduction

Porous polymers find important applications in various areas, ranging from biotechnology¹⁰⁷, to energy storage¹⁰⁸, catalysis¹⁰⁹ and adsorption separations¹¹⁰. In the latter case, porous particles¹¹¹ as well as monoliths^{63,64} are used as major stationary phases in liquid chromatography. Such a variety of applications depends primarily on the very peculiar features of these materials, especially in terms of porous structures, since monodispersed¹¹² as well as hierarchical¹¹³ arrangements of micro-, meso- and macro-pores can be obtained. Different strategies are available for the preparation of these materials¹¹⁴. The most common one implies the usage of a porogen for the formation of porous particles^{114–116}. In addition, block-copolymer self-assembly¹¹⁷ and post modification of resins, carried out generally via pyrolysis¹¹⁸ or solvent exposure¹¹⁹, are also used. In all of these methods, many different, interlinked parameters affect the final product properties and the resulting structure, making often difficult the design and control of the process¹¹⁴.

As an alternative to the previously mentioned approaches, colloidal gelation^{19,120} represents an original procedure to synthesize porous structures. Taking advantages of the fractal geometry of the micro-

clusters³⁰ formed during the particle aggregation, eventually leading to a percolating network¹⁶, different porous frameworks can be obtained. These can be stabilized in structures exhibiting strong mechanical properties through the Reactive Gelation process²⁰. This method comprises different subsequent steps: starting from a dispersion of polymer nanoparticles in water (the so-called latex), additional monomer and oil-soluble initiator are added in order to swell the particles. After aggregation, occurring because of suitable latex destabilization, the added monomer is further polymerized in order to form strong inter-particle bonds by means of connecting polymer chains, thus providing mechanical resistance to the previously achieved percolating structure. Using this technique, many different materials for liquid chromatography application, both in form of monoliths^{22,59} as well as particles^{21,60,121} have been produced. The major advantage of this method resides in the possibility to tune and precisely control the size, composition, morphology, surface characteristics and functionalities of the primary particles which are prepared through the well-established emulsion polymerization⁷³. Moreover, the aggregation process as well can be controlled playing with the latex properties (i.e., volume fraction or charge properties of the particle surface) and aggregation kinetics (i.e., electrolyte addition)¹⁶. All the aforementioned parameters concur to define the morphology of the final gel, resulting in a variety of final structures³⁰. Upon post-polymerization, the final gel acquires remarkable mechanical properties and is then able to withstand solvent evaporation from the pores during ambient drying.

In this work we show quantitatively how to carefully control the porous structure in monolithic foams by properly acting on specific latex properties, namely particle architecture (core and shell composition and thickness), average particle size, and solid content of the latex. This way, the pore size distribution and morphology in polymer monoliths can be tuned across multiple length scale. This control directly reflects into the functional properties of the monoliths themselves in dependence of their final application. For example, in chromatography large pores make the mass transport dominated by convection, allowing high performance at very high flow rates⁶⁴. Moreover, careful control of the

individual pore sizes is desirable for size exclusion operations. On the other hand, in thermal insulation, smaller pores are required because they reduce the conductivity of the final material when compared to the mean-free-path of the contained molecules¹²².

2.2 Experimental

2.2.1 Materials

The following chemicals have been employed without further treatments: styrene (STY, 10-15 ppm 4-tert-butylcatechol as stabilizer, purity 99%) from ABCR-Chemicals (D-76187 Karlsruhe); divinylbenzene (DVB, technical grade, > 80%) and sodium dodecyl sulfate (SDS, purity \geq 99%) from Sigma Aldrich; potassium peroxydisulfate (KPS) from Merck Millipore, 2,2'-azobis(2-methylpropionitrile) (AIBN, purity 98%) from Fluka Analytical; sodium chloride (for analysis, ACS, ISO, Reag. Ph Eur) from Emsure. Ultra-pure grade water was prepared by Millipore Synergy.

2.2.2 Reactive Gelation

The procedure used to synthesize the porous monoliths is based on the following steps: initially, a polymer latex (colloidal dispersion of polymer particles in water) was synthesized via emulsion polymerization and subsequently monomer and oil-soluble initiator were added. Afterwards, the swollen nanoparticles were destabilized and aggregated in a controlled way via salt addition. Once the gel was formed, it was left overnight at 50°C inside an oven to complete the added monomer consumption by free radical polymerization. Finally, the monoliths were fully dried, enabling their complete morphological characterization. All of the aforementioned steps are described in details in the following.

Emulsion polymerization

A semi-batch emulsion polymerization protocol was followed for the production of all the latexes. This procedure was divided into two subsequent steps, corresponding to the synthesis first of the core and then of the shell of the polymer particles. In particular, in the first phase a highly crosslinked (20%) seed of nanoparticles was produced and in the second one, a softer, less crosslinked (1%) shell was grown. Starting from a mixture (Initial Charge, IC) of water and surfactant (SDS) into a glass reactor, a solution (Initiator Shot 1, IS1) of water and initiator (KPS) was injected, once the temperature reached the set-point of 70°C. Afterwards, an emulsion of styrene, DVB, water, and surfactant (Charged Feed 1, CF1) was fed over the reaction time using an HPLC pump. Moreover, a solution of water and KPS (Initiator Feed, IF) was continuously fed as well, as the total reaction time is longer than the half-life time of the initiator at the reaction temperature. The reacting mixture was constantly monitored and specifically conversion checked to ensure that the system is kept in starved condition. The previously synthesized latex acts as a seed for the growth of a soft shell around the hard core particles. A new monomer solution (Charged Feed 2, CF2), this time composed only of styrene and DVB, was then fed to the system in a continuous way (i.e., without lag time or stopping the previous reaction of core synthesis), in order to achieve a radially homogeneous shell growth. The previous initiator feed was disconnected, while a shot of water and KPS was added to the reaction to keep it proceeding (Initiator Shot 2, IS2). Also during this stage, the reacting mixture was constantly monitored in terms of conversion to ensure starved condition. After the new monomer addition was complete, the synthesis was stopped once full conversion and the desired particle size, determined as z-average value from dynamic light scattering measurements, were obtained. Further details and references on the synthesis of each latex are reported in Appendix A.

Latex Swelling

The latex was diluted with deionized water to the desired dry solid content, measured through thermogravimetric analysis in a HG53 Halogen Moisture Analyzer from Mettler-Toledo. Afterwards,

an additional amount of a mixture of divinylbenzene and AIBN (5 %wt with respect to the monomer) was added. Considering the much larger amount of cross-linker in the core than in the shell, it is reasonable to assume that this additional monomer swelled only the outer layer of the particles. This additional mixture amount was about 20 %wt with respect to the dry solid content of the particle shell. The solution was left under agitation at 200 rpm overnight to ensure equilibrium swelling.

Latex Gelation

The swollen latexes were aggregated by mixing with an equivalent volume of a salt solution within 4 ml vials. Typical gelation time is about 20 minutes. The vials were carefully closed before post-polymerization. The specific recipes of each produced monolith are reported in Appendix A.

Gel Post-Polymerization and Drying

The formed gels inside the closed vials (Figure A.1 of Appendix A) were put into an oven at 50° C for at least 12 hours. After the reaction, they were still wet and quite fragile (the material cannot be easily handled – moved or touched – without damaging it). They were then transferred into a container with excess of water and left there (2-3 days) to remove residual non-aggregated particles and salt from the gel. Finally, the monoliths were dried in air, while their weight loss was checked daily to verify that full drying was achieved (the process takes ca. 3-5 days).

2.2.3 Monolith Characterization

The pore size distribution of the dry monoliths have been measured by mercury intrusion porosimetry (Hg Intrusion) using the instruments Pascal 140 and Pascal 440 from Thermo Scientific. Further investigation of the monolith structure and surface were performed by scanning electron microscopy (SEM) using a Gemini 1530 FEG from Zeiss with field emission gun operated at 5 kV. Surface area measurements were performed via nitrogen adsorption (BET theory) using TriStar 3000 from Micromeritics. Finally, the total porosity was estimated by measuring the skeletal density of the sample

and comparing it with the one of the fully non-porous materials. In particular, each dry sample was weighted first, then put into a container filled with isopropyl alcohol and left for 24 hours to achieve complete penetration of the solvent into the pores. Each sample impregnated by the alcohol (IPA-wet foam) was weighted again to evaluate the mass of alcohol intruded into the pores. The total porosity of each samples (ε) was then evaluated as follows:

$$\varepsilon = \frac{(m_{wet} - m_{dry}) / \rho_{IPA}}{\frac{m_{wet} - m_{dry}}{\rho_{IPA}} + \frac{m_{dry}}{\rho_{PS}}} \quad (1)$$

where ρ_{PS} and ρ_{IPA} are the densities of polystyrene and IPA, respectively, while m_{wet} and m_{dry} are the masses of IPA-wet and dry samples, respectively ($\rho_{PS} / \rho_{IPA} = 1.325$). Fifteen different measurements have been repeated for each monolith and average values with standard deviation have been computed. The obtained results have been compared with those obtained through Hg intrusion in order to cross-check the results.

2.3. Result and Discussion

2.3.1 The Reactive Gelation Process

During the first step of the process the particles are destabilized by electrolyte addition in the stagnant dispersion and aggregation proceeds until the resulting fractal clusters occupy all of the available space and their movement is hindered (arrest time). At this point they start interconnecting with each other, forming a percolating structure. The whole process is controlled by the electrolyte concentration in solution, leading to different aggregation regimes, namely DLCA (diffusion limited cluster aggregation) and RLCA (reaction limited cluster aggregation)¹⁶. Considering the swelling of the outer layer of the particles, which reduces considerably the glass transition temperature (T_g) of the polymer¹²³, it is reasonable to assume that they partly interpenetrate depending upon the shell thickness¹²⁴. Particles with

small core-to-particle ratio will interpenetrate more than those with larger ratios if the characteristic time of the gelation process is small enough compared to that of partial coalescence. Once the gel is heated up in the oven, the monomer in the outer layer of the particles starts polymerizing and, at the same time, particle rearrangement takes place, thus resulting in monolith shrinking. A second shrinking takes place during drying because of the evaporation of the capillary water¹²⁵. Being the resulting porous framework affected by the combination of all the above processes, many parameters play a role in the process. In the following, the effects of particle core-shell morphology (architecture) and initial latex dry content are investigated.

2.3.2 Effect of Particle Architecture

To investigate the effect of particle architecture on the final pore structure of the monoliths, different latexes have been synthesized, as shown in Table 2.1. The ratio of the core to the particle size, R_{CP} , and the actual size of the particles are changed. The dry content of the initial latex has been set equal to 8 %wt in all cases and all monoliths have been produced by mixing equivalent amounts of latex and salt solution, thus achieving RLCA conditions. Total porosity and surface area values of the obtained monoliths are summarized in Table 2.2.

Table 2.1. Particle architecture of the different latexes.

Latex	Core size [nm]	Particle size [nm]	R_{CP}¹
L1	80	110	0.73
L2	90	110	0.82
L3	100	110	0.91
L4	41	56	0.73
L5	40	49	0.82

Table 2.2. Total porosity and surface area of the produced monoliths.

Sample	Latex	Total Porosity [%]	Surface Area [m²/g]
M1	L1	86.6 ± 0.3%	17.37
M2	L2	79.5 ± 2.6%	36.1
M3	L3	-	58.69
M4	L4	83.9 ± 0.3%	28.17
M5	L5	77.8 ± 0.7%	58.76

Large Particles

Let us focus on the monoliths synthesized from the largest particles, i.e., M1, M2 and M3. As mentioned above, the monoliths are formed by salt addition, waiting until full percolation. All monoliths shrink

¹ Ratio of the core to the particle size

during post-polymerization and larger shrinkage is found for structures formed from particles with smaller core-to-particle ratio. Remarkably, almost no shrinkage was observed for the case of the thinnest shell, sample M3. This means that the shell thickness, i.e., the amount of post-polymerized monomer, affects the rearrangement.

After the drying step, the final monoliths shown in Figure 2.1 are obtained. This time, the trend is opposite to that observed for the previous process step: the monolith formed from particles with a small core-to-particle ratio (M1) retained its volume much better than M2, which instead shrank considerably. Moreover, the monolith M3 was not mechanically stable and broke into fragments while drying. It is worth repeating that each gel was formed mixing the latex with an equal volume of salt solution at well-defined concentration (details in Table A.5 of Appendix A): the collapse or major modification of the structure occurred afterwards, during the drying phase, where the shell thickness of the particle has much larger influence on the final structure than the gelation itself. Thicker shells allow in fact for deeper particle-particle interpenetration during aggregation thus providing better mechanical stability to the monolith, which therefore can better keep its structure during drying. On the other hand, thinner shells reduce the extent of interpenetration, thus leading to more fragile structures. Therefore, these gels need more rearrangement during drying to find a stable structure: this was the case of sample M2 while the interpenetration was not enough for sample M3 and the structure collapsed.

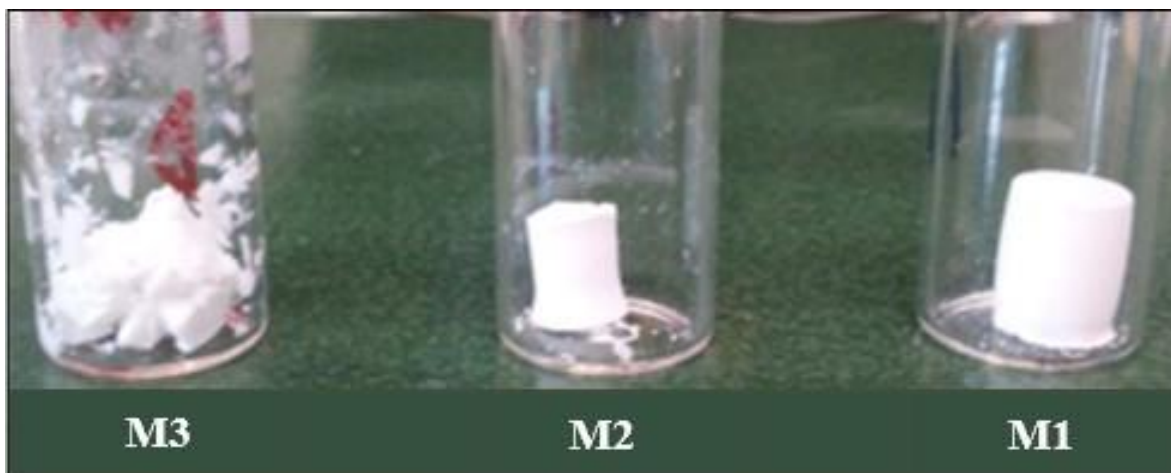


Figure 2.1. Dried monoliths synthesized from different latexes.

These considerations are supported by the SEM pictures shown in Figure 2.2 where the different extents of interpenetration are clearly identified moving from the sample M1, in which the identity of the single primary particles is lost (Figure 2.2a), to M3, where the individual particles are still clearly recognizable (Figure 2.2c). The sample M2 (Figure 2.2b) lies clearly somewhere in between. The previous discussion directly reflects also into the possible final applications, as an intermediate processing of the monolith would anyhow be required before use. Indeed, actions like press-fitting into proper housing for chromatography⁵⁹ and general material handling in the form of huge thermal insulation panels, require suitable mechanical stability.

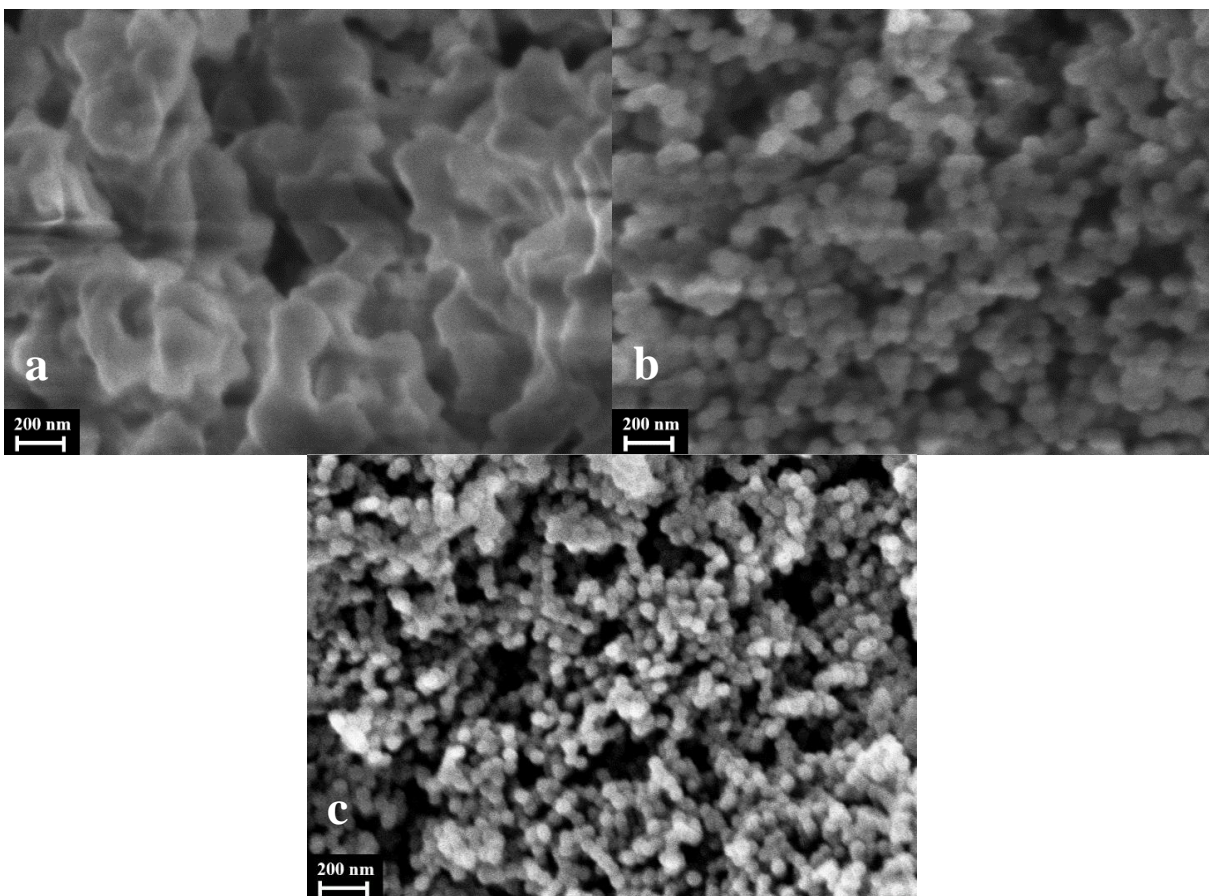


Figure 2.2. SEM pictures of the monoliths formed from samples M1 (a), M2 (b) and M3 (c).

The pore size distributions of monoliths M1 and M2 measured by Hg intrusion are shown in Figure 2.3. The difference between the two is evident: sample M1 exhibits bimodal pore size distribution, whereas M2 a quite broad monomodal one. Latex L1 enabled the preservation of large pores, with diameter up to 10 micrometers, while the smallest pore, those among individual nanoparticles, disappeared by coalescence. On the other hand, latex L2 did not allow large pores to remain in the final monolith, since they are most probably lost during drying and shrinking, while small pores are present even in the range of few nanometers. Note that the two materials are quite different in terms of total porosity, with monolith M1 exhibiting much larger pore volume (Table 2.2).

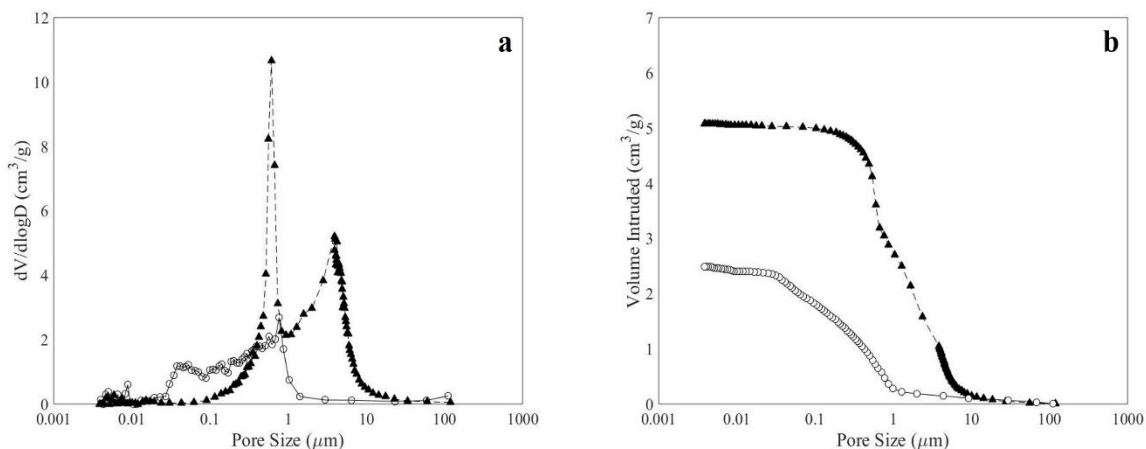


Figure 2.3. Differential (a) and cumulative (b) pore size distribution of the monoliths M1 (filled triangle) and M2 (empty circles).

These results can be explained as follows: since both samples percolated occupying the same volume, with identical particle size and concentration, their initial gel structure (*i.e.*, right after stagnant gelation) is rather similar, with possible minor discrepancies due to the different shell thickness. The bimodal pore structure formed during gelation originates from two processes: the first one refers to the initial aggregation of the primary particles, leading to aggregation characterized by a well-defined fractal dimension (in the order of 1.9 – 2.2) which is responsible for the small inter-particles pores (0.01 to 1 μm), and the second one, which refers to the final cluster interpenetration and interconnection during the percolation phase, responsible for the large inter-clusters pores (1 to several μm). The capability of the monolith to maintain this bimodal structure during post-polymerization and drying, mainly dependent on the primary particle architecture, determines the final pore structure: smaller pores tend to disappear under the effect of partial coalescence, which is the case of sample M1, while less interpenetration makes the structure less stable, leading to a loss of large inter-cluster pores and preserving the inter-particle ones.

The measured values of specific surface area confirm the different interpenetration of the primary particles shown in the SEM pictures as well as the contribution of small pores ($< 0.1 \mu\text{m}$) measured via

Hg intrusion. As shown in Table 2.2, the lower the thickness of the shell, the larger is the value of the measured surface area.

Small Particles

In order to check whether the effect of the particle architecture is affected by the particle size, let us consider the monoliths produced from latexes with small particles, M4 and M5 in Table 2.2. Notably, the shrinkage is again determined by the ratio R_{CP} , which in turn controls the restructuring upon post-polymerization and drying (Figure 2.4). Samples made from particles with equal core-to-particle ratio shrank equivalently.

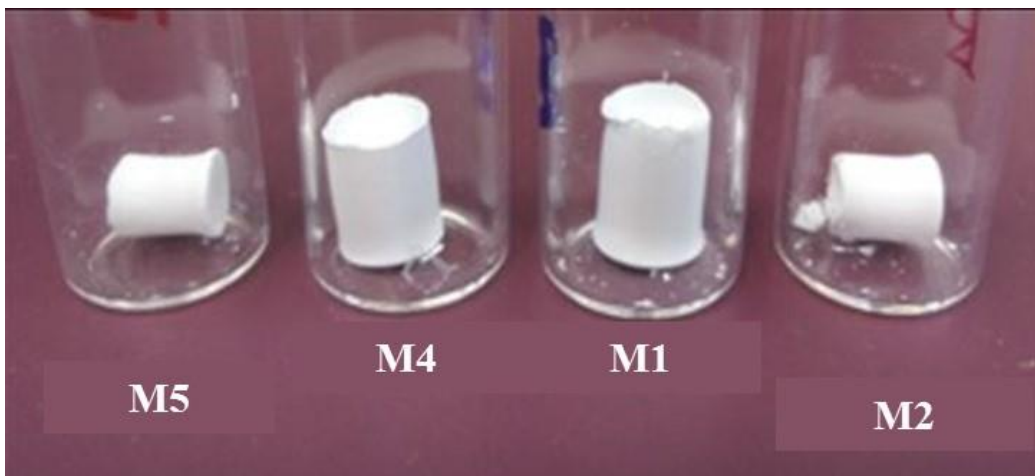


Figure 2.4. Dried monoliths synthesized from different latexes presenting equivalent particle size (L5 and L4, L1 and L2) or equivalent particle architecture (L4 and L1, L5 and L2).

Also the pore size distribution is again determined by R_{CP} or shell thickness, as it appears from the curves referred to the samples produced with smaller particles and measured by Hg intrusion shown in Figure 2.5. Both the differential and cumulative pore size distributions are similar to those discussed for larger particles and the same conclusions can be drawn also for this case.

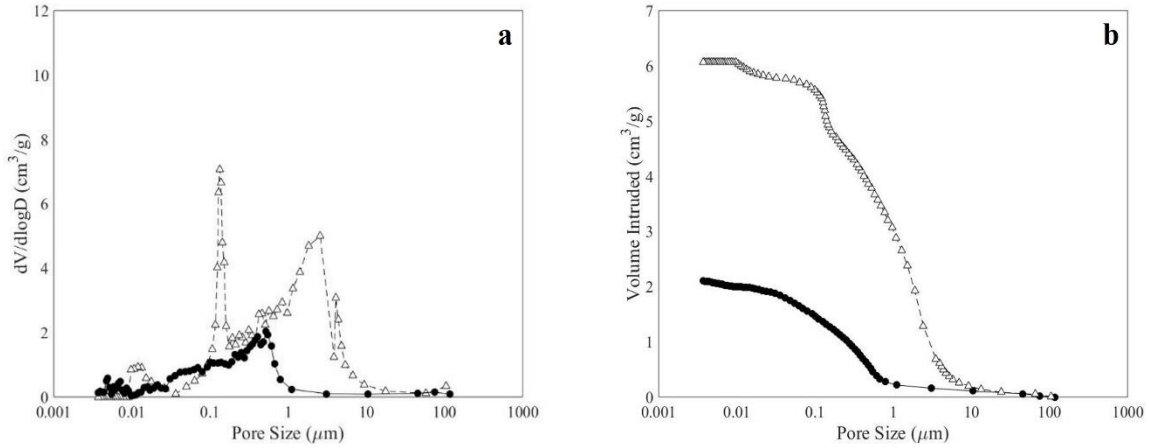


Figure 2.5. Differential (a) and cumulative (b) pore size distribution of the monoliths M4 (white triangle) and M5 (black circles).

In particular, a detailed comparison is shown in Figure 2.6 in the cases of samples made from latexes with the same $R_{CP} = 0.73$. It is seen that smaller primary particles lead to smaller inter-particle pores, as indicated by the shift of the first peak in the pore size distribution from approximately 600 nm for particles with total size of 110 nm to about 150 nm for particles with total size of 56 nm. In both monoliths the largest pores (from 1 μm to 10 μm) are preserved, even though the actual position of the peak corresponds to smaller pore size for smaller particles. This effect is mainly driven by the crowding of the particles more than by their size, since the identical dry content for the two starting latexes leads to different particle concentration in the final volume.

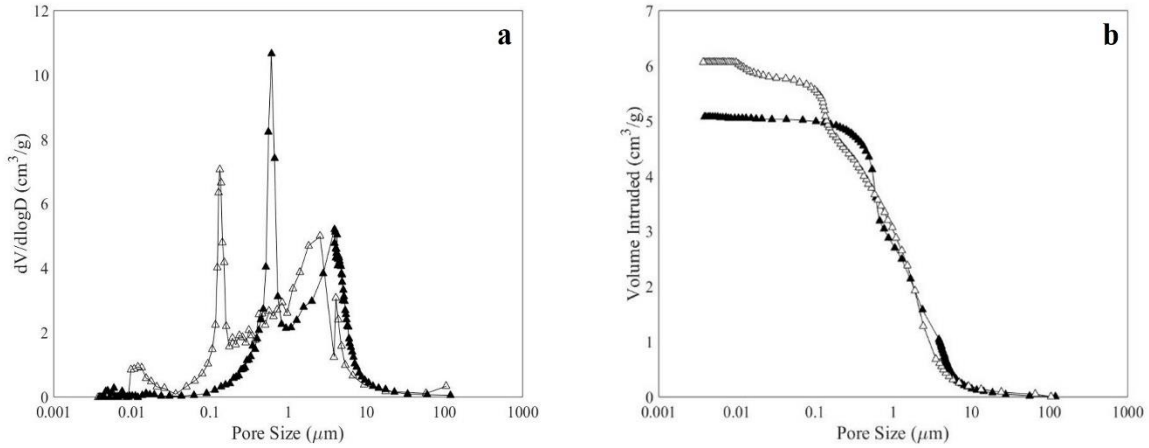


Figure 2.6. Differential (a) and cumulative (b) pore size distribution of the monoliths M4 (white triangle) and M1 (black triangle).

In the case of primary particles with $R_{CP} = 0.82$, the particle size effect becomes irrelevant, as shown in Figure 2.7. Indeed, only the largest pores are slightly affected by the previously mentioned particle crowding.

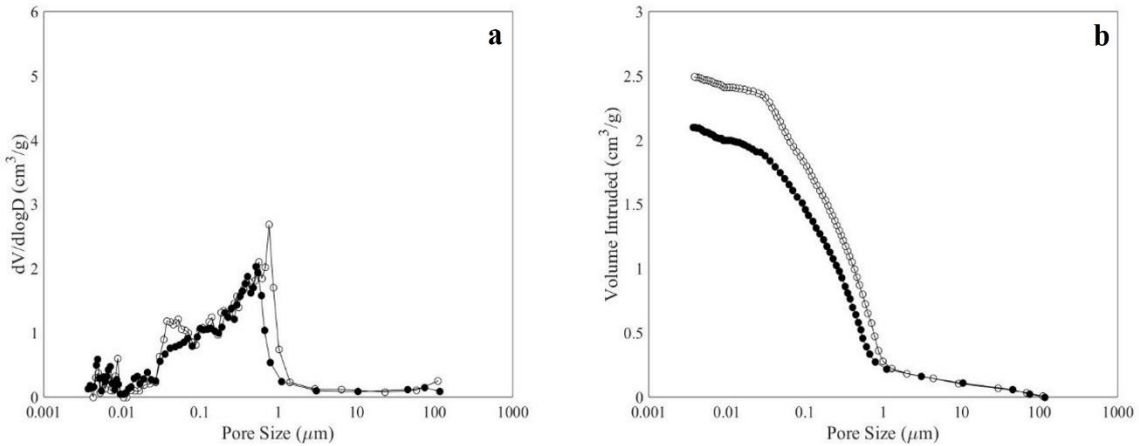


Figure 2.7. Differential (a) and cumulative (b) pore size distribution of the monoliths M5 (black circles) and M2 (white circles).

The data in Table 2.2 show that the reduction of total porosity upon shrinkage is observed also for smaller particles. Indeed, monoliths M4 and M5 exhibit a difference in porosity of 6.1% (Table 2.2), similarly to the case of large particles. Furthermore, the porosity values are also quite similar for particles with

equivalent core-to-particle ratio (e.g. compare the values for samples M4 and M1). Not surprisingly, materials with similar pore size distribution, exhibit also similar total porosity values (cf. samples M2 and M5).

The values of specific surface area, shown in Table 2.2, reflect the different interpenetration of the primary particles already shown in the SEM pictures as well as the fraction of small pores, namely below 0.1 μm , measured by intrusion techniques. In particular, the lower the thickness of the shell, the higher the value of the measured surface area, e.g. M4 presents a specific surface area smaller than M5. Not surprisingly, the value is larger for smaller particles.

2.3.3 Effect of initial dry content

It was found that latexes composed of nanoparticles with smaller core-to-particle ratio ($R_{CP} = 0.73$) can preserve the percolation structure obtained during the gelation process, independently of the initial nanoparticle size. This behavior has been observed also for different initial concentrations of primary particles still keeping the monolith volume equal to that of the same container. Therefore, the porosity of the final volume is strongly affected by the dry content of the initial latex. On the other hand, particles with $R_{CP} = 0.82$ suffered major restructuring upon drying and the dry content effect might be less relevant. To study the impact of the solid content, different monoliths have been produced starting from latexes L1 and L2 at different dry contents as summarized in Table 2.3. Since the two sets of monoliths have been prepared from the same primary particles, the specific surface remains constant and BET measurements have not been run.

Table 2.3. Characteristics of the monoliths produced at different dry contents.

Sample	Latex	Initial dry content [w/w]	Porosity [%]
M6	L1	0.12	77.1 ± 1.0%
M1	L1	0.08	86.6 ± 0.3%
M7	L1	0.04	89.5 ± 0.4%
M8	L2	0.12	68.1 ± 0.1%
M2	L2	0.08	79.5 ± 2.6%

Core-to-particle ratio 0.73

Let us consider first the monoliths with larger shell thickness M6, M1, and M7 in Table 2.3. The pore size distributions of the different samples are shown in Figure 2.8.

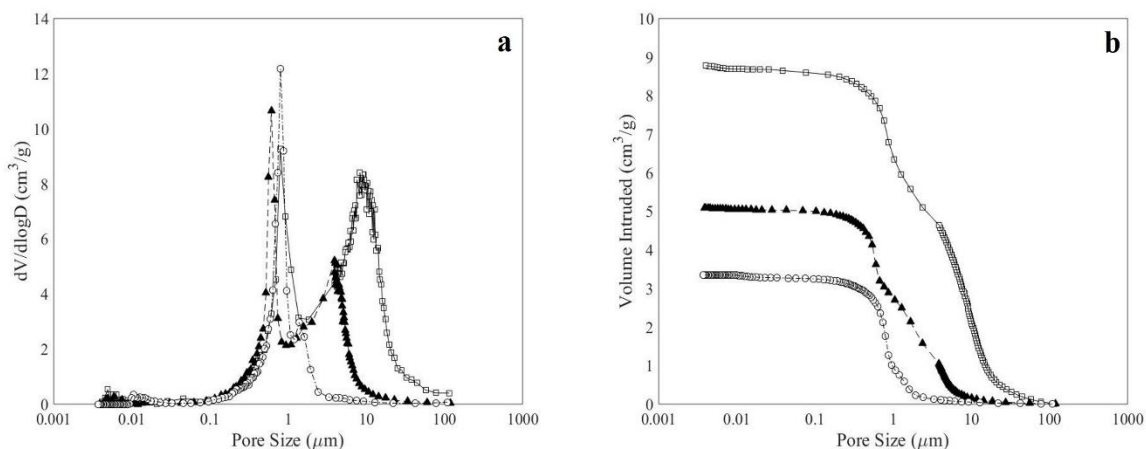


Figure 2.8. Differential (a) and cumulative (b) pore size distribution of the monoliths M6 (white circles), M1 (black triangles) and M7 (white squares).

All of them look bimodal, with a first peak approximately at 0.6 - 0.8 μm and a second one at much larger values of pore size, whose value is a function of the solid content i.e. 1.5 μm for sample M6, 4 μm for 1, and 9 μm for M7. Remarkably, the area of the second peak increases with decreasing of the initial

dry content of the latex. This behavior can be explained considering the mechanism of gel formation: at the beginning of the process, particle aggregation proceeds and fractal clusters are formed. Small pores are generated as interstitial spaces among the primary nanoparticles, that is the inter-particle pores corresponding to the left peaks in Figure 2.8. As seen above, those pores are affected by the interpenetration due to the shell softness and not by occupied volume within the container as well as by the dry content. Once the system is crowded, the clusters start interpenetrating each other and percolation occurs. This mechanism is responsible for the formation of larger pores, that is the inter-cluster pores, corresponding to the right peaks in Figure 2.8. At this stage, the initial dry content becomes the crucial factor: samples produced with smaller dry content, exhibited much larger inter-cluster pores and lower mechanical resistance.

The corresponding overall porosity values are shown in Table 2.3. Reducing the dry content increases the porosity of the final dry monolith, especially when the shape is retained upon drying. While such increase is quite relevant when the solid content decreases from 12% to 8%, it is less relevant from 8% to 4%. This result is not surprising since there should exist anyhow a limit value of porosity for which the monolith can actually be produced. As a matter of fact, it is quite difficult to observe the gelation process with dry content lower than 4%.

Core-to-particle ratio 0.82

In this case (samples M8 and M2 in Table 2.3), the effective shrinkage was much more relevant than in the case of particles with thicker shell discussed above.

The pore size distributions of the different samples are shown in Figure 2.9. After shrinkage, the initial percolation structure is lost in both cases and only the smallest inter-particles pores are retained. This means that, independently on the initial dry content, a major rearrangement takes place in order to find an equilibrium during drying, which results in the loss of the largest pores. Therefore, the dry content

has no effect on the morphology of the final monolith when particles with high enough core-to-particle ratio are used.

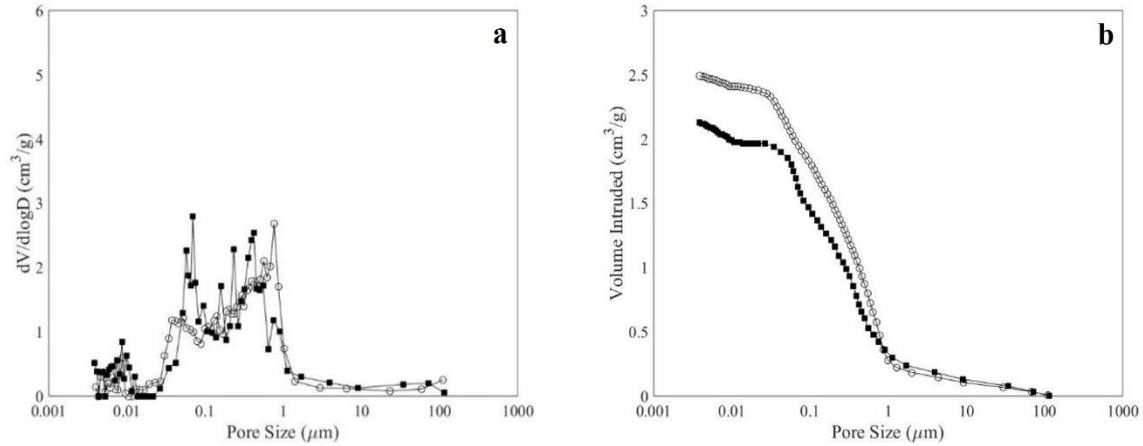


Figure 2.9. Differential (a) and cumulative (b) pore size distribution of the monoliths M8 (black squares) and M2 (white circles).

Looking at the total porosity values in Table 2.3, it appears that the overall porosity of the sample decreases by decreasing the solid content of the initial latex. The difference in porosity between the two monoliths, equal to 11.4 %, is quite similar to that of latexes with $R_{CP} = 0.73$, equal to 9.5%, thus confirming the important role played by the solid content on porosity independently of the particle architecture.

2.4. Conclusion

The preparation of different monoliths via Reactive Gelation of core-shell colloidal polymer particles has been investigated as a function of two major process parameters: the particle architecture, namely the soft shell thickness compared to the total particle size, and the initial solid content of the polymer latex.

A thick shell is crucial in determining the pore morphology of the final product. Monoliths characterized by bimodal pore size distribution and up to 10% larger porosity have been formed from particles with lower core-to-particle ratio (0.73), whereas monomodal pore size distribution and smaller porosity have been obtained at a higher core-to-particle ratio (0.82). Further increase in the core-to-particle ratio resulted in unstable structures due to very weak particle interconnections. In addition, increasing the shell thickness led to smaller surface areas, with a reduction of approximately 50% when passing from particles with $R_{CP} = 0.82$ to 0.73. The effect of particle architecture on the pore size of the monoliths has been also investigated using smaller particles (total particle size reduced by a factor of 2 while keeping constant the core-to-particle ratios), and the same conclusions were drawn. Therefore, we can conclude that particle architecture, namely core-to-particle ratio, affects the porous properties of the final monolith in a way which is rather independent on particle size.

About the solid content, provided that the right architecture is chosen, highly porous monoliths can be produced by properly decreasing the initial dry solid content.

The latex parameters investigated in this work (i.e. size, architecture, and solid content of the particles in the initial aqueous dispersion) represent a very valuable tool to control the process of monolith formation and its final porous structure. Consequently, Reactive Gelation appears as a very promising technique for the production of porous materials with specific pore size distribution and morphology, which may suit different kinds of applications.

Chapter 3

Preparation of Ultra-Perfusible Chromatographic Materials via Shear-Induced Reactive Gelation

3.1 Introduction

Porous polymers are widely employed in a variety of different applications including separation and purification techniques^{126,127}, catalysis¹²⁸, thermal insulation¹²⁹ and medical tissue engineering¹⁰⁷. Depending on the amount, morphology and mechanical characteristics of the desired porous material, different manufacturing methods are currently in use¹¹¹. For example polymer-based materials with large pores are produced by suspension polymerization with the aid of a pore-generating system, mainly in the form of a porogen¹¹¹. The resulting process involves multiple steps taking place at the same time, thus making the control of the final pore architecture very challenging. Moreover, the porogen is essential for the pore formation but needs to be fully extracted after the reaction, which may be difficult in some cases. Despite the extensive use of this approach, a reliable and comprehensive relationship between the reaction recipe and the morphological properties of the final material is far from being fully established^{114,116,130}. Reactive Gelation, an alternative, porogen-free method for producing rigid macroporous polymer particles has been proposed previously by Marti et al.²⁰ and it enables the preparation of these materials in a closely controlled and step-wise manner. Starting from a stable colloidal suspension of polymer particles, additional monomer and initiator are added in order to swell them. These swollen

particles, usually stabilized by ionic surfactants, are subsequently aggregated by destabilization induced in different ways: by screening the surface charges through the addition of electrolytes (Brownian aggregation), thus reducing the repulsive barrier among the particles, or by providing them enough kinetic energy to overcome the repulsive barrier (shear aggregation)¹⁶. Depending on the selected aggregation method, different products (*e.g.* monoliths or micrometer-size clusters) and different structures in terms of pore size distribution, have been obtained^{16,21}. The last step of the Reactive Gelation consists in a post-polymerization of the previously added monomer/initiator mixture. This way the primary particles are more strongly bonded together, while retaining the porous structure and improving the mechanical strength and resistance of the final material.

Shear-induced aggregation is performed by exposing the latex to some kind of flow field. If applied without electrolyte addition, this mechanism is called pure shear-induced aggregation¹³¹. Owing to their fractal structure, the aggregates occupy more space while growing, which eventually leads to a percolation and the formation of a gel. It already has been shown¹³² that a fraction of non-aggregated primary particles remains free when such a network is formed, which means that a fully percolating system can be obtained even when the aggregation is not complete. Xie et al.¹³³ showed that this process is affected by the size of both the primary particles and the resulting aggregates. It is also possible to carry out the aggregation process at large conversion while preserving the liquid-like behavior and limiting the system's viscosity increase²¹. This enables the use of continuous processes, which are easily scalable to large productivity. Moreover, the final dispersion of clusters and residual primary particles can be easily diluted by water addition, facilitating the subsequent steps of post-polymerization, wet filtration and packing. The final product can in fact be collected as ready-to-pack slurry of polymer particles in water.

The porous polymers produced in this work are specifically suited for chromatographic applications because they provide high transport efficiency⁶⁰. As a matter of fact, a trade-off between pressure drop

and separation performance is typically observed in chromatographic columns packed with conventional porous particles^{60,127}. In contrast, particles and monoliths produced by Reactive Gelation exhibit pore sizes so large (radii larger than 200 nm) that they permit convective flow through the particle, thus reducing (or even overcoming) the intraparticle diffusion limitations even at relatively large fluid velocities⁵⁸. This allows using large particles, thus with low pressure drop and high flowrates, while avoiding mass transfer limitations. This behavior is known as perfusion and it enables flow-independent separation performance^{61,62}. On the other hand, the major drawback of these materials is their reduced surface area due to the presence of large pores, resulting in reduced binding capacity. This limitation may be overcome when brushes are grown from the pore surface¹³⁴ or nano-particles are used to cover the pore walls if they can be bound in a stable enough manner (*e.g.* by exploiting electrostatic interaction)⁶⁷. In both cases, the effective surface area is increased, thus increasing the chromatographic performance.

In this work, a high-throughput method for producing highly porous and mechanically resistant polymer particles via Reactive Gelation is presented. The primary particles are aggregated through pure shear-induced aggregation by pumping the latex through a microfluidizer, followed by post-polymerization. A comprehensive analysis of the effect of different features of the primary particles (architecture and size) on the morphology of the final material and its performance as chromatographic matrix is conducted, aiming at identifying the optimal operating conditions required to fulfill desired specifications. Pulse chromatography experiments using tracers of different sizes have been run on the produced materials and a comparison with commercially available resins is presented. Due to their most interesting behavior, namely flat HETP profiles resembling those typical of monoliths, we labelled these novel materials as Ultra-Perfusives.

3.2 Experimental

3.2.1 Materials

The following chemicals have been employed without further treatments: styrene (STY, Sigma Aldrich, 4-ter-butylcatechol as stabilizer, purity ≥ 99 wt%), divinylbenzene (DVB, Sigma Aldrich, technical grade, > 80 wt%), sodium dodecyl sulfate (SDS, Sigma Aldrich, BioUltra ≥ 99 wt%), potassium persulfate (KPS, Fluka, purity ≥ 99 wt%), 2-2'-azo(2-methylpropionitrile) (AIBN, Fluka, purity ≥ 98 wt%), sodium chloride (for analysis, Merck), sodium phosphate dibasic, sodium phosphate monobasic (Sigma Aldrich). Dextran standards with different molecular weights (Sigma Aldrich) have been used for packing testing. Ultra-pure grade water has been prepared by Millipore Synergy (Millipore, Billerica, MA, U.S.A.). Deionized water to be used for the polymerization reactions has been de-oxygenated by degassing under vacuum and subsequent saturation with nitrogen. Commercial resins POROS[®] 50 HS and Eshmuno[®] CPX have been purchased from ThermoFisher Scientific and Merck respectively and have been packed following the packing procedures provided by the manufacturers. The monolith CIM[®] r-Protein A DISK has been purchased from BIA Separations and used following the instructions of the producer.

3.2.2 Synthesis of the Primary Particles

The primary particles are produced via a semi-batch emulsion polymerization protocol. The procedure is divided into two steps: core and shell synthesis. In the first phase a hard, highly crosslinked (20 wt%) seed of nanoparticles is produced. In the second step, a much softer, slightly crosslinked (1 wt%) shell is grown around the previously formed particles. These two steps are done in series, thus feeding the monomer mixture required for the shell production directly after completion of the core synthesis.

Several latexes have been produced with different particle architectures. Namely, the ratio between core and overall particle radii as well as the total particle sizes were varied. Details of all the recipes used in each synthesis are reported in Appendix B, while the applied general procedure is presented hereinafter.

Core Synthesis

A mixture of water and surfactant (SDS) is initially charged into the glass reactor and the temperature set to 70°C (Initial Charge, IC). Once this set-point is reached, a solution of water and initiator (KPS) is injected (Initiator Shot 1, IS1). In order to guarantee starved polymerization conditions, an emulsion of styrene, DVB, water, and surfactant is fed over the reaction time using an HPLC pump (Charged Feed 1, CF1). Moreover, a solution of water and KPS is continuously fed as well, as the total reaction time is longer than the half-life time of the initiator at the reaction temperature (Initiator Feed, IF). The conversion is frequently measured to ensure monomer-starved conditions.

Shell Synthesis

A new monomer solution (Charged Feed 2, CF2), this time composed only of styrene and DVB, is then fed to the system right after terminating the core synthesis in the same reactor. The previous initiator feed is disconnected, while a shot of water and KPS is added to keep the reaction running (Initiator Shot 2, IS2). Again, the conversion is monitored to ensure starved operation. After the new monomer addition is complete, the synthesis is left running in batch until full conversion is obtained.

Latex Characterization

During production, the latex is monitored in terms of particles size distribution (by dynamic light scattering (DLS) using a Zetasizer Nano ZS from Malvern) and monomer conversion (from the dry mass fraction of the sample). In the latter case, the latex is spread over quartz sand and analyzed at 120°C in air using a HG53 Moisture Analyzer from Mettler-Toledo.

3.2.3 Reactive Gelation

Latex Swelling

Each latex is diluted with deionized water up to the desired dry mass fraction and swollen by an additional mixture made of divinylbenzene and oil-soluble initiator (AIBN, 5 wt%). This mixture swells the outer layer of the particles almost exclusively, because the core is too highly crosslinked. The amount of added monomer is adjusted to be 30 wt% of the polymer mass in the particle shell. The obtained dispersion of swollen particles is then kept under stirring overnight to ensure complete equilibration.

High Shear Destabilization

The swollen latexes are then destabilized using the high shear device HC-5000 (Microfluidics, Westwood, MA, U.S.A.) equipped with a L30Z microchannel (rectangular cross section of 5.76×10^{-8} m², length of 5.8 mm), referred to as “microchannel” in the following. The latex is pumped through it by a membrane pump and micrometer size clusters of primary particles are collected at the outlet. According to the specifications provided by the manufacturer, the generated shear rate $\dot{\gamma}$ (1/s) is correlated to the pressure drop through the channel itself, ΔP , by the following empirical relationship:

$$\dot{\gamma} = 2.27 \times 10^5 \cdot \Delta P^{0.64} \quad (1)$$

where ΔP is the applied pressure drop in bar. This relationship is valid in a range of ΔP values between 80 and 160 bar. In this work all samples have been aggregated using a constant ΔP of 120 bar, corresponding to a flow rate in the channel of 918 mL/min, a residence time of 0.94 ms, and a shear rate of 4.8×10^6 1/s.

It is worth mentioning that the limiting factor of the setup to form aggregates is the operational limit of the pump. It was in fact observed experimentally that flooding occurs when a latex with too high dry solid content is passed through the microchannel, with head and piston housing clogged by polymer. Such clogging affects the process and the product quality significantly. Therefore, the dry solid content

of the latexes was kept at 7.5 wt% and the suspension of aggregates leaving the microchannel is immediately diluted about ten times in deionized water and transferred into a three-neck flask. This way, the aggregates remain completely wet (preventing air contact) and fully segregated during the post-polymerization phase, thus avoiding the formation of polymer lumps. The aggregation extent (called “conversion” in the following) is measured by quantifying the mass fraction of aggregates with respect to the initial mass of polymer. This is done by precipitating the aggregates from the continuous phase by centrifugation and separating them from the residual primary particles (and very small aggregates), after which they are dried and weighted.

Post-polymerization

The clusters of primary particles produced by aggregation in the microchannel are kept together only by Van der Waals forces. In order to improve the mechanical properties of the aggregates, an additional polymerization step (called post-polymerization) is carried out taking advantage of the monomer added during the swelling step before the high-shear treatment. The three-neck flask containing the aggregates is immersed in an oil bath, connected to a reflux condenser, and kept under gentle stirring (100 rpm) and mild flow of nitrogen. Then, the temperature is raised to 70°C, the nitrogen flow is stopped after one hour and the system is left reacting for at least twelve hours. Finally, the latex is first filtered with a 200 µm mesh to remove possible large polymer lumps, and then dialyzed using a membrane with 10 µm mesh for approximately half an hour to clear out residual primary particles.

3.2.4 Packing

The produced materials are slurry packed into GE Tricorn Columns of 50 mm length and 5 mm inner diameter. The applied packing procedure consists of housing the clusters in the column and in the reservoir, and packing them in water with flow rates up to 9 ml/min. Materials that are not able to

withstand such a high flow rate are not considered of interest and discarded. The commercial resins are packed in the same housings following the procedures reported by the supplier. Monoliths are acquired prepacked and fitted in suitable housings.

3.2.5 Product Characterization

As the aggregates produced are in micrometer range, their size and internal structure is characterized by static light scattering (SLS). Samples are highly diluted and then analyzed using a Mastersizer 2000 (Malvern Instruments, Worcestershire, UK). The scattered light intensity can be used to evaluate the average structure factor $\langle S(q) \rangle$ of the aggregates, defined as⁸⁸:

$$\langle S(q) \rangle = \frac{I(q)}{I(0)P(q)} \quad (2)$$

where q is the magnitude of the scattering vector (defined as $\frac{4\pi n}{\lambda} \sin\left(\frac{\theta}{2}\right)$, where n is the refractive index of the continuous phase, λ is the wavelength in vacuum, and θ is the scattering angle), $I(0)$ the scattered intensity at zero angle, $I(q)$ the angle-dependent scattered intensity and $P(q)$ the form factor of the primary particles measured using the same instrument. In order to relate the average structure factor to the radius of gyration, the Guinier approximation is used⁸⁸:

$$\langle S(q) \rangle = \exp\left(-\frac{q^2 \langle R_g^2 \rangle_{S(q)}}{3}\right) \quad (q \langle R_g \rangle_{S(q)} < 1) \quad (3)$$

where the root-mean square radius of gyration of the aggregates, $\langle R_g^2 \rangle$, and the radius of gyration of the primary particles, $R_{g,p}$, are expressed as $\langle R_g^2 \rangle = \langle R_g^2 \rangle_{S(q)} + \langle R_{g,p}^2 \rangle$ and $R_{g,p} = \sqrt{3/5} R_p$, respectively. Therefore, a rough evaluation of the average cluster size in terms of radius of gyration ($\langle R_g \rangle$) is obtained from the position of the bending of the curve in the double logarithmic plot. Note that the contribution of the primary particles is significant only for aggregates of small size and, therefore, it is not relevant in

our case, where clusters with average size of several micrometers are produced and the residual primary particles have been removed. The same measurement technique provides additional information about the internal structure and the fractal dimension (d_f) of the aggregates. Rayleigh-Debye-Gans theory may be applied where the power-law region of the average structure factor $\langle S(q) \rangle$ plotted as a function of q on a double logarithmic plot yields a straight line whose slope is equal to $-d_f$, *i.e.*, $\langle S(q) \rangle \propto q^{-d_f}$. If clusters are compact enough, the particle size distribution can be derived as well by applying Mie theory, which assumes that the particles are spherical.

The overall surface area of the produced materials is evaluated by nitrogen adsorption measurements through the Brunauer-Emmett-Teller (BET) equation. Two different instruments were used, TriStar3000 (Micrometrics, Norcross, GA, U.S.A.) and Quadrasorb (Quantachrome, Odelzhausen, Germany).

Pore size distribution and total porosity of the aggregates is measured by mercury intrusion porosimetry (equipment Pascal 140 and Pascal 440, Thermo Scientific, Waltham, MA, U.S.A.). In several samples, a clear distinction between internal and external porosity cannot be made in the measurements. Therefore, pores bigger than those intruded by Hg at atmospheric pressure (*i.e.*, equal to or larger than 15 μm according to the Washburn equation) are considered as external voids.

Visual inspection of the aggregates is performed by Scanning Electron Microscopy (Gemini 1530 FEG, Zeiss, Oberkochen, Germany).

Finally, direct characterization of the produced material, as well as of the commercial resins and monoliths is carried out by applying inverse size-exclusion chromatography (ISEC) of suitable tracers to the columns. Pulses of dextrans (polymerized anhydroglucose) in water (25mM, pH 7, phosphate buffer) of different molecular weights are injected at different flow rates to determine the total porosity and the maximum accessible pore size for each material after packing, as well as the dependence of the column efficiency on the flow rate in terms of height equivalent to the theoretical plate (HETP). All of the

chromatographic analyses are run using a high performance liquid chromatography (HPLC) unit equipped with auto-sampler, refractive index detector, UV diode-array detector, and isocratic pump (Agilent Series 1100, Agilent Technologies, Santa Clara, CA, U.S.A.). The pressure drop of each column is also measured at different flow rates using the manometer of the HPLC pump.

3.3 Results and Discussion

3.3.1 Production of Porous Materials

Flowing through the microchannel the particles are provided with enough kinetic energy to overcome the energy barrier due to electrostatic repulsion¹⁶. Therefore in the high shear region of the channel, primary particles as well as already formed clusters undergo aggregation. Since the aggregation rate constant is proportional to the third power of the size of the colliding objects, the interaction between large objects is highly favoured¹³⁵. At the same time, the largest clusters may break under the action of the hydrodynamic stress²⁸. Eventually, a dynamic equilibrium between size increase by aggregation and reduction by breakage is established. Considering the swelling of the outer layer of the particles, which reduces the glass transition temperature of the polymer considerably¹²³, the particles within the clusters interpenetrate to different extents depending on the shell thickness¹²⁴. This phenomenon has an effect on the aforementioned interplay between aggregation and breakage as well.

During the post-polymerization process, a strong interconnection is formed among the nanoparticles within a single cluster through the polymerization of the additional monomer present in the interpenetrating region of the neighboring particles. Their structure becomes mechanically more resistant and thus suitable for chromatographic applications. In the following only materials which could be packed in a column have been considered. Since many parameters, namely the core-shell particle

architecture and the particle size, affect the resulting characteristics of the produced materials, different latexes, listed in Table 3.1, have been synthesized and characterized. The influence of each parameter on the properties of the final clusters is discussed in the following.

Table 3.1. Summary of the properties of the considered latexes.

Latex	Core Size (nm)	Particle Size (nm)	$\frac{\text{core size}}{\text{particle size}}$
L80/110	80	110	0.73
L90/110	90	110	0.82
L100/110	100	110	0.91
L41/56	41	56	0.73
L53/73	53	73	0.73

3.3.2 Structure Characterization

Effect of Particle Architecture

The clusters formed from latexes L80/110, L90/110 and L100/110 (different core-to-particle size ratio, same particle size) are considered first. Note that the core is highly crosslinked (20 wt% DVB) and thus impenetrable to the swelling monomer. On the other hand, the monomer can easily penetrate the much softer shell (1 wt% DVB).

Under the effect of shear (while passing through the microchannel), the polymer nano-particles are destabilized and aggregate in macroscopic clusters. The core-to-particle ratio has a clear influence on the extent of aggregation (conversion) and indeed the thicker the shell, the larger the number of clusters

formed. The presence of a soft shell on the particles surface allows them to undergo a deeper interpenetration upon collision, making the aggregation events very efficient and almost irreversible. Indeed the same effect also increases the resistance to breakage (Figure 3.1). On the other hand, the residence time within the microchannel is not long enough to guarantee full aggregation and primary particles remain in all cases. Not surprisingly, the thicker the shell, the larger are the resulting aggregates, as illustrated in Figure 3.2, where the different cluster size distributions are reported. This conclusion reinforces the mechanism described previously, whereby the degree of interpenetration between the primary particles increases the mechanical stability of the aggregates. This is further supported by SEM images (see Figure 3.3), in which different interpenetration depths between different primary particles is evident. While the primary particles are visible and recognizable in the case of clusters made from L90/110 and L100/110, they almost lose their identity in the case of latex L80/110. Moreover, the morphology in terms of fractal dimension is not affected much by the different particle architecture and only small variations are visible. Indeed, a value of fractal dimension of 2.5 ± 0.1 has been estimated for all samples by SLS analysis.

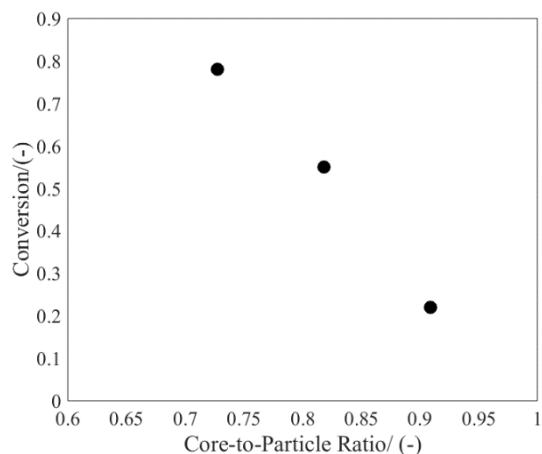


Figure 3.2. Aggregation extent (conversion) as a function of the core-to-particle ratio (same particle size, 110 nm).

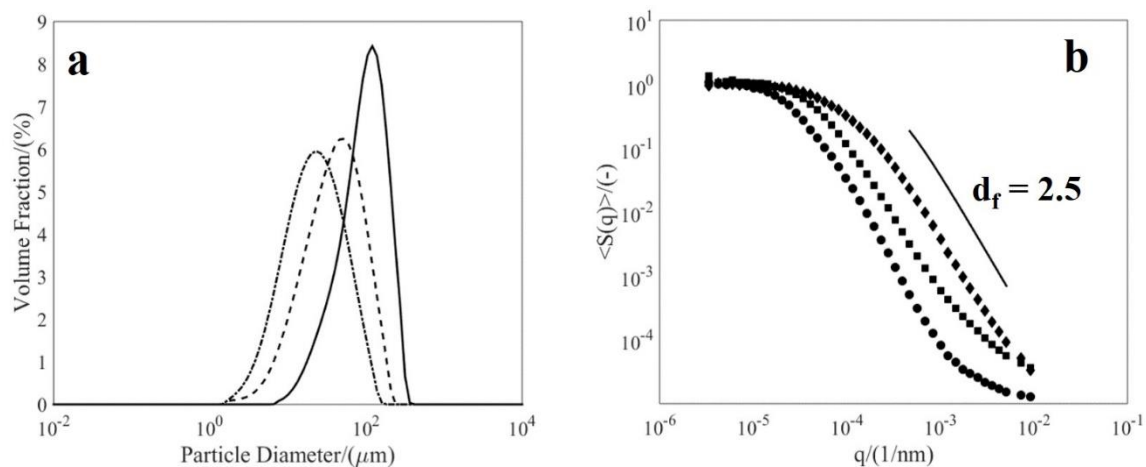


Figure 3.3. Particle size distribution (a) and structure factor curve (b) for clusters produced from particles with different architecture and constant size. Solid line and black dots for L80/110, dashed line and black squares for L90/110 and dotted line and black diamonds for L100/110.

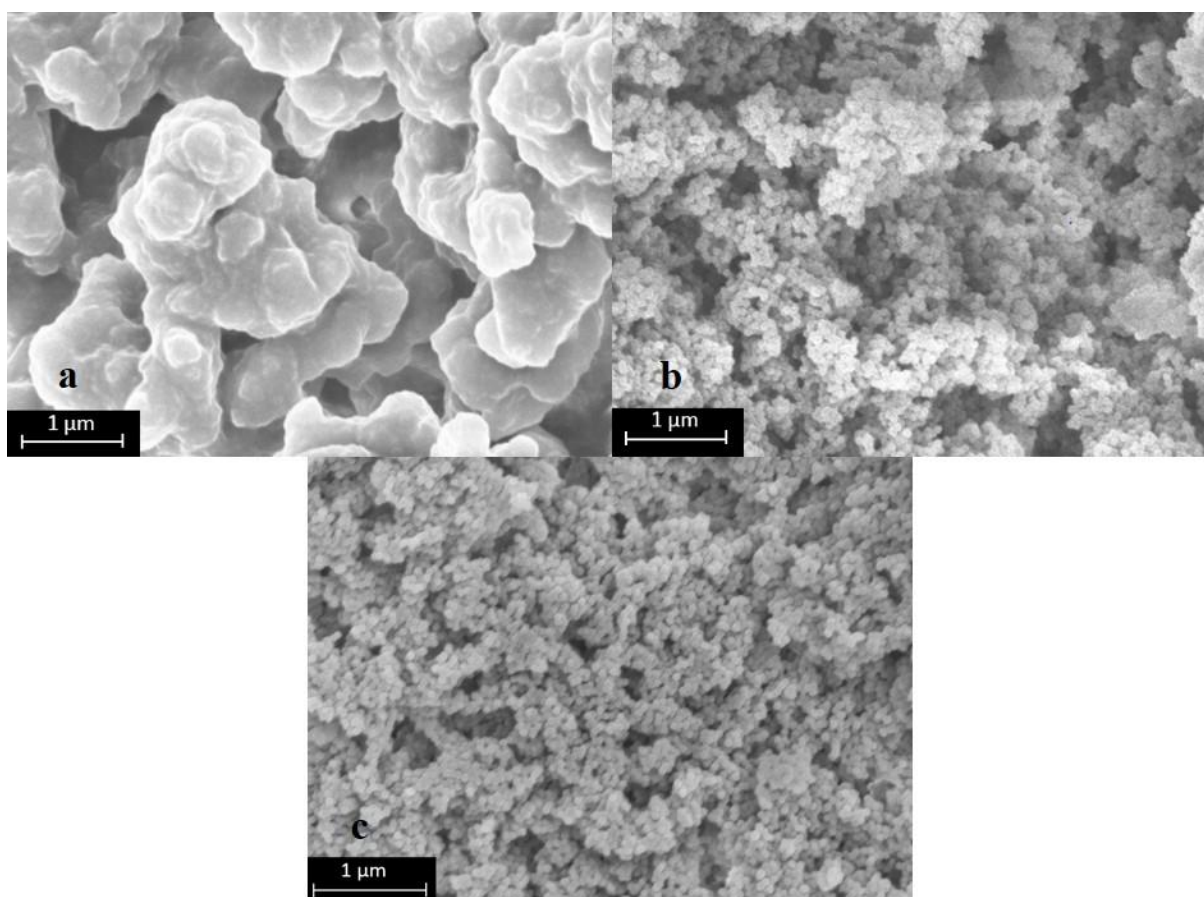


Figure 3.3. SEM pictures of the three different samples produced from L80/110 (a), L90/110 (b) and L100/110 (c).

Table 3.2. Properties of the materials produced from particles with different architecture.

Material	$\frac{\text{core size}}{\text{particle size}}$	Max Flow (ml/min)	<Rg> (μm)	d_f (-)
L80/110	0.73	9	55	2.55
L90/110	0.82	4	37	2.5
L100/110	0.91	0.5	23	2.40

The previously produced materials have been slurry packed and their ability to withstand the shear induced by a solvent flowing through at high velocity has been tested. Specifically, the maximum possible flow rate before the material collapses has been measured and the values are reported in Table 3.2. The failure of the matrix resulted into the formation of a compact polymer plug within the column and a dramatic increase in back pressure. In the case of the clusters produced from latex L80/110, no failure could be induced at all and the reported value of 9 mL/min simply corresponds to the maximum flow rate of the pump used. This highlights again the strong role that the interpenetration among the particles, which is favored by the presence of a thick outer shell, plays in determining the mechanical strength of the resulting clusters.

Effect of Particle Size

In this section the clusters formed from latexes L80/110, L53/73 and L41/56 (core-to-size ratio constant and equal to 0.73, but different particle size) are investigated. The same architecture, including crosslinked core (20 wt% DVB) and much softer shell (1 wt% DVB) is considered.

Figure 3.4 shows the conversion measured with respect to the primary particle size. As expected, larger particles leads to higher extent of aggregation. The aggregation rate constant within the microchannel is in fact proportional to the third power of the size of the colliding particles, making the interaction between

large objects highly favored¹³¹. This is in agreement with the findings of Xie et al.¹³³, who showed already that a lower cluster volume fraction, and thus a lower conversion, is required for smaller particles to achieve gelation at the outlet of the microchannel. About the morphology of the clusters, Figure 3.5 confirms that in fact the core-to-particle ratio is the parameter dominating the final characteristics of the materials. Clusters with very similar size and morphology in terms of fractal dimension are obtained when using primary particles of different size but identical architecture. This is because it is the high degree of interpenetration among the primary particles that makes the clusters more prone to aggregation and more resistant to breakage during the whole process.

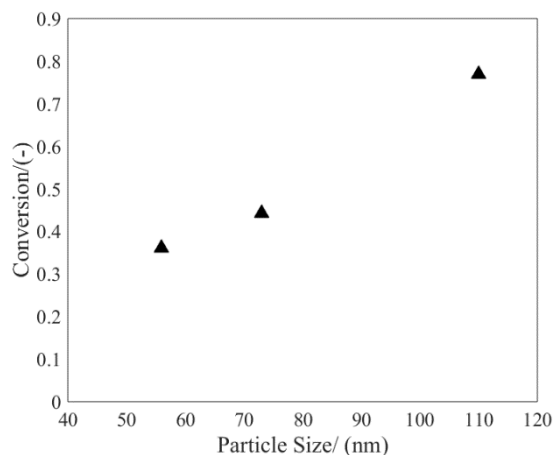


Figure 3.4. Aggregation extent (conversion) as a function of particle size.

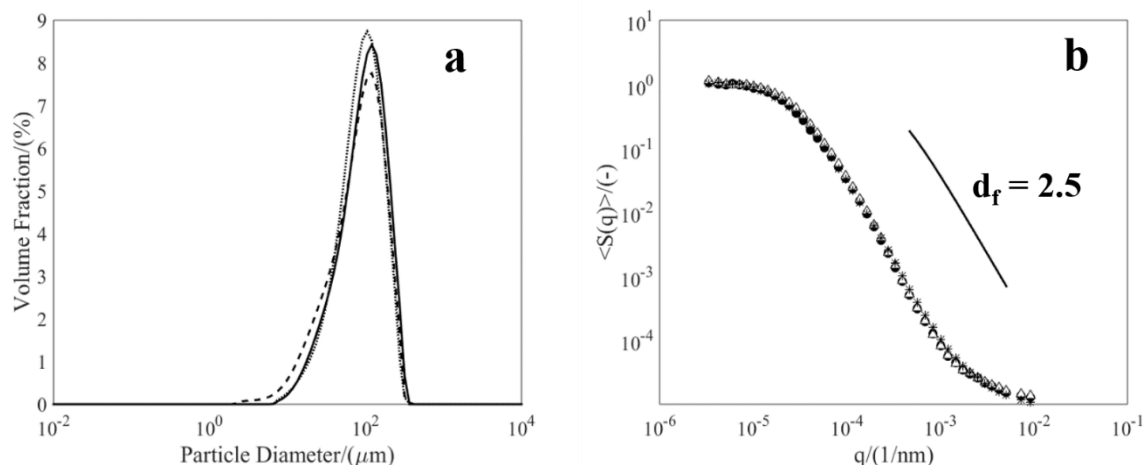


Figure 3.5. Particle size distribution (a) and structure factor curve (b) for clusters produced from particles with different size and same architecture. Solid line and black dots for L80/110, dashed line and white triangles for L53/73 and dotted line and asterisks for L41/56.

This second set of materials has also been slurry packed following the procedure previously described. Once housed in the column, all of these clusters were able to easily withstand a flow rates of up to 9 mL/min without collapsing and with extremely low backpressure.

This is clearly due to the deep interpenetration among the primary particles which however also reduces the surface area. In Table 3.3 the values obtained by nitrogen physisorption are reported, showing that values equal to or below $10 \text{ m}^2/\text{g}$ are obtained in all cases. This means that such interpenetration closes most of the smaller pores, leaving only very large pores within the clusters. This result is also confirmed by the mercury intrusion curves reported in Figure 3.6 for all the samples. Evidently, no pores under $0.1 \mu\text{m}$ are detected and basically all of the available porosity falls in the range between $0.5 \mu\text{m}$ to several micrometers. In light of these results, we can regard these packed materials in the column as a framework composed of very hard particles (after post-polymerization, the degree of crosslinking within the cluster domain is very high) with extremely large pores. Not surprisingly, such a system is able to withstand extremely high flow rates with very low backpressure. The presence of such huge pores is confirmed also by the SEM pictures shown in Figure 3.7.

Table 3.3. Summary of the characteristics of materials produced from particles with identical architectures but different sizes.

Material	$\frac{\text{core size}}{\text{particle size}}$	Max Flow (ml/min)	$\langle Rg \rangle$ (μm)	df (-)	Surface Area (m^2/g)
L80/110	0.73	9	55	2.55	1.7
L53/73	0.73	9	55	2.55	2.9
L41/56	0.73	9	55	2.55	10

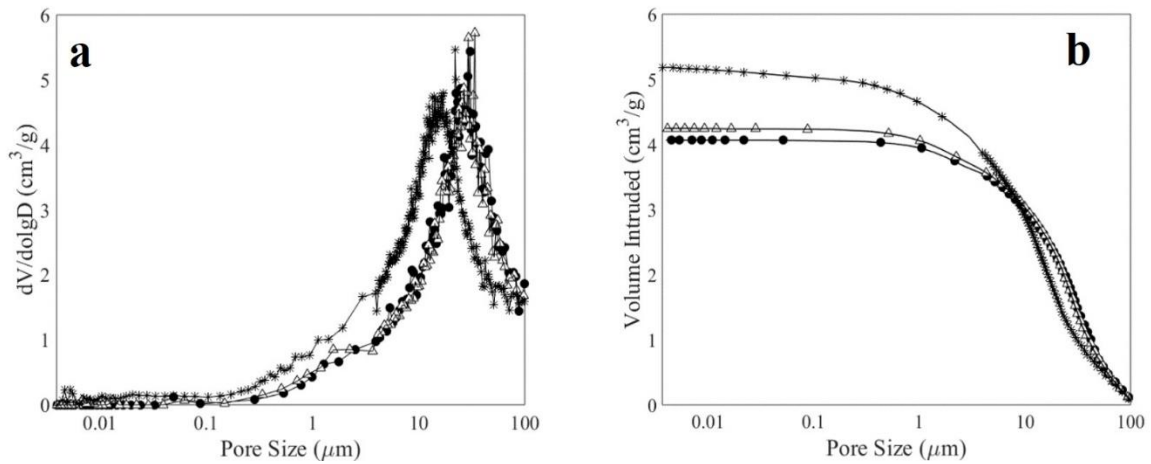


Figure 3.6. Differential (a) and cumulative (b) pore size distribution for the materials produced from latex L80/110 (black dots), L53/73 (white triangles) and L41/56 (asterisk).

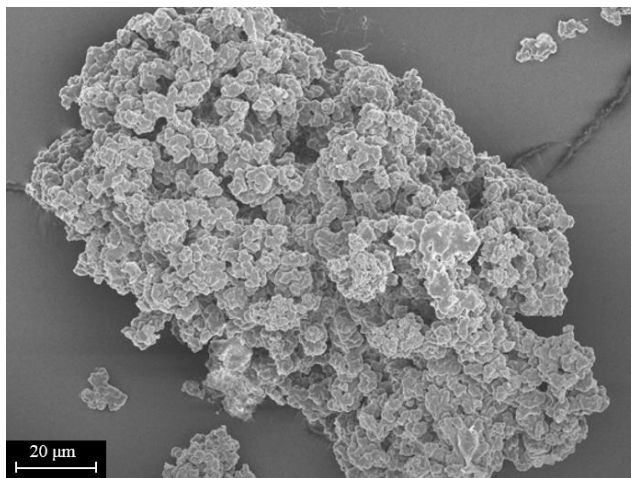


Figure 3.7. SEM picture of a cluster produced using the microchannel using latex L80/110.

3.3.3 Chromatographic Characterization

Packing Characteristics

As already shown, the produced stationary phases that are able to withstand the applied packing procedure have average particle sizes in the range of 100 micrometers in diameter and pore sizes up to several micrometers. These characteristics make them considerably different from the most popular commercial materials, such as Eshmuno CPX, POROS 50 HS and the monolithic CIM® r-Protein A DISK, as can be seen from the comparison of average particle and pore sizes shown in Table 3.4.

The pressure drop data shown in Figure 3.8 indicates that the commercial materials exhibit considerably larger pressure drops. This difference can be imputed not only to the obvious effect of the smaller particle size, but also to the lower fraction of very large pores.

In Figure 3.9, the column porosity for all the investigated stationary phases measured by SEC is shown as a function of tracer molecular weight (dextrans), which correlates with its hydrodynamic radius¹⁰². As expected, the porosity of the commercial materials decreases for bigger dextran species, because the smaller pores exclude larger molecules. This exclusion is not observed for our materials: indeed, they always exhibit constant value of porosity above 85% independently of the tracer size. This is in

agreement with the results of mercury intrusion measurements, which already showed the presence of very large pores and large void fractions in the clusters. This confirms that, compared to the commercial materials, the technology based on Reactive Gelation allows producing pore size distributions centered on larger average sizes, thus excluding the formation of smaller pores.

Table 3.4. Structure characteristics of the materials used in the chromatographic studies.

Material	Average Particle Diameter (μm)	Pore Diameter (μm)
L80/110	110	1 – 10
L53/73	110	1 – 10
L41/56	110	1 - 10
POROS 50 HS	50	0.05 – 1
Eshmuno CPX	50	< 0.3
CIM® r-Protein A DISK	-	1.5

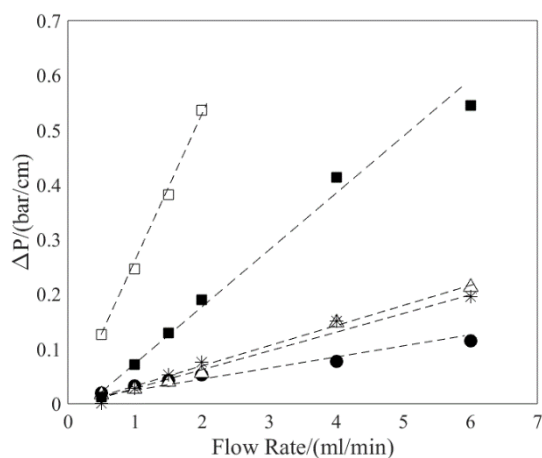


Figure 3.8. Pressure drops for all the packed materials: Eshmuno CPX (white squares), POROS 50 HS (black squares), L80/110 (black dots), L53/73 (white triangles) and L41/56 (asterisks). Dashed lines are shown to guide the eye.

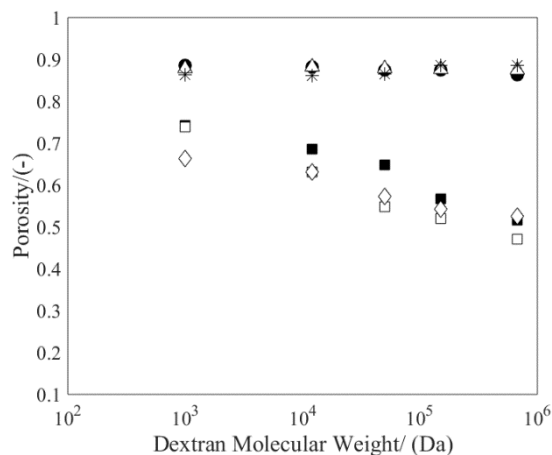


Figure 3.9. Porosity measured using tracers with different size for all the packed materials: Eshmuno CPX (white squares), POROS 50 HS (black squares), CIM® r-Protein A DISK (white diamonds) L80/110 (black dots), L53/73 (white triangles) and L41/56 (asterisks).

Intraparticle Mass Transfer Resistance

The HETP values of each of the packed columns have been measured using tracers at different molecular size under non-adsorbing conditions. In particular, dextrans with molecular weights of 12 kDa (Dex12000) and 150 kDa (Dex150000) have been chosen as representative of typical sizes of large biomolecules (2.9 nm and 9 nm of hydrodynamic radius, respectively), the purification of which is one of the main applications of preparative chromatography in industry. As shown in Figure 3.10a, the HETP values of both Eshmuno CPX and POROS 50 HS increase with the flow rate for the smallest species (Dex12000), meaning that the column becomes less efficient at larger flow rates. On the other hand, all our materials exhibit HETP values almost constant with the flow rate, a behavior very comparable to that of the monolith CIM® r-Protein A DISK. Even though the efficiency of the monolith remains larger, the flow-independent behavior of our packings is quite remarkable. In this sense, our material show an extremely perfusive characteristic that we labelled as Ultra-Perfusive. In the case of the largest tracer (Dex150000), Figure 3.10b shows increasing HETP values at increasing flow rates for Eshmuno CPX, whereas some flattening is observable for POROS 50 HS, given the perfusive nature of that material.

Once again, all our materials all behave as the monolith, showing a flat HETP profile for all considered flowrates, justifying even more our previous definition.

Although the measured HETP values are smaller for the monolith than for our materials, the latter offer the key advantage of an easy packing into conventional columns, without the requirement of special housings. This aspect represents a major advantage in terms of versatility and broadens the range of possible applications of materials produced through shear-induced Reactive Gelation.

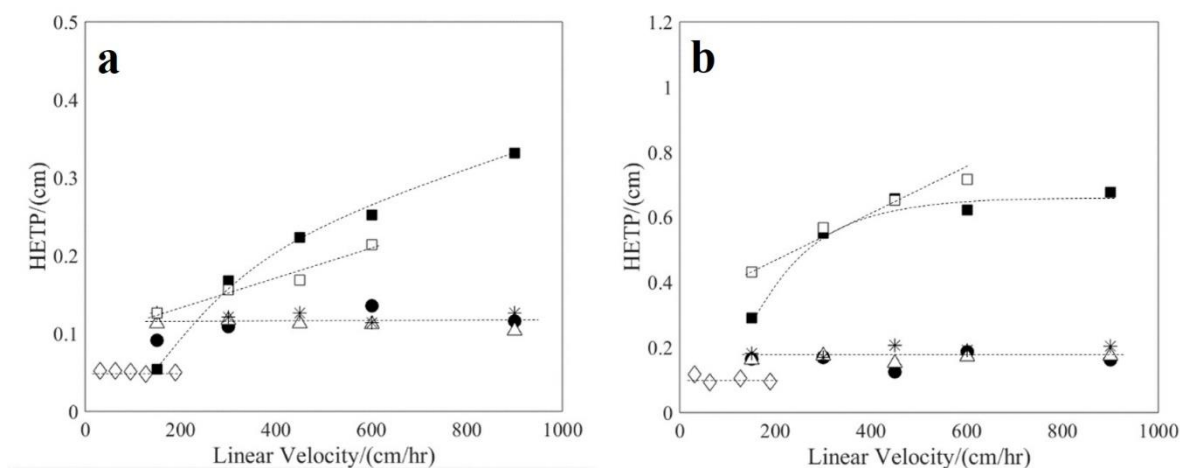


Figure 3.10. HETP as a function of flow rate for the species Dex12000 (a) and Dex15000 (b): Eshmuno CPX (white squares), POROS 50 HS (black squares), CIM® r-Protein A DISK (white diamonds) L80/110 (black dots), L53/73 (white triangles) and L41/56 (asterisks). Dashed curves are shown to guide the eye.

3.4 Conclusion

In this work, the effects of different properties of the primary particles on the final properties of porous clusters produced by Reactive Gelation under shear have been investigated. In particular, the effects of core-to-particle ratio and particle size have been explored. All the produced materials have been tested as potential chromatographic packings by measuring pressure drops and column efficiencies (HETP) after packing.

While the particle size was found to have little impact, the core-shell architecture of the primary particles affects the size of the produced aggregates and their mechanical resistance to a large extent. As a matter of fact, a small core-to-particle ratio is required to achieve highly porous materials able to withstand high flow rates after packing with small pressure drops.

Considering the chromatographic efficiency of columns packed with these materials, their nature enables flow rate independent HETP values. This achievement is a consequence of the large pore size, up to several micrometers, which makes the contribution of convective flow through the clusters dominate the mass transfer. Notably, flat HETP profiles resembling those typical of monolithic packings have been observed when large dextran tracers have been eluted. Moreover, comparison with similar commercial packings shows that shear-induced Reactive Gelation produces porous materials with better pressure drop and mass transfer properties, particularly with respect to their perfusion characteristics, that is HETP values which remain constant for increasing fluid velocity. This consideration allows their definition as Ultra-Perfusive and makes the materials produced in this work extremely promising as efficient and easy-to-pack base scaffolds suitable for further functionalization. This last step will make them specific to the required separation target and partly compensate for the reduced specific area associated with the large pore sizes.

Chapter 4

Synthesis of Monodisperse, Porous, Rigid, Hollow and Spherical Polymeric Capsules Combining Microfluidics and Reactive Gelation

4.1 Introduction

Porous materials in the form of microscale particles (MPs) with well-controlled morphology are of great interest in polymer and material science⁸⁶ as they find major applications in different fields including separation and purification techniques¹³⁰, catalysis¹⁰⁹, thermal insulation¹²², drug delivery and medical tissue engineering¹⁰⁷. Conventional synthesis techniques are based on suspension polymerization in the presence of a porogen¹¹¹. On the other hand, a major versatility can be introduced by the usage of colloidal approach^{19,21,23,51,136}. Thanks to self-organization of colloidal particles at fluid-fluid interfaces^{47,49}, templating^{40,137} and controlled aggregation¹⁶, the final MPs evolved from the classical full-spherical shapes towards more complex structures. In this way, porous MPs in the forms of crystals⁴⁵, capsules¹³⁶, hollow shells⁴⁴ and not spherical templated arrangements^{138,139} have been produced and applied in different fields. A major role among this secondary generation of porous MPs is played by colloidosomes⁵¹. Defined as microscale capsules whose shell is composed of colloidal polymer particles, they find major applications in microencapsulation and triggered release. The classical production

methodology⁵⁷ takes advantage of the self-assembly of colloid particles at oil/water interface, occurring spontaneously and producing very stable emulsions (Pickering emulsion³⁵). Therefore, the porosity is given by the interstitial spaces between the individual colloidal particles and by the defects in their arrangement on the surface. In order to make these MPs usable in practical applications, a step to harden the structures and to provide mechanical resistance is required⁵⁷. Thermal annealing¹⁴⁰, covalent crosslinking¹⁴¹ and further polymerization at the interface¹⁴² represent valuable options, but for the former, high temperature (*i.e.* above T_g) is required, and for the latter two, it is often difficult to find chemicals compatible for both phases and complex multi-scale protocols⁵⁷. This limits consistently also the scalability of the production process. Another extremely robust path, already implied in the production of mechanically stable porous polymer networks, is represented by Reactive Gelation²⁰. This technique is divided into the following steps: 1) starting from an aqueous dispersion of colloidal polymer nano-particles (so-called latex) swollen by a mixture of monomer and initiator; 2) controlled aggregation or templating is used to let the particles arrange in a defined structure; 3) afterwards a post-polymerization through heating in mild conditions is run to harden and consolidate the previously formed network, ensuring mechanical stability. In general, the permeability of the aforementioned capsules is the key for their use in different applications and is determined by the porosity and the sizes of pores⁵¹. In this sense, the use of microfluidics provides a new pulse to the discipline allowing precise and strict tuning not only of the process parameters, but also of the morphology of the outcomes¹⁴³. Playing with chips design and particles manufacturing enables production of customized ordered or hierarchical porous frameworks with adjustable pore sizes and regular shapes.

In this work, we investigate the possibility of combining reactive gelation and microfluidics to produce monodisperse, rigid, hollow and spherical capsules (MPs) with tunable porosity of the crust, taking advantage of a peculiar self-organization of the primary nanoparticles (NPs) in a jammed state. Moreover, a possible explanation of the physical mechanism controlling the aforementioned behavior is

proposed and verified using a simplified model at atomic scales by means of molecular dynamics simulations. Based on the identified nature of the process, it is possible to design the capsules with rather open or compact shells, playing with the solid content of the NPs in the latex. Furthermore, this last parameter has been correlated with the capsule accessibility by tracking intra-particle diffusion of probe fluorescent molecules. This results in an effective control not only of the shell morphology and appearance of the capsules but also of their suitability for future applications, such as delivery, release and encapsulation.

4.2 Experimental

4.2.1 Materials

The following chemicals have been purchased from Sigma Aldrich and employed without further treatment: styrene (STY, purity ≥ 99 wt%), divinylbenzene (DVB, technical grade, > 80 wt%), sodium dodecyl sulfate (SDS, BioUltra ≥ 99 wt%), sodium phosphate dibasic, sodium phosphate monobasic and fluorescein isothiocyanate-dextran, average mol wt 4000 (FITC-dextran 4000). Sodium Chloride and Potassium persulfate (KPS) were purchased from Merck. 2,2'-azo(2-methylpropionitrile) (AIBN, purity ≥ 98 wt%) was purchased from Fluka. Rhodamine B was purchased from Acros Organic. Ultra-pure grade water has been prepared by Millipore Synergy. All water used in polymerization reaction has been de-oxygenated by degassing under vacuum and subsequent saturation with nitrogen. Fluorinated oil Novec™ HFE-7500 with 0.5 wt% block copolymer fluorosurfactant was purchased from Ran Biotechnologies. Isopropanol was purchased from Fisher Chemicals and used without further treatments.

4.2.2 Emulsion Polymerization

The primary nanoparticles were produced via semi-batch emulsion polymerization procedure, consisting of two steps, namely the core and the shell synthesis. In the first phase, a hard, highly crosslinked (20 wt %) seed of NPs is produced. In the second one, a much softer, slightly crosslinked (1 wt %) shell is grown around the previously formed NPs. These two steps are performed in series, i.e., directly feeding the monomer mixture required for the shell right after completion of the core synthesis, without stopping the reaction. Details about each of the previous stages are reported in the following.

Core Synthesis

A mixture of water and surfactant (SDS) was initially charged into the glass reactor and the temperature set to 70 °C (Initial Charge, IC in Table 4.1). Once this set-point was reached, a solution of water and initiator (KPS) was injected (Initiator Shot 1, IS1). In order to guarantee starved polymerization conditions, an emulsion of styrene, DVB, water, and surfactant was fed over the reaction time using an HPLC pump (Charged Feed 1, CF1). Moreover, as the total reaction time is longer than the half-life time of the initiator, a solution of water and KPS was continuously fed as well (Initiator Feed, IF), at the reaction temperature. The conversion was frequently measured to ensure the monomer-starved conditions.

Table 4.4. Recipe for the production of the core/shell polymer particles latex

	Core				Shell	
	IC	IS1	CF1(14h)	IF (14h)	CF2 (6h)	IS2 (6h)
Water (g)	250	25	29.1	74		20
Styrene (g)			23.3		35.64	
DVB (g)			5.8		0.324	
SDS (g)	0.375		0.58			
KPS (g)		0.75		1.24		0.2
Crosslinker (%)			20		1	
Diameter (nm)			80		107	
PDI			0.03		0.002	

Shell Synthesis

A new monomer solution (Charged Feed 2, CF2), this time composed only of styrene and DVB, was then fed to the system right after terminating the core synthesis in the same flask. The previous initiator feed was disconnected, while a shot of water and KPS was added to the reaction to keep it running (Initiator Shot 2, IS2). Again, the conversion was monitored to ensure the starved operation. After the second monomer addition was complete, the synthesis was left running in batch until full conversion was obtained.

Latex Characterization

During production, the latex was monitored in terms of particle size and particle size distribution by dynamic light scattering (DLS) (Zetasizer Nano ZS, Malvern) and of the monomer conversion based on the dry mass fraction of the sample. For the latter, the latex was spread over quartz sand and analyzed at 120 °C in air using a Moisture Analyzer (HG53, Mettler-Toledo).

4.2.3 Capsules Formation

Latex Swelling

Each latex was diluted with deionized water up to the desired dry mass fraction and swollen by an additional mixture made of DVB and oil-soluble initiator, AIBN (5 wt%). This mixture swells almost exclusively the outer layer (shell) of the NPs, because the crosslinking extent of the shell is substantially smaller than that of the core. The amount of added monomer was adjusted to be 10 wt% of the polymer mass of the shell. The obtained dispersion of the swollen NPs was then kept under stirring overnight to ensure complete equilibration.

Generation of Monodisperse Latex Droplets using Microfluidic Devices

Microfluidic Devices

Figure 4.1 shows schematically the microfluidic channel designs. In particular, the microfluidic circuits were designed using AutoCAD 2014 (Autodesk, San Rafael, USA) and printed onto a high-resolution film photomask (Micro Lithography Services Ltd, Chelmsford, UK). Master structures were subsequently fabricated on SU-8 (Microchem Corporation, Westborough, USA) coated silicon wafers via conventional photolithographic methods. Microfluidic devices were manufactured using standard soft-lithographic techniques. Briefly, a 10:1 wt/wt mixture of polydimethylsiloxane (PDMS) base and curing agent (Sylgard 184; Dow Corning, Midland, USA) was poured over the master structure and cured in the oven at 70 °C for 4 hours. The cured PDMS structure was then peeled off from the wafer, with

inlet and outlet ports being formed using a hole-puncher (Technical Innovations, West Palm Beach, USA). The structured PDMS substrate was then bonded to a 3 mm thick, flat PDMS layer using an oxygen plasma (EMITECH K1000X, Quorum Technologies, East Sussex, United Kingdom). For latex droplet generation chip, the height of all microchannels was 30 μm , and the width of the flow focusing part was also 30 μm . Picoinjection devices were fabricated following the same procedure described above. After bonding of the chip, electrodes were made using a simple liquid-solder approach. The empty microchannels in the shape of the electrodes were previously designed. The device was heated and a low melting-point liquid solder was injected into the channel. By cooling the device the solder was solidified, producing a metallic electrode in the shape of the channel, thus allowing fabrication of high-resolution electrodes.

Latex Droplet Production

A MotionPro Y5 Compact Digital Camera (IDT, Hitchin, United Kingdom) and Nikon Eclipse Ti-E microscopy (Nikon Instruments Europe) were used to monitor and image the droplet formation process. The fluorinated oil Novec™ 7500 (3M, St. Paul, USA) containing 0.5 wt% triblock fluoro-surfactant, a hydrophilic poly(ethyleneglycol) (PEG) block flanked by two perfluorinated tails (RAN Biotechnologies, USA), was used as the carrier phase and the latex containing 0.2 wt% SDS was the segment phase. neMESYS low pressure dosing modules (Cetoni GmbH, Korbussen, Germany) were used to motivate all fluids using 1 ml gastight syringes (Hamilton Bonaduz AG, Bonaduz, Switzerland). Tygon tubing (Cole Palmer, Hanwell, UK) was used to connect syringes to the inlets of the microfluidic device. The latex droplets were formed at the flow focusing part of the chip with various sizes according to different ratios of the flow rates for carrier and segment phases. The picoinjector device was used to induce the coagulation of the primary NPs by injecting sodium chloride aqueous solution with different concentration into the latex droplet. We energized the electrode using 10 kHz, 500 Voltage AC signals generated by an ADS1102CAL⁺ digital storage oscilloscope (ATTEN instruments, China) and amplified

by a high voltage amplifier (TREK Model 2210, USA). The sodium chloride aqueous solution was pumped into the injection channel at a constant pressure using a Mitos P-Pump (Dolomite, UK).

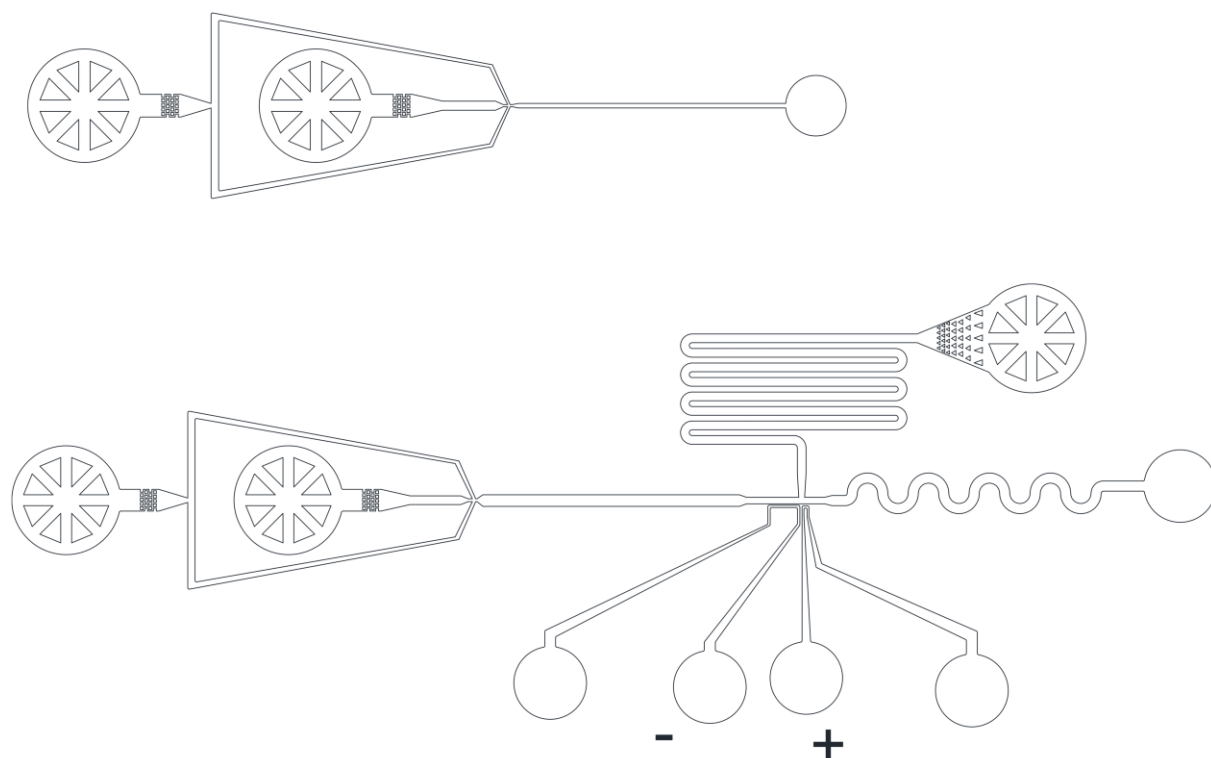


Figure 4.1. Microfluidic channel designs. Upper image: footprint of the device used for latex droplet generation. Lower image: footprint of the picoinjection device for sodium chloride aqueous solution and latex fusion.

Conversion of Latex Droplets to Capsules by Post-polymerization

From the latex droplets generated above, we performed the post-polymerization to fix permanently the formed structure within the droplets, leading to the final capsules. The post-polymerization was conducted by exposing the dispersion at 50 °C overnight, closed either in a plastic capillary or in a 5 ml vial, depending on the actual volume. In general, the former was more desirable than the latter, because it can better preserve the stability of the droplets and avoid any merging. In the case of using a vial, though the productivity can substantially increase, some merging of the droplets and formation of amorphous solid residuals have been recorded. In the present work, both have been applied. After the

post-polymerization, the excess fluorinated oil was removed, and the obtained wet capsules were transferred to an excess of isopropanol in order to wash completely the remaining oil. After the solvent exchange for several times, the capsules were finally fully dried and collected as a powder.

4.2.4 Capsules Characterization

Morphology

During the whole production period, the chip and the droplets were constantly monitored via optical microscopy. Moreover, monodispersity of the capsules after post polymerization and drying was assessed both via optical microscopy (Nikon Eclipse Ti-E) as well as scanning electron microscopy (SEM) using a Gemini 1530 FEG from Zeiss with field emission gun operated at 5 kV. In these last measurements, the coating of the samples was performed using platinum. This last technique has been also used in order to perform visual inspection of the particles surface.

Surface Porosity and Permeability of the Capsules

The surface porosity and the permeability of the capsules were studied both qualitatively and quantitatively by means of fluorescent molecules. Diffusion of rhodamine B within the capsules was followed for different samples via confocal fluorescent microscopy. In particular, capsules were soaked in isopropanol, in which rhodamine B was dissolved. After 24 hours equilibration, the capsules were separated via centrifugation, and repeated solvent exchange was performed. Pictures of the capsules were taken only when the solution was enough limpid to allow the right fluorescence contrast. These observations were performed using a Leica SP8-AOBS confocal microscopy. An Argon laser at 550 nm was used for excitation of the samples and the emitted light was collected using one HyD detector. Bright field images were collected in parallel using a PMT detector. More quantitative measurements were performed by quantifying the penetration via diffusion of species of known size (FITC-dextran 4000,

with Stoke's radius of 1.4 nm) within the individual porous shells. Exact amounts of dried porous capsules (in the range of 1 to 5 mg) were soaked and fully intruded with phosphate buffer at pH 8. Then, they, when still completely wet, were added to 1 ml of the same buffer, in which a known amount of FITC-dextran 4000 was dissolved. This species has a fluorescent label that allows tracking its concentration in a solution by measuring the fluorescent intensity. These measurements were performed using a plate reader (EnSpire 2300 Multilabel Reader, Perkin Elmer). Moreover, this technique is extremely sensitive and a difference of few percentages can be detected. In general, in order to correlate the concentration of FITC-dextran 4000 to the recorded intensity, a calibration with five different known dextran concentrations is required.

In the experimental practice, right after the addition of the capsules, they were quickly sedimented out of the supernatant, and a portion (200 μ l) of the supernatant was taken and used to measure the FITC-dextran 4000 concentration, which was defined as the initial concentration. Afterwards, the capsules were left in the FITC-dextran 4000 solution equilibrating for 24 hours in a fridge, and the same procedure was repeated to quantify the remaining FITC-dextran 4000 concentration in the supernatant. The relative difference in the two concentrations, divided by the initial mass of the dried capsules, was used to quantify the accessibility of the porous shell of the capsules. It is worth mentioning that, due to its chemical structure, FITC-dextran 4000 might have some interactions with the polystyrene surface of the capsule shell and be partially adsorbed. Thus, the recorded variation in the concentration might be the sum of the amount from pure diffusion into the internal hollow domain and the amount from the limited adsorption. On the other hand, all of the capsules were made from the same initial polymer latex, and they should present the same interactions with the FITC-dextran 4000, thus not affecting the conclusion that we can draw from the applications of this technique.

4.2.5 Simplified Model for Individual Primary NPs

The behavior of the individual primary NPs inside the latex droplets produced from the microfluidics has been investigated from a theoretical point of view through a simplified model at molecular scale, by means of molecular dynamics (MD) simulations. The primary NP has been modeled as a flat surface made of amorphous syndiotactic polystyrene, while the water-soluble portion of the surfactant coming from the oil phase but located at the oil-water interface has been modeled as pure polyethylene glycol (PEG). The computational protocol can be divided into three phases; in the first one, an equilibrated polystyrene surface is built. In the second step, the surface is solvated with explicit water molecules and also explicit SDS molecules are added, in order to realize surfactant adsorption and obtain a reasonable input structure of a stabilized surface. In the last phase, the influence of pH on the surfactant/particle interactions is studied. In particular, two different simulations have been performed here: one representative of acidic environment, where PEG oxygen atoms are protonated, and one mimicking neutral/basic pH conditions, where PEG is uncharged. Interaction energies have been computed by means of Molecular Mechanics Poisson Boltzmann Surface Area (MMPBSA) method.

4.3 Results and Discussion

4.3.1 Preparation of Porous Capsules

Using microfluidic devices, the polymer latex, diluted at the desired NP concentration, is housed into stable droplets dispersed in a continuous fluorinated oil phase, which acts as a micro-container. Thanks to the chip design, high monodispersity among the generated droplet is accessible, independently of the initial latex concentration and actual droplet size. In general, droplets in the range from 20 μm to 100 μm in diameter can easily be produced with high degree of monodispersity. Still owing to different chip designs, it is possible to inject into the latex droplets controllable amount of salt (e.g. sodium chloride)

solution, as shown in Figures 4.2a and 4.2b. In Figure 4.2a, the primary polymer NPs in the droplets are destabilized because of the screening of the repulsive energy barrier induced by the injected electrolytes, and aggregation of the primary NPs occurs.

In a general macroscopic system, it is always possible to control the aggregation rate slow enough, in the RLCA regime, so that the system, provided the right NP concentration, can percolate and jam into an arrested non-equilibrium state^{16,144}. This process, often referred to as gelation, results in a liquid to solid transition and the formation of an interconnected framework. Obviously, different shape of a gel can be obtained by tuning the shape of the container in which the percolation occurs. Thus, one would expect that in our case of microscale droplets, the electrolyte injection would result in a transition from a liquid droplet to a solid sphere. However, our experimental results did not confirm this. Though many different salt concentrations have been tested, it was not possible to properly tune the aggregation rate, and the formation of a solid-like sphere as defined by the droplet could not be achieved, as shown in Figure 4.2c, where it is seen that only pieces of gels are formed inside the droplet, which do not have the same shape as the droplet. On the other hand, it was observed that if no salt was added, the primary NPs can self-organize toward the droplet interface, leading to the formation of a solid-like shell, resulting in a hollow sphere of the same shape of the initial droplet, as shown in Figure 4.2d. This obviously indicates some forces present at the oil-water interface, which attract the primary NPs. Moreover, with an extremely low salt concentration, an interesting intermediate state has been also observed, where, apart from the formation of a solid-like shell, a piece of gel is also presented inside the hollow sphere (Figure 4.2f). The latter is obviously related to the salt-induced gelation.

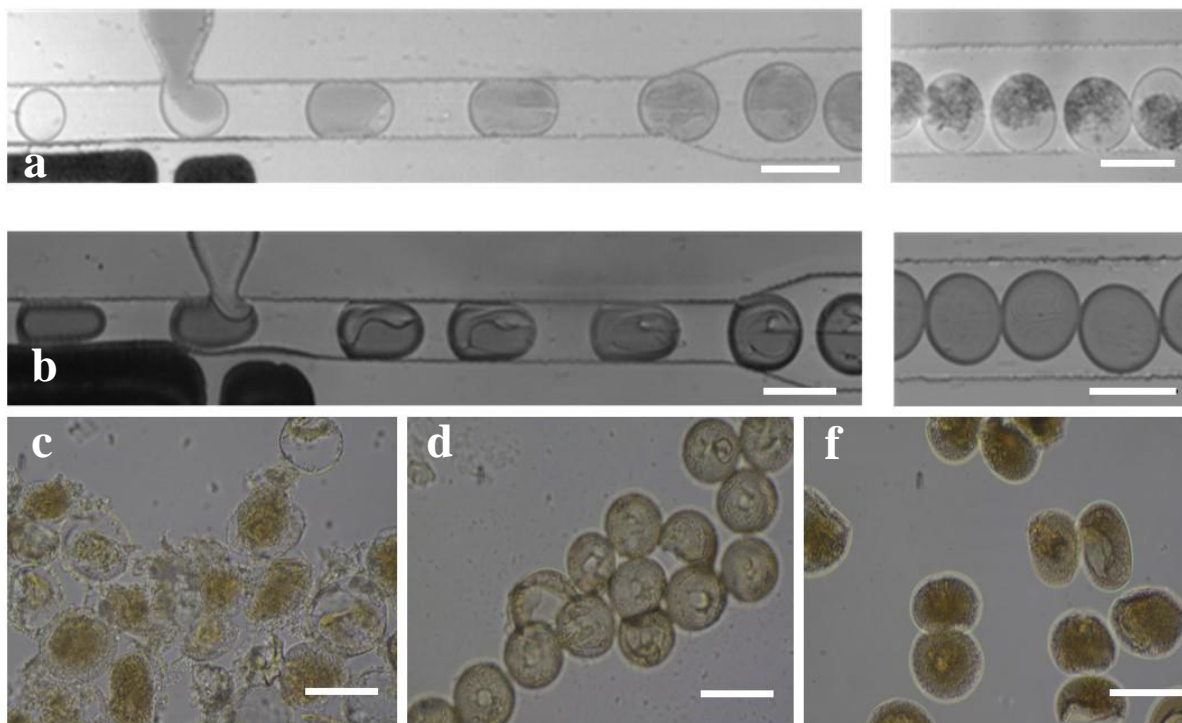


Figure 4.2. a) 1 M sodium chloride aqueous solution (lighter droplet) fused with the latex droplet (darker one) at a volume ratio of 0.7, where a very fast aggregation of the primary NPs occurs on chip; b) 0.3 M sodium chloride aqueous solution fused with the latex droplet at a volume ratio of 0.5, where a slow aggregation of primary NPs was observed on chip; c) Latex droplets injected with a high salt concentration, leading to fast aggregation; d) Formation of a solid-like shell in the droplets without salt addition; f) An intermediate state observed at an extremely low salt concentration, where, apart from the solid-like shell, a piece of gel is also formed inside the hollow sphere. Scale bars: 100 μm .

Among the above mentioned obtainable structures, only the case in Figure 4.2d, i.e., the hollow spheres, is particularly interesting as capsules, thus specifically considered and analyzed in the following. Instead, in the other cases, the morphologies are irregular and difficult to control, thus ignored here. Therefore, the hollow capsules were post-polymerized in order to permanently fix the shell structure, leading to hard, mechanically stable and dryable capsules. Figure 4.3 exhibits typical examples of monodisperse and robust polymeric capsules in different sizes generated in this way.

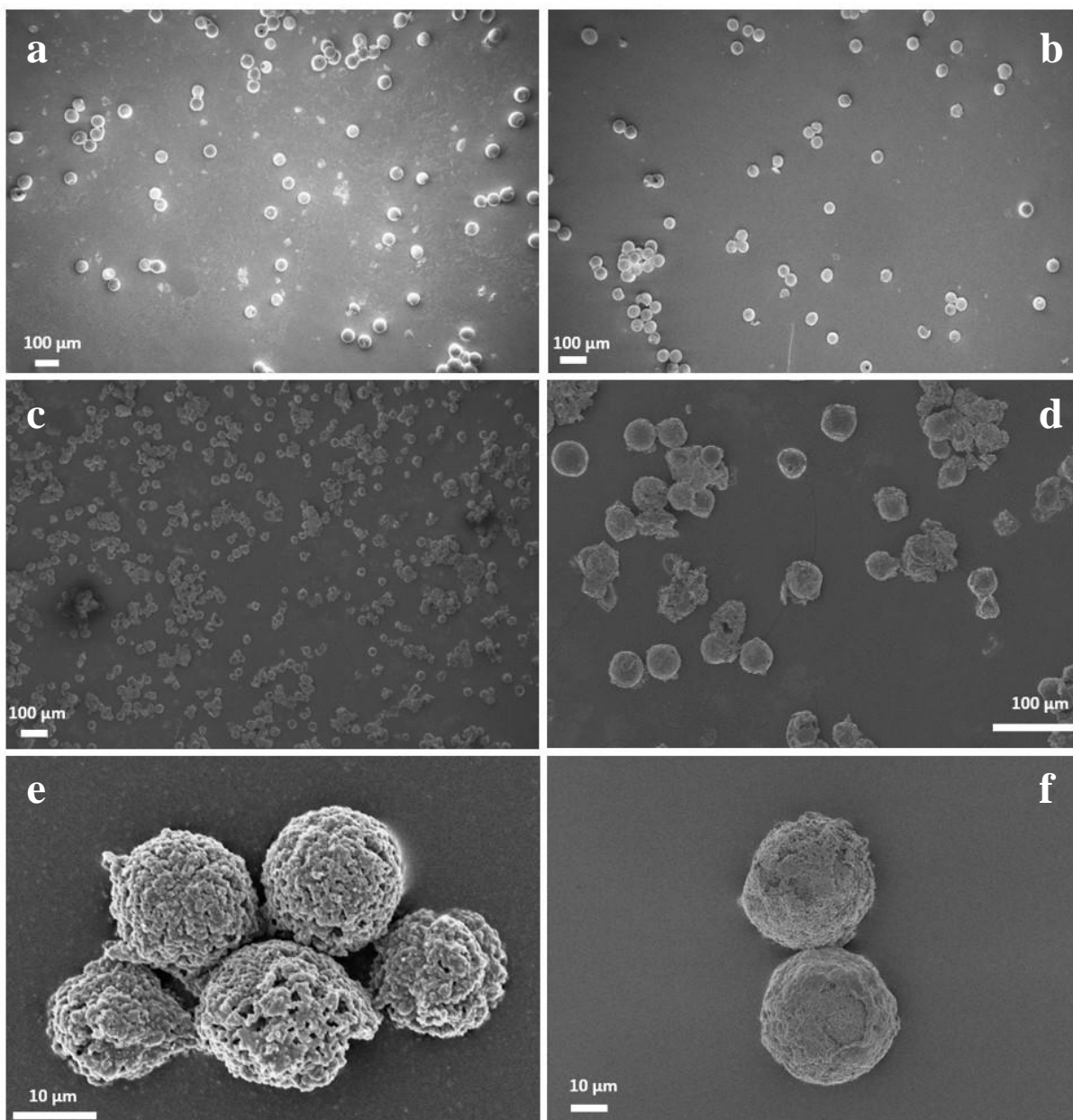


Figure 4.3. Pictures of the porous hollow capsules obtained via microfluidics in different sizes, after post polymerization and drying.

Visual inspection of the final, fully dried capsules via SEM enables us to recognize and establish that the arrangement of the NPs within the shell is jammed rather than ordered, similarly to what occurs during conventional aggregation or percolation. This statement is supported by Figure 4.4, where a rather disordered disposition of the NPs within the shell of the hollow capsules is observable. Moreover, the

NPs partially merge among themselves, and in some cases they almost lose their individual identity. This is due to the presence of the swollen soft shell on the primary NPs, which allows partial interpenetration among them during the aggregation. Then, along the post-polymerization, the additional monomer reacts, forming additional polymer within the interpenetrated region, which reinforces the structure and holds all the NPs together, but at the same time also results in partially losing the identity of the primary NPs.

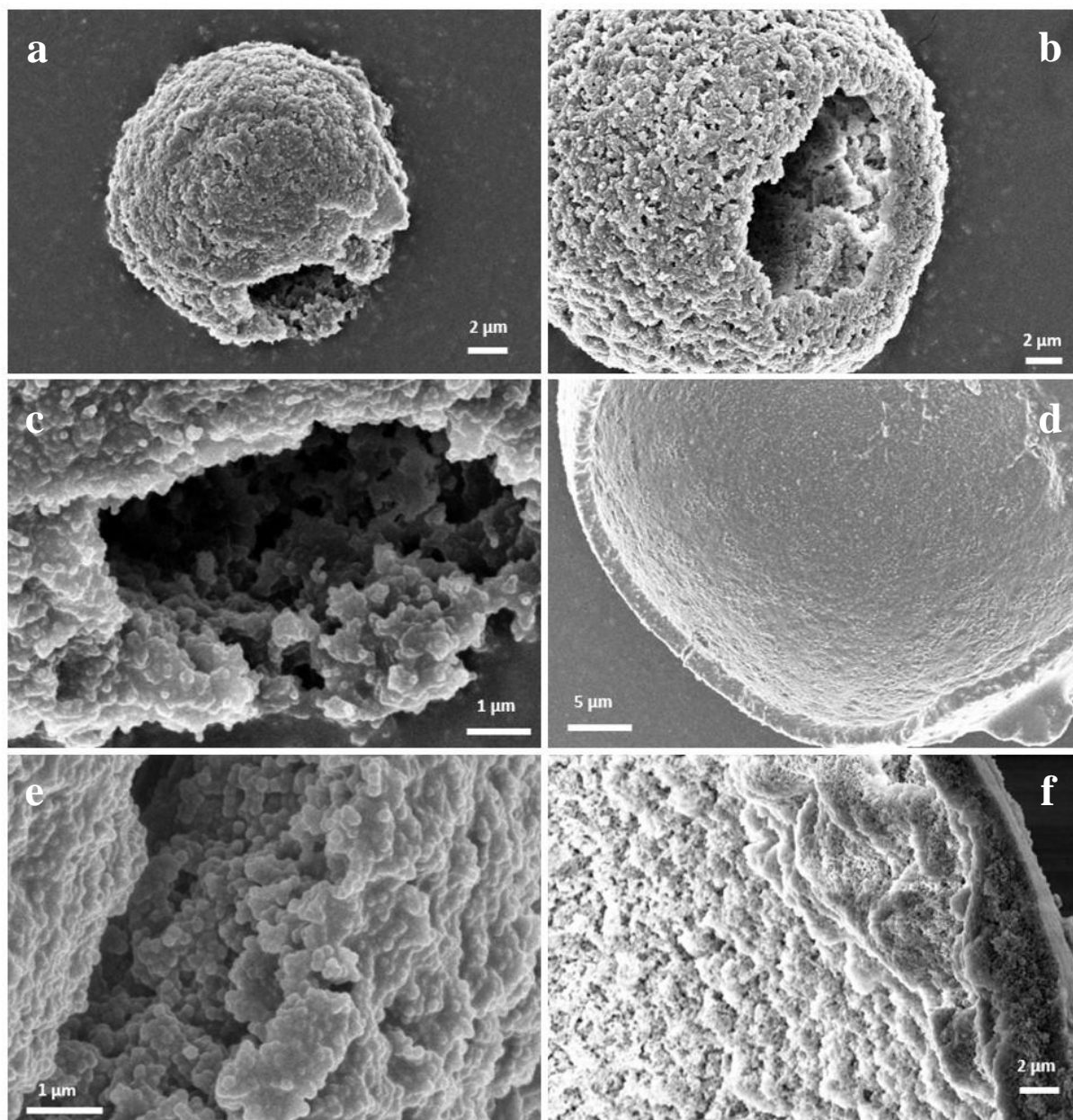


Figure 4.4. Pictures of the jammed arrangement of the NPs within the shell of the obtained hollow capsules.

The mechanism leading to the observed NP organization in Figure 4.4 is elusive in the literature and a full description is unavailable. A possible explanation might reside in some interactions among the NPs themselves and between the NPs and the fluorinated surfactant that stabilizes the latex-in-oil emulsion¹⁴⁵. This fluorinated surfactant possesses a hydrophilic part, the etheric domain¹⁴⁶ (*i.e.* polyethylene oxide), which is exposed toward the inside of the latex droplet, and at the actual pH 3 of the latex, the etheric oxygen atoms could be partially protonated. Moreover, the polymer NPs are stabilized via SDS, in concentration just below the critical micellar concentration (cmc), making them highly negatively charged. Then, an electrostatic attraction could be generated between the SDS-stabilized NPs and the protonated hydrophilic part of surfactant, which has been observed in the literature for the other systems^{147,148}. This pushes the NPs to move towards the interface of the droplet, to aggregate and jam, leading to the observed hollow and porous structure of the capsules. It is worth pointing out that this highlighted interactions might also not be the only effect occurring at the NP level. For example, it is well known that particles may self-arrange at the interface between two immiscible fluids, because of reduction in the free energy of the system, and this approach has been highly exploited to produce templated materials⁴⁷. On the other hand, this possibility is excluded in our case as we tried to work without the fluorinated surfactant and observed that the latex itself is unable to stabilize the water-in-oil emulsion. Moreover, the presence of surfactant in our case should prevent the possible interfacial jamming due to water migration within the oil domain and coffee-stain effect¹⁴⁹. This statement is also reinforced by the observed consistency between the size of the generated droplets and that of the final dry particles.

4.3.2 Computational Study of the Ether-SDS Interaction

According to literature data¹⁴⁷, the oxygen atoms of polyethers can be partially protonated at the pH value chosen for the present experiments. This can lead to an electrostatic-driven binding between polyether

groups and the polystyrene NPs, because the surface of the polystyrene NPs is negatively charged with the adsorbed SDS. In this framework, molecular dynamics (MD) simulations were employed in order to investigate the interactions between the NPs and the water-soluble chain of the surfactant. A detailed description of the simulation protocol is provided in Appendix C.

For this purpose, a simple model is here proposed. The system was modeled as a flat surface of amorphous syndiotactic polystyrene (Figure 4.5a), since the chain length of the water-soluble portion of the surfactant is much smaller than particle diameter. The surfactant is modeled as a polyethylene glycol (PEG) chain with 16 repeating units, which corresponds to a molecular weight of about 700 g mol^{-1} .

In order to reproduce experimental conditions, one side of polymer surface is almost fully covered by SDS (Figure 4.5b), by virtue of a surface density value equal to 1.7 mg m^{-2} , which is consistent with the experimental and computational studies presented in the literature^{150,151}. In addition, a complete coverage can be expected because of the large amount of the used SDS with respect to the polymer content.

In particular, two different conditions were here investigated, representative of low environmental pH (where all PEG oxygen atoms are protonated) and neutral/basic environmental pH (where PEG moieties are uncharged). These two cases should be intended as asymptotic behavior of the system, since in a more realistic case PEG chain is expected to be only partially protonated.

MD simulations were performed as follows. The SDS-covered surface was placed in the xy plane, in order to reproduce an infinite surface by means of periodic boundary conditions. One PEG chain was placed close to SDS layer and the surface was solvated with explicit water molecules along z direction. Explicit sodium ions were added in order to assure electroneutrality. Two different initial conditions were considered for each system (in terms of initial arrangement of PEG chain on the surface). 100 ns MD simulations were carried out for each model, in NPT ensemble at 300 K and 1 atm.

Notably, at neutral pH the unbinding between the uncharged PEG and the surface is observed during the simulation (Figure 4.5c), while the charged PEG chain is tightly bound to the adsorbed SDS (Figure

4.5d). In this case, the interaction energy was estimated by means of Molecular Mechanics Poisson Boltzmann Surface Area (MMPBSA) method, which highlighted the relevant contribution of electrostatic interactions in the binding. The obtained interaction energy value is equal to -181.71 ± 21.24 kcal mol⁻¹, where the contribution of Van der Waals interactions is limited to -3.39 ± 0.27 kcal mol⁻¹. The model results suggest that, amongst the other involved phenomena, the electrostatic-driven binding between polymer NPs and the water-soluble portion of the surfactant can indeed play a role in the system behavior.

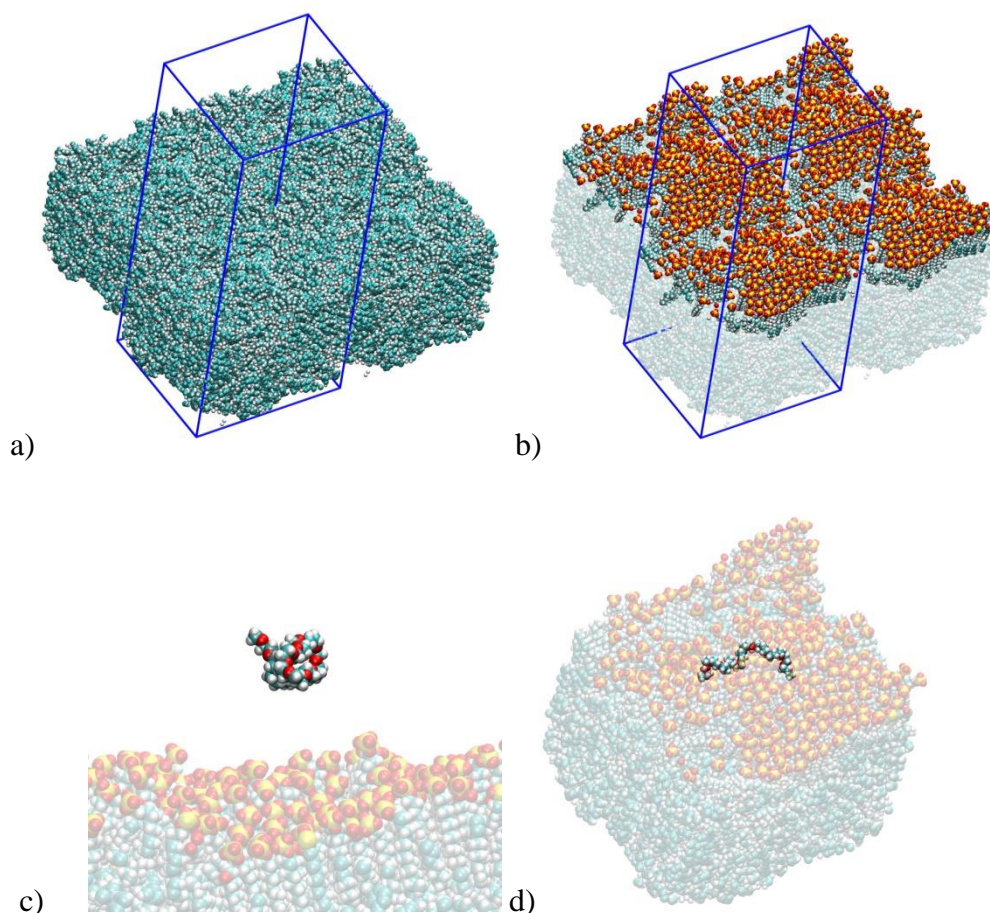


Figure 4.5. Basic element of PS surface, replicated along x and y direction; simulation box is highlighted in blue. Polystyrene is represented as VdW spheres, water and ions are omitted for the sake of clarity (a). Basic element of PS surface covered with SDS, replicated along x and y direction; simulation box is highlighted in blue. Polystyrene is represented as transparent VdW spheres SDS as VdW spheres, water and ions are omitted for the sake of clarity (b). Unbinding event of PEG chain from the SDS covered surface (c). Bound conformation of protonated PEG and SDS covered surface; protonated PEG is represented as VdW spheres (d).

4.3.3 Particles Features

Independently of the mechanism leading to the observed jamming of the primary NPs in the shell of the hollow capsules, we decided to investigate the effect of the initial NP concentration of the latex on the resulting structures. Indeed, it has been observed in macroscopic systems that the effect of the initial NP concentration on the final porosity is indeed substantial. In particular, the droplets have been produced from the latexes with the initial NP concentration of 6 wt%, 8 wt% and 12 wt%, respectively, and their

features have investigated. Figure 4.6 shows the pictures of the surface of the final capsules formed at different initial NP concentrations. As can be seen, increasing the primary NP concentration, the surface of the hollow capsules becomes more and more compact. In the case of 6 wt% in Figures 4.6a, 4.6d and 4.6g, the open pores are clearly observable, while in the case of 12 wt% in Figures 4.6c, 4.6f and 4.6i, they have almost disappeared. The situation in the case of 8 wt% in Figures 4.6b, 4.6e and 4.6h is just intermediate between the above two. Remarkably, not substantial difference was observed in the shell thickness, which was estimated in the range of 1 μm to 2 μm .

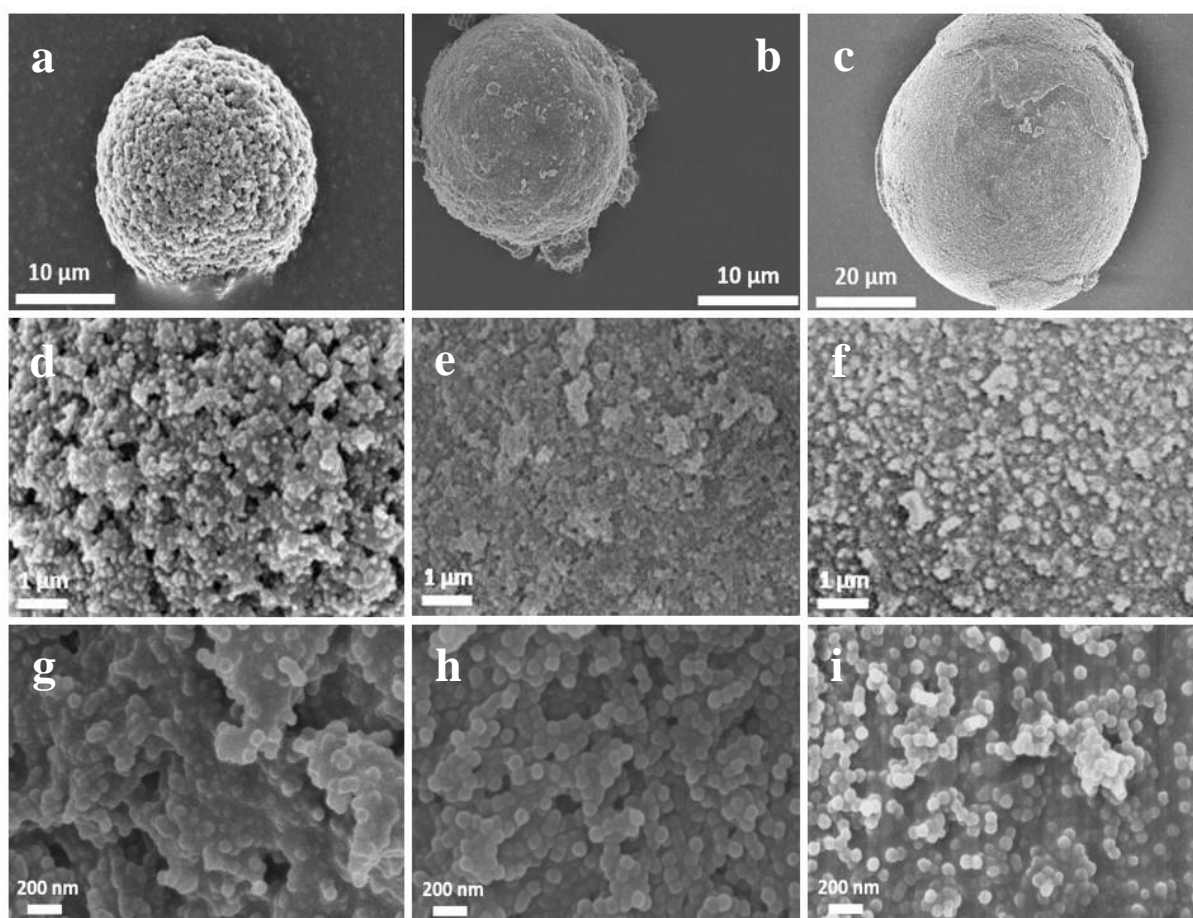


Figure 4.6. Pictures of the capsules and of their surface produced at different initial NP concentrations of the latex. Specifically: 6 wt% for a,d and g; 8 wt% for b, e and h; 12 wt% for c, f and i.

The above visually observed difference in the surface porosity has been further studied in respect to the actual influence it has on the accessibility of the capsules. Tracking rhodamine B intrusion into the

capsules produced at different initial NP concentrations revealed that the penetration of the dye into the capsules increases as the porosity of the surface increases, as clearly shown in Figure 4.7. In fact, at the highest NP concentration studied, 12 wt% in Figure 4.7c the dye is basically located only on the outer surface, because of the high compactness of the capsules, as can be seen in Figure 4.6i.

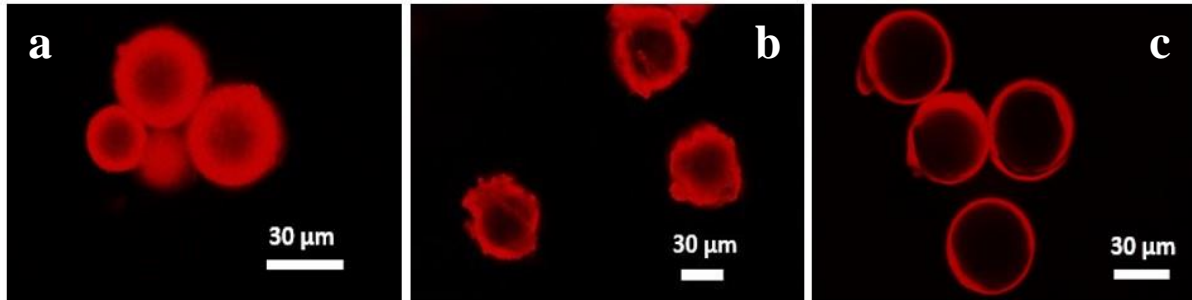


Figure 4.7. Pictures of the capsules produced at different initial NP concentrations but with similar sizes soaked into a rhodamine B solution after 24h. Specifically: 6 wt% for a, 8 wt% for b and 12 wt% for c

Figure 4.8 shows instead the results obtained by quantifying the actual concentration reduction of a fluorescently labelled species (FITC-dextran 4000) due to diffusion within the internal volume of the capsules. The data are reported in the form $\frac{C_0 - C_{eq}}{C_0 m_p}$, where C_0 represents the initial FITC-dextran 4000 concentration, C_{eq} the equilibrium one and m_p the actual dried mass of the porous capsules used. It can be noticed that a major specific decrease in the dye concentration in the solution at equilibrium is observable for the capsules that possess a higher surface porosity, thus resulting in higher accessibility to the selected species. Therefore, we can conclude that the primary NP arrangement within the jammed shell of the capsules, depending on the initial NP concentration of the latex, affects not only the surface appearance but also the permeability of the formed macroscopic hollow capsules. This statement has major implication in the future applications of these hollow capsules, for example in controlled release or trapping of valuable species.

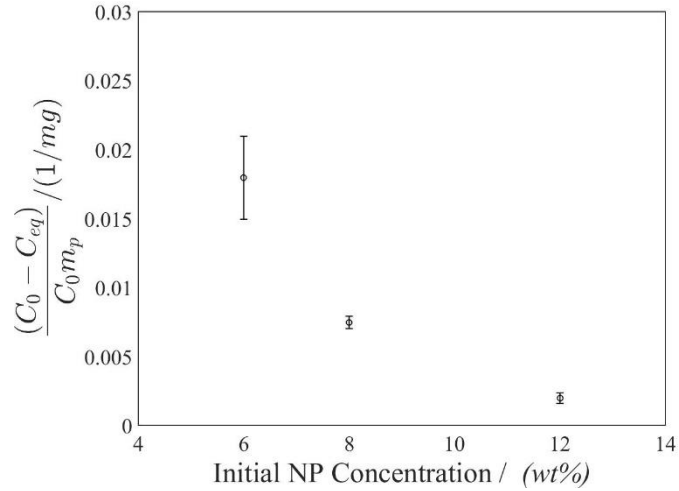


Figure 4.8. The actual concentration reduction (per unit mass of the added capsules) of FITC-dextran 4000 in the solution after adding the capsules for 24h as a function of the initial NP concentration of the latex used in the capsules production.

4.4 Conclusions

In this work we have presented a method to produce rigid hollow capsules combining reactive gelation and microfluidics. We started from the peculiar observation that latexes of polymer NPs housed in form of droplets at the microfluidic scale can form hollow spheres with a jammed solid-like shell, resulting in porous hollow capsules. A possible explanation of this phenomenon is discussed and supported by molecular dynamic simulations, which showed that a key role can be played by the electrostatic interactions between the negatively charged NP surface and the positively charged portion of the fluorinated surfactant under the acidic conditions, which was located inside the latex droplets, coming from the oil phase. As a matter of fact, it is possible to take advantages of this peculiar behavior as templating force for producing rigid, porous and permeable capsules. Owing to the aforementioned mechanism, which leads to the jamming of the NPs in a hollow arrangement, forming a porous shell, it is possible to tune the surface porosity by simply tuning the initial NP concentration of the latex. Indeed, compact surfaces of the capsules have been obtained, when using high NP concentrations (e.g. 12 wt%),

whereas at lower NP concentrations (e.g. 6 wt%) the surfaces are more open. Afterwards, thanks to the post-polymerization step of the reactive gelation, all of these structures can be consolidated, and rigid, hollow and permeable capsules are produced and collected as a powder after drying. The utilization of microfluidics introduces high versatility in the process, enabling the production of highly monodisperse capsules of different sizes. Moreover, using chips with different designs contributed to the understanding of the self-organization mechanism and to its control. As expected, different surface porosity results also in different permeability and accessibility for probe molecules. In this sense, we have shown both qualitatively and quantitatively that the intrusion within the internal volume of the capsules increases as the shell porosity of the capsules increases. As a conclusion, the combination of reactive gelation and microfluidics results in a robust and efficient method for production of rigid hollow capsules. Moreover, the ease of control of the capsule morphology and permeability might become a crucial point in the further applications such as trap and release of useful species in biomedicine, pharmaceuticals and material science.

Chapter 5

Tracking of Fluorescently Labeled Polymer Particles Reveals Surface Effects during Shear-controlled Aggregation

5.1 Introduction

The process of aggregation and breakage of polymer particles under shear, which is a very relevant operation in the production of many polymeric materials¹⁵², is highly influenced not only by the physical parameters of the system (*i.e.*, solid and volume fraction, shear regime, particles' size)^{153–157}, but also by the surface chemistry and properties of the particles themselves^{30,82,158,159}. Our ability to quantitatively describe the behavior of aggregating particles exposed to shear forces is only limited to simple systems, behaving strictly as non-deformable sticky spheres. As soon as the particles present complex surface features, such as advanced functionality and composition, core/shell architecture and presence of plasticizers that soften the particles' shells, they show characteristic and peculiar behaviors difficult to rationalize¹⁵⁸. A particularly relevant example is the one of surface nano-roughness, which has already been shown to strongly affect polymer particles' adhesion^{160,161}. Shear aggregation experiments carried out in our group on certain polystyrene particles have led us to hypothesize that, upon aggregation, their surface's roughness was changing as a function of time, leading to completely different time evolutions of clusters' morphology and to progressively decreasing average cluster sizes, instead of commonly

encountered steady-state conditions¹⁵⁹. Indeed, the increase in surface roughness leads to weaker bonds among particles within clusters, thus progressively increasing their breakage rate with time. Despite the importance of such effects, it is generally challenging to experimentally demonstrate not only the presence of surface roughness but even more a modification of this parameter upon prolonged exposure to shear forces. More importantly, the mechanisms that lead to these changes remain elusive. One of the proposed mechanism is plastic deformation, but what causes it still needs to be fully understood. Along with this line, molecular dynamic simulations have highlighted the possibility of some material transfer between particles as a result of repeated aggregation/breakage events, with small chunks of polymer being torn off from the surface, and transferred to other particles¹⁶².

In this work, we have devised a novel and elegant strategy to experimentally prove the deformation of polymer particles exposed to shear forces, causing their aggregation and subsequent breakage. The surface alteration mechanism of suitably engineered colloidal particles was revealed by means of fluorescent microscopy. This technique has the potential to accurately visualize colloidal clusters when they are made of large enough primary particles¹⁰⁴. Two sets of experiments were performed in this work. First, small polymer colloidal nano-particles with slightly crosslinked polystyrene shell, swollen with styrene, which acts as a softener, were exposed to shear-controlled aggregation under fully-destabilized conditions. It was found that the system did not reach a stable steady state size, as commonly observed with hard particles, but showed a decrease in the average cluster size over time while keeping a constant fractal dimension (*i.e.*, maintaining the cluster structure unaltered) and never reaching a steady state condition. Among the various factors hypothesized to explain this behavior, an alteration of the surface, due to the softness of the outer layer induced by the monomer, seemed the most plausible and consistent with our previous findings¹⁵⁹. In the second set of experiments, a different system was used, consisting of much larger particles, visible through an optical microscope, featuring a similar architecture to the smaller particles, but incorporating a fluorescent monomer. Using this second system, and working with

a mixture of fluorescently labelled and non-labelled particles, we took advantage of fluorescence to monitor the surface alteration of the particles. In particular, we tracked whether some polymer could be displaced from a particle to another upon repeated aggregation and breakage events by simply recording the percentage over time of particles showing fluorescence. It was demonstrated that substantial material exchange occurs between particles if their surface is sufficiently soft, which indeed is the case only in the presence of swelling monomer. Not surprisingly, the presence of a soft layer around the particles was also found to promote their adhesion upon contact¹⁶³. Keeping in mind that material exchange might not be the only mechanism responsible for surface alterations of polymer particles, this work proves for the first time that material exchange takes place, thus providing novel insight into the importance of particle architecture and surface properties on shear aggregation

5.2 Experimental

5.2.1 Materials

Divinylbenzene (DVB), styrene (STY), rhodamine B (Rh B), azobis(isobutyronitrile) (AIBN), sodium dodecyl sulfate (SDS), potassium peroxydisulfate (KPS), polyvinylpyrrolidone 40k MW (PVP), dicyclohexylcarbodiimide (DCC), 4-(dimethylamino)-pyridine (DMAP), 2-hydroxyethyl methacrylate (HEMA), magnesium chloride and acetonitrile were purchased from Sigma Aldrich and used without further purification. Ethanol was purchased from Fluka and used without further purification. Ultra-pure water was prepared by a Millipore Synergy water purification system. Nucleopore filters with 0.45 μm pore size for dialysis were purchased from Whatman.

5.2.2 Synthesis of Colloidal Core-Shell Polymer Nano-particles

The synthesis of the polymer nano-particles was carried out in a LabMax© Automatic Reactor from Mettler-Toledo equipped with a 4 L jacketed glass reactor. The preparation involved two steps: core synthesis and shell covering. The former was made of 20% cross-linked particles of styrene and divinylbenzene, produced *via* semi-batch emulsion polymerization, whereas the latter was obtained by a seeded emulsion polymerization, using the 20% cross-linked particles as a seed, forming a 1% cross-linked shell around the core.

Synthesis of the Core

A mixture of water and surfactant (SDS) was initially charged into a glass reactor and the temperature was set at 70 °C using the oil heating jacket (initial charge, IC as reported in Table 5.1). When the reactor temperature reached the set-point (in approximately 25 minutes), a solution of water and initiator (KPS) was injected through a septum directly into the reactor (initiator solution, IS). In order to guarantee starved conditions, an emulsion of styrene, DVB, water, and surfactant was fed over the reaction time using a syringe pump (continuous feed, CF as reported in Table 5.1). A solution of water and KPS was continuously fed using a second syringe pump, to guarantee the constant presence of the initiator (initiator feed, IF). When the reaction time was over, the system was kept at 70 °C for one hour, to ensure complete conversion of the monomer. The monomer conversion and the particle size evolution were followed by gravimetric analysis and dynamic light scattering (DLS), respectively. The exact quantities of the chemicals used in the particle synthesis are reported in Table 5.1.

Table 5.1. Recipe for the synthesis of the core. All numbers are target values, the actual ones may vary by less than 1%².

	IC	IS	CF	IF
Water	1575 g	75 g	315 g	75 g
DVB			63 g	
Styrene			252 g	
SDS	6.2 g		2 g	
KPS		2 g		2 g
Reaction time			5 hours	
Cross-linkage degree			20%	
Diameter			42 nm	
PDI			0.055	

Synthesis of the Shell

To form a soft shell onto the core particles, the latter was added a second time into the LabMax together with water and surfactant (initial charge, IC as reported in Table 5.2). The previously synthesized latex worked as a seed for the second polymerization step. When the reactor temperature reached the set point of 70 °C, a water solution of initiator KPS was added to the jacketed reactor (initiator solution, IS). During the reaction time, a mixture of styrene and DVB was fed to achieve a radially homogeneous

² IC = Initial Charge, IS = Initiator Solution, CF = Continuous Feed and IF = Initiator Feed.

cross-links density¹⁶⁴ (continuous feed, CF as reported in Table 5.2). Again, the monomer conversion and the average particle size were determined by gravimetric analysis and DLS, respectively. The complete recipe is reported in Table 5.2.

Table 5.2. Recipe for the synthesis of the shell. All numbers are target values, the actual ones may vary by less than 1%³.

	IC	IS	CF
Water	1295 g	50 g	
DVB			0.8 g
Styrene			79.7 g
SDS	1 g		
KPS		1.5 g	
Core latex	723 g		
Reaction time		5 hours	
Cross-linkage degree		1%	
Diameter		54 nm	
PDI		0.030	

³ IC = Initial Charge, IS = Initiator Solution and CF = Continuous Feed.

5.2.3 Synthesis and Purification of Rhodamine B - HEMA Precursor

The synthesis method was adapted from Cova *et al*¹⁶⁵. The rhodamine B-HEMA (RhB-HEMA) precursor was synthesized by Steglich esterification. In a flask, 4 g of RhB were dissolved in 80 mL acetonitrile. After full dissolution, 1.3 g of HEMA were added to the reaction mixture under stirring. In a second flask, 1.72 g of DCC and 52 mg of DMAP were mixed in 80 mL acetonitrile and added dropwise to the solution within 20 minutes. The reaction was run for 24 hours at 40 °C. The crude product was filtered to remove the precipitated by-product. The obtained solution was then purified by preparative chromatography using a C18 reversed phase column and Acetonitrile/Water mixture as the mobile phase. The purity of the product was confirmed by mass spectroscopy (LC-ESI-TOF) identifying a peak at 555 m/z. This precursor has been used to produce the fluorescent shell on the micron size particles.

5.2.4 Synthesis of Core-Shell Polymer Micro-particles

Synthesis of the Core

The synthesis method was based on the work by Lee *et al*.¹⁶⁶. Accordingly, 1.5 g of PVP were dissolved in 102.6 g of ethanol in a 500 mL round bottom flask and heated to 70 °C. Furthermore, 0.15 g AIBN were dissolved in 15 g styrene and added to the reaction mixture upon reaching the target temperature. The reaction was left at 70 °C for 24 hours under continuous stirring. When a conversion of 80% was reached, the mixture was cooled to room temperature. At this point, 1.43 g DVB, corresponding to 20% of the converted amount of styrene, were mixed with 0.075 g AIBN and added to 58 g of the seed reaction product. The mixture was left for 6 hours under stirring at room temperature. After completion, the mixture was added to a 250 mL three neck flask and heated to 70 °C for several hours, until conversion reached values above 95%. The final size was approximately 2 µm in diameter. SEM pictures and optical microscopy confirmed very high monodispersity of the prepared particles.

Synthesis of the Shell

In order to grow the shell on the polymer micro-particles, 50 g of the previously produced suspension of crosslinked core particles were added to a plastic wide neck bottle. Under stirring, 100 mL water were dripped into the solution over 20 minutes using an addition funnel. The resulting mixture was added to a Millipore dialysis chamber with a 0.45 micron Whatman Nucleopore membrane. Millipore water was rinsed through the chamber at 0.8 bar until the surface tension of the permeated solution reached the one of pure water, equal to 71.97 mN/m at 25 °C, to ensure complete removal of PVP from the dispersion. The dialyzed particles were transferred to a 250 mL round bottom flask and heated to 70 °C. After charging 0.01 g KPS, 30 μ L of the monomer mixture (styrene with 1% DVB) were added successively every 30 minutes over 4 hours to increase the particle size by about 100 nm. In case of the synthesis of a fluorescent shell, the RhB-HEMA precursor was added to the previous mixture. The precursor was dissolved in 5 mL acetonitrile and put into a small flask and completely dried from the solvent, using a rotary evaporator. The conventional monomer mixture used in the previous case was used to re-dissolve the precursor. Effective inclusion of the RhB-HEMA within the polymer was assessed by UV measurements of the supernatant after precipitation of the particles. The absence of any signal confirmed complete incorporation. Moreover, to verify with more accuracy that the dye is bound to the polymer chains, some particles were centrifuged out of the aqueous solution, dried, re-dispersed and swollen with an organic solvent (isopropanol). After precipitation of the polymer particles, the supernatant was newly analyzed by means of UV spectroscopy, and again no trace of dye was found. Increase in size of the particles was determined via small angle light scattering (SALS) measurements and SEM pictures. Moreover, the absence of an unwanted nucleation, leading to a second small nano-particles population was confirmed by DLS.

5.2.5 Processing of the Particles

Dilution and Swelling

The synthesized nano-particles' latex has been diluted with degassed Millipore water down to a specific dry mass fraction (5×10^{-5}). This mixture has either been used as it is or swollen with additional hydrophobic monomer (*i.e.*, styrene), whose amount is calculated as a percentage of the solid content of the latex. The obtained solution has been left under mild agitation overnight at 200 rpm before further processing.

The micro-particles dispersion has been diluted in degassed Millipore water from the previous mixture to reach a mass fraction of $5 \cdot 10^{-4}$. In case of swelling, pure styrene equal to half of the saturation concentration in water has been added to the mixture. The system was left to equilibrate overnight. The repartition of the monomer between the water and the hydrophobic polymer phase allows for swelling of the outer, slightly crosslinked shell on the surface of the particles. Experiments were run using either fully non-fluorescent or an equal mixture of fluorescent and non-fluorescent particles.

Stirred Tank Reactor

The diluted latex has been aggregated using a 2 L cylindrical stirred tank reactor equipped with a 60 mm Rushton impeller and four metallic cylindrical baffles. The solution has been fed into the reactor through an opening and the tank has been firmly closed. Significant attention has been dedicated to the removal of any bubble of air inside the reactor, to avoid aggregation at the interface between the suspension and air. To prevent air entering the reactor when sampling, part of the excess polymer solution was pumped in a vertical tube (1.5 m high) connected to the reactor. The stirring velocity is set at 500 rpm, which corresponds to a maximum shear rate of 17300 s^{-1} and an average one in the range of $900\text{-}1700 \text{ s}^{-1}$, evaluated from the scaling for the maximum dissipation rate proposed by Soos *et al*¹⁶⁷. In order to destabilize the system, 60 mL of a 2 M solution of MgCl_2 were added to the reactor through an opening in the bottom plate. Owing to the strong shear forces produced by the stirrer, the primary particles start

aggregating in a shear-controlled regime, which is not driven by Brownian motion but is controlled by the extent of the applied shear.

5.2.6 Characterization Methods

Monomer Conversion

The monomer conversion is determined from the dry mass fraction of the sample. A small aliquot of the sample (about 1cc) was spread over quartz sand and heated at 120 °C in air using a HG53 Moisture Analyzer from Mettler-Toledo.

Dynamic Light Scattering

The average size of the nano-particles was determined by dynamic light scattering (DLS) using a Zetasizer Nano ZS from Malvern.

Static Light Scattering

To compute the size and the fractal dimension of the aggregated nano-particles' clusters, the average size of the micro-particles as well as of their aggregated clusters, small angle static light scattering Mastersizer 2000 from Malvern Instruments equipped with a laser having $\lambda_{SALS} = 633$ nm was used. The radius of gyration $\langle R_g(t) \rangle$ was obtained by fitting the structure factor in a Guinier plot, as reported in Harshe *et al*²⁸. The fractal dimension d_f was extracted from the Guinier plot, by measuring the slope of the curve in the power-law region, using the relation $\langle S(q) \rangle \propto q^{-d_f}$.

Microscopy

The micro-particles and their clusters were analyzed using scanning electron microscopy (Gemini 1530 FEG from Zeiss), with field emission gun operated at 5 kV. The coating of the samples was performed using platinum. Optical microscopy was performed using a Leica SP8-AOBS confocal microscopy. An Argon laser at 550 nm was used for excitation of the samples and the emitted light was collected using one HyD detector. Bright field images were collected in parallel using a PMT detector.

Image Analysis

The image analysis was performed on the picture taken with confocal microscopy using ImageJ software. At least 2000 micro-particles were evaluated for each measurement. For each picture, the average area in terms of number of pixels occupied by the non-clustered polymer micro-particles was evaluated. The obtained value was used, together with the total occupied area, to compute the total number of polymer micro-particles present as individuals, non-clusters objects as well as aggregated in clusters, both in the case of not-fluorescent and fluorescent particles.

5.3. Results and Discussion

5.3.1 Shear-controlled Aggregation

In our shear-controlled aggregation experiments, a colloidal suspension of primary particles is fed into a stirred tank reactor and an electrolyte solution is added to fully destabilize the system. However, owing to the presence of the stirrer, the aggregation process is not driven by Brownian motion but is controlled by the magnitude of the applied shear. Accordingly, the aggregation rate is highly affected by the stirring velocity¹⁵⁶. The destabilization of the system due to the electrolyte addition cancels the repulsive energy barrier, thus leading to primary particles aggregating at a much faster rate into their primary energy minimum. The stirrer creates velocity gradients that drive particles and clusters against each other, thus increasing the frequency of their encounters. On the other hand, clusters may also break under the action of hydrodynamic stresses caused by the presence of shear forces¹⁵⁶. Consequently, it is expected that the system reaches and preserves a steady state condition, determined by an equilibrium between the aggregation and breakage rates¹⁵⁷. The critical parameter defining the region of shear-controlled

aggregation is the Peclet number (Pe) which expresses the ratio between the shear and the Brownian forces and is defined according to the equation:

$$Pe = \frac{3\pi\mu\dot{\gamma}R_p^3}{k_B T} \quad (1)$$

where μ is the solvent viscosity; $\dot{\gamma}$ is the shear rate; R_p is the radius of the primary particles; k_B is the Boltzmann's constant; T is the absolute temperature³⁰.

5.3.2 Aggregation of Nano-particles

The study of the aggregation of particles in a shear-controlled regime has been carried out using the polymer nano-particles with a core-shell structure, synthesized through the recipe described in the experimental section. The soft shell of the polymer particles allows for swelling by additional monomer (styrene), which is used as a plasticizer that lowers the glass transition temperature of the polymer domain¹²³, thus making it very soft at the operating temperature. The addition of highly concentrated (2 M) magnesium chloride solution ensures full screening of the surface charges located at the particles' surface. The system is left under agitation for some hours and the morphology evolution of the clusters, in terms of the radius of gyration ($\langle R_g \rangle$) and fractal dimension (d_f) is monitored. As the latter is obtained *via* power-law regression of the scattering structure factor, only variations in the range of ± 0.1 are appreciable. Figure 5.1 reports the average cluster size and fractal dimension as a function of the aggregation time for the samples swollen with 0, 10 and 20% of additional monomer.

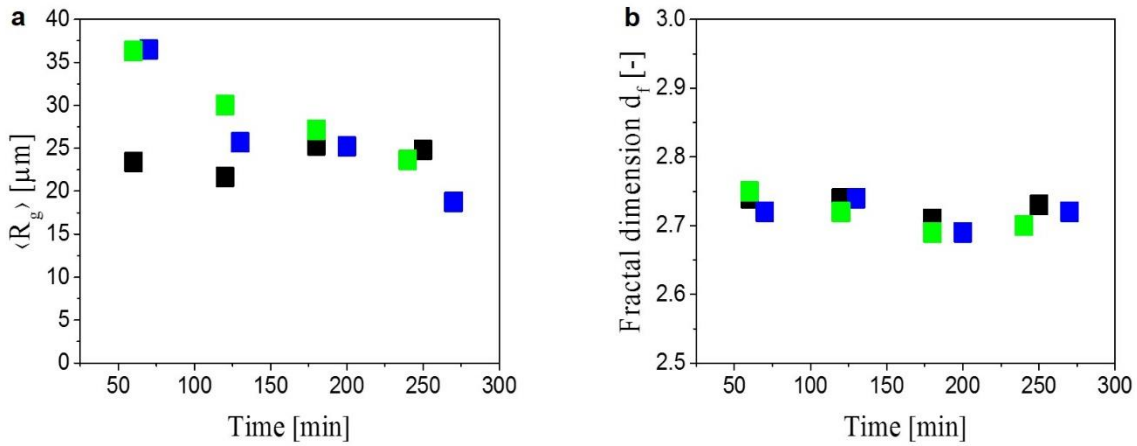


Figure 5.1. Time evolution of the average cluster size (a) and fractal dimension (b) for different swelling ratios (black squares: non-swollen; blue: 10% swollen; green: 20% swollen) during the shear-controlled aggregation of nano-particles.

As it can be seen from Figure 5.1a, the average cluster size for the not swollen clusters presents no appreciable variations with time after about 50 minutes and reaches a constant value of approximately 25 μm (black squares). This is in agreement with the results obtained by Harshe *et al*²⁸ and Soos *et al*¹⁵⁶ and shows that the interplay between aggregation and breakage reaches an equilibrium and the average cluster size remains steady in time. Due to the high Pe number, as soon as a cluster is broken into smaller fragments, it promptly aggregates with other polymer particles or clusters to reach the same constant average size. On the other hand, in the case of primary particles swollen with 10 and 20% of styrene, the average size of the clusters continuously decreases with time. In particular, the average size of the sample swollen with 10% of styrene is measured to vary from 36 μm after 70 minutes to 19 μm after 270 (blue squares). Likewise, the size of the sample swollen with 20% of additional monomer decreases from 36 μm after 60 minutes to 23 μm after 240 (green squares). In addition, Figure 5.1b shows that the fractal dimension remains constant at a value of approximately 2.7, which is virtually identical to that obtained for clusters made of non-swollen particles in the case of shear-induced aggregation and breakage processes²⁸.

The observed decrease of the aggregate size with time is in contrast with the available literature and accepted explanations for this trend are still missing. Consistently with what hypothesized in a previous work¹⁵⁹, the observed trend could be the result of some alterations on the surface of the swollen primary particles, which eventually affect the bond strength among particles and consequently the rate of breakage. More specifically, after the particles undergo many cycles of aggregation and breakage, their surface could become more irregular and less homogeneous. The experimental evidence indicates that this process should be related to the morphology of the primary particles, which are made of a hard core surrounded by a shell that is softened through monomer swelling. One possible mechanism consistent with these observations is that the surface alteration of the primary particles occurs through material exchange among different particles upon collision and breakage. These alterations may affect the surface adhesion of the particles and consequently the breakage rate because less energy is required in order to separate them. It is worth noting that the observed behavior cannot be simply due to the fact that the system is not yet at equilibrium conditions, because a destabilized system under shear-controlled aggregation regime typically reaches equilibrium between aggregation and breakage within about 60 minutes, at least for the particle concentration used in these experiments¹⁵⁶.

5.3.3 Aggregation of Micro-particles

In order to confirm whether the hypothesized material exchange process occurs, aggregation and breakage have been investigated using micro-particles produced according to the recipe reported in the experimental section. These particles exhibit the same architecture as the nano-particles: they have a hard core of 2 μm diameter, composed of polystyrene crosslinked with 20% DVB, and a soft outer shell of 100 nm, again made of polystyrene but only 1% crosslinked. The morphology of the micro-particles before and after the growth of the shell is shown in Figure 5.2. Note that the micro-particles present

dimples, which probably result from the swelling and crosslinking procedure used to produce their shell, as reported and discussed earlier in the literature^{168,169}.

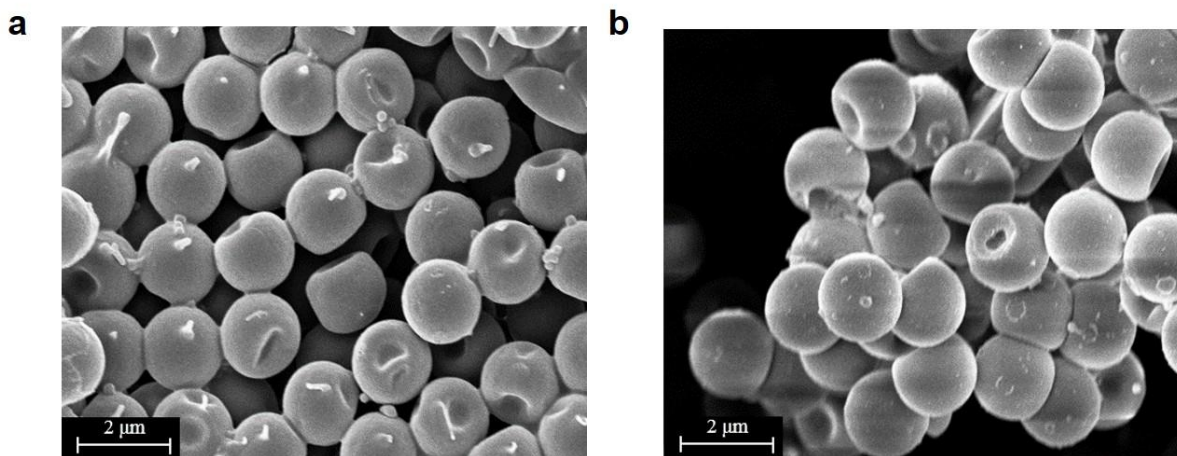


Figure 5.2. Particles without shell (a) and after shell growth (b).

Furthermore, some particles have been made fluorescent by the addition of RhB-HEMA precursor in the monomer mixtures used to synthesize the shell, so that they can be visualized with a fluorescent confocal microscope. Their shear-controlled aggregation has been investigated by introducing an equal mixture of fluorescent and not fluorescent particles into the stirred tank, following the same procedure as for the nano-particles. Again, the experiments have been run without and with the addition of further styrene in order to swell, and thus soften, the particles outer shell. The number of fluorescent micro-particles before and after aggregation, present both as single entities as well as grouped in clusters, has been determined by image analysis. Figure 5.3 shows the confocal pictures of the micro-particles, before and after applying the fluorescent filter. This allows visualizing all the particles (Figure 5.3a) or only the fluorescent ones (Figure 5.3b). The two pictures are superimposed in Figure 5.3c, which allows appreciating how many micro-particles result fluorescent.

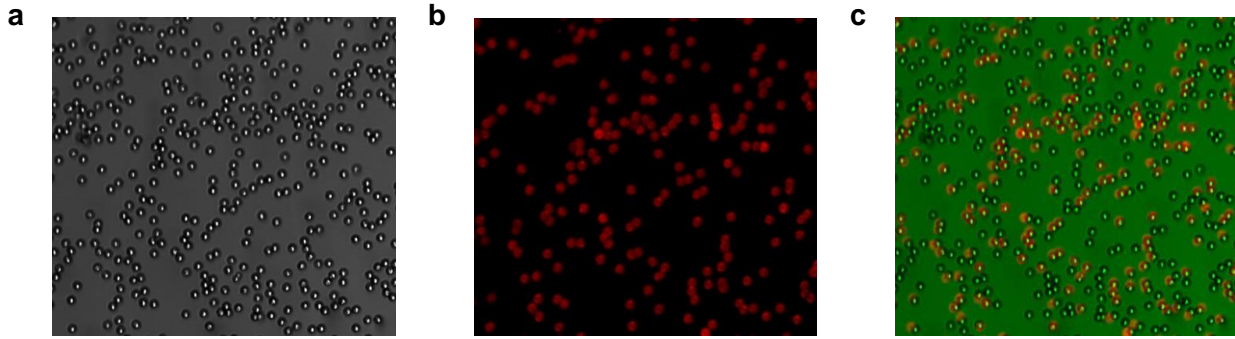


Figure 5.3. Micrographs of the micro-particles in transmission mode (a), in fluorescent confocal mode (b) and their superposition (c).

Aggregation of non-swollen Micro-particles

Non-swollen micro-particles were aggregated under shear and monitored for several hours. The $\langle R_g \rangle$ values of the formed clusters measured by small angle light scattering measurements are shown in Figure 5.4 (red squares). It can be observed that already after one hour a steady state of the average size is reached, which remains constant over the five hours' experimental time. Remarkably, this equilibrium value for $\langle R_g \rangle$ is considerably smaller than in the case of nano-particles. This observation can be understood considering the number of particles present in each cluster, which can be estimated through the equation:

$$i = k \left(\frac{\langle R_g \rangle}{R_p} \right)^{d_f} \quad (2)$$

where k is the fractal prefactor, a number whose value typically ranges between 1 and 1.2^{170,171}; $\langle R_g \rangle$ is the average radius of gyration; R_p is the radius of the primary particles; d_f is the fractal dimension of the colloidal aggregates. It results that the number of nano-particles aggregated in a cluster is in the order of 10^7 , whereas the one of the micro-particles is limited to 4-5. Since aggregation is a second order kinetic process, a smaller number of particles implies a lower aggregation rate, while breakage, being a first

order kinetic process, is unaffected by a lower number of particles. It is, therefore, reasonable to expect a different equilibrium condition, dominated by the relative higher breakage contribution. Moreover, the breakage process is also strongly influenced by the size of the particles. For the same cluster size, in fact, a cluster made of micron-sized particles contains a lower number of particles and consequently a lower number of bonds among them. Given this relatively weaker bond strength compared to the hydrodynamic stress acting on the particles, it is reasonable to assume that, when subjected to shear, their clusters can re-break into much smaller units, including individual particles¹⁷². In order to determine any alteration on their surface, the percentage of fluorescent particles was monitored as a function of time as shown in Figure 5.5 (red squares). The fact that this value does not change over five hours allows concluding that, in this case, no material exchange occurs among the surfaces of the primary particles.

Aggregation of Swollen Micro-particles

The same experiment has been repeated using particles whose shell has been swollen with styrene. The values of $\langle R_g \rangle$ were determined *via* light scattering and shown in Figure 5.4 as a function of time (green squares). It is seen that the gyration radius reaches the value of 3 μm within the first hour and then remains constant. Noticeably, it seems not to decrease over time, as in the case of the nano-particles. This aspect is again due to the low number of particles present in each cluster, which makes it difficult to observe a significant decrease in the average cluster size in time when dealing with micro-particles. In any case, it is a fact that the interplay between aggregation and breakage controls the process. Anew, the proportion of fluorescent particles was measured. As visible in Figure 5.5, the percentage of fluorescent particles clearly increases over time, moving from the initial 50% to approximately 62% after two hours and eventually to 70% after five hours (green squares). This experiment shows that the fluorescent polymer chains, initially present only on the surface of fluorescent particles, are displaced and can be found also on the surface of non-fluorescent particles. In particular, this material exchange occurs only when the shell of the particles is sufficiently soft, *i.e.*, when the particles are swollen by styrene. It is therefore

reasonable that a similar mechanism occurs even in the case of nanoparticles, and might be responsible for the unexpected progressive decrease in the average cluster size.

Aggregation of the Micro-particles without Shell

For sake of completeness, the highly crosslinked polystyrene micro-particles without shell were aggregated under shear. Interestingly, under the same conditions, they were unable to aggregate over the four hours' time course of the experiment (Figure 5.4). This behavior further confirms the extreme importance of the surface of the particles in colloidal aggregation. More aptly, a softer surface, in this case due to a 1% crosslinked polystyrene shell of 100 nm, was observed to promote aggregation, whereas a harder one, composed of highly crosslinked polystyrene (20%), makes it impossible for the micro-particles to form stable clusters in the tested conditions. They surely collide but due to their rigidity, weak bonds are formed, which are easily broken by shear forces.

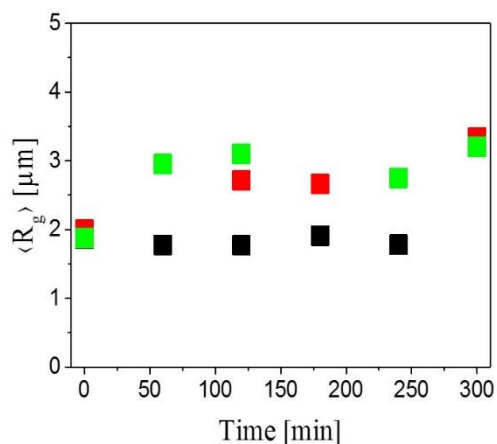


Figure 5.4. Average $\langle R_g \rangle$ as a function of time for different micro-particles. In particular: black squares refer to non-swollen core micro-particles, red squares to non-swollen core-shell micro-particles and green squares to swollen core-shell micro-particles.

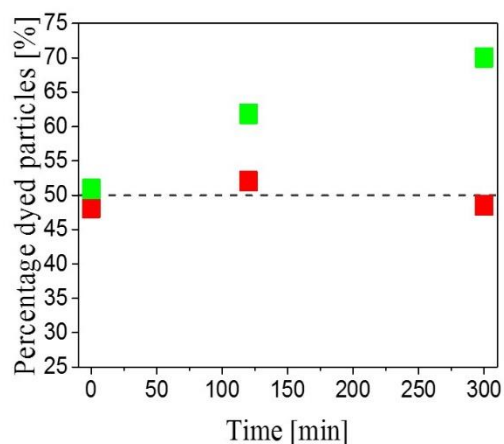


Figure 5.5. Percentage of fluorescent core-shell micro-particles as a function of time (red squares: non-swollen, green squares: swollen).

5.4. Conclusion

In this work, shear-induced aggregation experiments of various polymer colloidal particles have been carried out, with the specific objective of clarifying the role of the softness of the particle shell on the outcome of the aggregation. In particular, in a previous work, we hypothesized that the surface of sufficiently soft particles could be deformed as a result of the repeated aggregation and breakage events, leading to an increase in surface roughness. This effect could be sufficiently pronounced to lead to exchange of material from one particle surface to another. In order to prove the presence of such material exchange, specially designed polymer particles with core-shell structure, and having fluorescence group incorporated into their shell have been prepared. To tune the softness of the polymer shell, some styrene monomer was added, which acts as a plasticizer. For the first time, material exchange occurring on the surface of core-shell polymer micro-particles, when softened by monomer addition, upon aggregation under shear was proven and highlighted. This was achieved by aggregating a 1:1 mixture of fluorescent and non-fluorescent particles, and by monitoring the increase in the number of particles exhibiting fluorescence as a function of time. An increase in the percentage of particles showing a fluorescent signature was recorded over time, reaching after 5 hours a fraction of 70%.

The consequences of our work are far-reaching. It is reasonable to assume this phenomenon to be responsible for the unusual behavior observed on similar nano-particles in the same conditions (swollen shell). Indeed, the slow but progressive decrease in the size of the formed clusters over time upon shear-controlled aggregation, without substantial change in fractal dimension, and without reaching steady-state conditions, might be due to surface alterations and increased roughness on the polymer domain induced by material transfer. These modifications can affect the surface adhesion among the particles and lead to a restructuring of the clusters towards continuously new steady-state conditions between aggregation and breakage.

It is worth noticing that material exchange, which has been proven for the first time in this work, might not be the only phenomenon controlling the unusual behavior observed in shear-controlled aggregation of nano-particles, but we believe that it represents a very important effect, the full consequences of it need to be further ascertained and deepened.

Chapter 6

Conclusions

In this thesis primary polymer nanoparticles with different features have been used as building blocks to produce porous functional materials via Reactive Gelation in various forms (monoliths, clusters and capsules) depending upon on the operative aggregation regime. An accurate control of the characteristics of the aforementioned particles enabled to access products with different mechanical properties and internal microscopic porous structure. More specifically, major emphasis has been posed on the concept of particle architecture (described in terms of core-to-particle ratio), namely the differentiation in the particle composition between a hard crosslinked core and a soft superficial shell. This morphology allows different degree of interpenetration upon particle aggregation as a function of the shell thickness. Moreover, it affects also the surface properties of the particles, elucidating peculiar behaviors in clusters evolution during aggregation under shear.

Control of Pore Structure in Polymeric Monoliths Prepared from Colloidal Dispersions

Polymeric monoliths are produced when stagnant aggregation is performed. In this sense, primary nanoparticle architecture, size and initial concentration have the major impact on the mechanical stability and morphology. Regarding the first parameter, it was revealed that the presence of a thick shell around the particles is crucial in determining the pore morphology of the material: specifically, monoliths characterized by a bimodal pore size distribution and higher porosity have been formed from particles

with lower core-to-particle ratio of 0.73, whereas a monomodal pore size distribution and lower porosity have been obtained at a higher core-to-particle ratio of 0.82. Further increase in the core-to-particle ratio resulted in the formation of unstable structures due to very weak particle interconnections. Besides, increasing the shell thickness leads to smaller surface areas. The same conclusions have been drawn when using particles of different initial size, thus showing that the effect of architecture is independent on the scale. About the solid content, provided that the right architecture is chosen, highly porous monoliths can be produced by properly decreasing the initial dry solid content.

Preparation of Ultra-Perfusible Chromatographic Materials via Shear-Induced Reactive Gelation

Another method to produce porous materials is represented by shear-induced aggregation, in which polymer nanoparticles are assembled into fractal-like clusters by exposing them to high shear rates generated in a microchannel. After post-polymerization these clusters have been packed in conventional chromatographic columns and tested as stationary phase. Once again the effect of the primary particles characteristics has been investigated and their features tuned in order to achieve very rigid clusters with huge pores, able to withstand high flow rates after packing and exhibiting small pressure drops. Such a peculiar performance has been obtained when primary nanoparticles presenting a thick shell have been implied, rather independently on their initial size. Moreover, the presence of extremely large pore sizes, up to several micrometers, makes the contribution of convective flow through the clusters dominating the mass transfer. This way, a flat HETP profile, independent of fluid velocity, has been observed when the column has been tested with tracers in size range of most common bio-macromolecules. Due to their very peculiar flow characteristics and similarity to those of monolithic supports, these novel materials have been named Ultra-Perfusible. As a matter of fact, they represent an extremely promising and efficient easy-to-pack base scaffolds suitable for further functionalization.

Synthesis of Monodisperse, Porous, Rigid, Hollow and Spherical Polymeric Capsules Combining Microfluidics and Reactive Gelation

Microfluidics represents a valuable tool for closely studying peculiar behavior of colloidal polymer particles in different conditions. In this sense, it was observed that micro-droplets of polymer latex dispersed in oil can be used as template for producing permeable capsules, as the nanoparticles self-organize in a hollow-like jammed structure. Indeed, thanks to the post-polymerization step of Reactive Gelation, the aforementioned arrangement could be consolidated and rigid hollow capsules produced and collected as a powder. The jammed self-arrangement of the nanoparticles, forming a porous crust, allowed to tune the superficial porosity by simply varying the initial nanoparticles concentration. As a matter of fact, very compact surfaces have been obtained when an initial concentration of 12 wt% was chosen, whereas quite loose and porous facets have been recorded starting instead with 6 wt%. Moreover, test performed with fluorescent species, showed that this last parameter directly reflects into the permeability and accessibility of the capsule for probe molecules.

Tracking of Fluorescently Labeled Polymer Particles Reveals Surface Effects during Shear-Controlled Aggregation

The aggregation behavior of colloidal particles exposed to shear forces is quite difficult to rationalize as soon as we move from conventional hard and non-deformable sticky spheres towards complex features. Starting from the observation that soft core/shell swollen particles do not reach a dynamic equilibrium between aggregation and breakage, differently from common records in literature, ad hoc experiments have been performed in order to check whether the particles' surface might modify, upon repeated collision and breakage events. An equal mixture of fluorescent and non-fluorescent particles, whose surface was softened by monomer swelling, was aggregated and the number of particles exhibiting fluorescence as a function of time monitored. The final outcome was an increase in the percentage of particles showing a fluorescent signature, rising over time and reaching a fraction of 70% after 5 hours.

As a matter of fact, it was proved that material transfer occurs among individual particles when the surface is sufficiently soft. These modifications can affect the surface adhesion among them and lead to a restructuring of the clusters towards new steady-state, thus altering the final equilibrium. Material transfer may not be the only superficial effect occurring during aggregation/breakage under shear, but it correctly explains the aforementioned peculiar behavior.

Outlook of this Thesis

The results presented in this thesis, support the statement that Reactive Gelation represents a valuable tool for the production of porous materials in different forms. Moreover, the possibility of differentiating their final morphological characteristics through the features of the primary particle, and more specifically their architecture, provides outcomes ready for a really wide range of possible applications.

In view of this consideration, the major remaining open issues are essentially two, one more practical and the other more fundamental.

From the practical point of view, the presented porous materials represent already a valuable solution if implied as adsorbents or thermal insulators. However, in order to better fulfill more advance applications, further functionalization might be required. In this sense, it might be useful to directly incorporating functional groups on the surface either during the primary polymer particles synthesis or in a subsequent step. For this second case, different strategies can be used. Among them, the use of polymer brushes directly grown or just “clicked” on the surface represents maybe the most practical and versatile. This way, the same starting material can act as a base scaffold to be further tailored towards any specific requirements and still presenting the major features of the pristine structure, such as mechanical resistance or convective flow behavior. In this very last case, for example, the impact on the development of products for the purification of biopharmaceutical will be dramatic, considering the continuously increasing request of high performance materials.

From a fundamental point of view, certainly it would be of great interest to deepen the knowledge on the aggregation and self-organization behavior of even more advanced particles, introducing shape irregularities, exterior roughness, dimples or patchy surfaces. The response to different external stimuli of this secondary generation of particles is all but trivial and full understanding still missing. The development of this fundamental knowledge will enhance even more the colloidal approach towards advanced, functional and nano or micro-structured materials.

Appendices

Appendix A - Chapter 2

Latex Synthesis

Core

A mixture of water and surfactant (SDS) was initially charged into the glass reactor and the temperature set to 70°C (Initial Charge, IC). Once this set-point was reached, a solution of water and initiator (KPS) was injected (Initiator Shot 1, IS1). In order to guarantee starved polymerization conditions, an emulsion of styrene, DVB, water, and surfactant was fed over the reaction time using an HPLC pump (Charged Feed 1, CF1). Moreover, a solution of water and KPS was continuously fed as well, as the total reaction time is longer than the half-life time of the initiator at the reaction temperature (Initiator Feed, IF). The reacting mixture was constantly monitored and specifically conversion checked to ensure that the system is kept in starved condition.

Shell

The previously synthesized latex acts as a seed for the growth of a soft shell around the hard core particles. A new monomer solution (Charged Feed 2, CF2), this time composed only of styrene and DVB, was then fed to the system in a continuous way (i.e., without lag time or stopping the previous reaction of core synthesis), in order to achieve a radially homogeneous shell growth. The previous initiator feed was disconnected, while a shot of water and KPS was added to the reaction to keep it proceeding (Initiator Shot 2, IS2). Also during this stage, the reacting mixture was constantly monitored in terms of conversion to ensure starved condition. After the new monomer addition was complete, the synthesis was stopped once full conversion and the desired particle size were obtained.

Latex Characterization

During its production, the latex was continuously monitored in terms of particles size distribution, determined by dynamic light scattering (DLS) using a Zetasizer Nano ZS from Malvern and monomers

conversion, determined from the dry mass fraction of the sample. The latter was spread over quartz sand and analyzed at 120°C in air using a HG53 Moisture Analyzer from Mettler-Toledo.

Table A.1. Recipes used for the synthesis of latexes L1, L2 and L3.

Latex L1						
	Core				Shell	
	IC	IS1	CF1	IF	CF2	IS2
H2O (g)	250	25	29.1	74		20
Styrene (g)			23.3		35.64	
DVB (g)			5.8		0.324	
SDS (g)	0.375		0.58			
KPS (g)		0.75		1.24		0.2
% crosslinker	20				1	
Diameter (nm)	80				107	
PDI	0.03				0.002	

Latex L2						
	Core				Shell	
	IC	IS1	CF1	IF	CF2	IS2
H2O (g)	250	25	36	50		45
Styrene (g)			28.5		23.76	
DVB (g)			7.1		0.24	
SDS (g)	0.375		0.39			
KPS (g)		0.75		1.25		0.75
% crosslinker	20				1	
Diameter (nm)	89				113	
PDI	0.03				0.01	

Latex L3						
	Core				Shell	
	IC	IS1	CF1	IF	CF2	IS2
H2O (g)	250	25	37.5	95.6		20
Styrene (g)			30		11.88	
DVB (g)			7.5		0.12	
SDS (g)	0.375		0.75			
KPS (g)		0.75		1.6		0.2
% crosslinker	20				1	
Diameter (nm)	98				111	
PDI	0.09				0.04	

Table A.2. Sequence of addition of the different feeds for latexes L1, L2 and L3.

Latex L1																					
Core														Shell							
1h	2h	3h	4h	5h	6h	7h	8h	9h	10h	11h	12h	13h	14h	15h	16h	17h	18h	19h	20h		
IC																					
IS1																					
CF1																					
IF1																					
														IS2							
														CF2							

Latex L2																			
Core																Shell			
1h	2h	3h	4h	5h	6h	7h	8h	9h	10h	11h	12h	13h	14h	15h	16h	17h	18h	19h	20h
IC																			
IS1																			
CF1																			
IF1																			
																IS2			
																CF2			

Latex L3																			
Core																	Shell		
1h	2h	3h	4h	5h	6h	7h	8h	9h	10h	11h	12h	13h	14h	15h	16h	17h	18h	19h	20h
IC																			
IS1																			
CF1																			
IF1																			
																	IS2		
																	CF2		

Table A.3. Recipes used for the synthesis of latexes L4 and L5.

Latex L4						
	Core				Shell	
	IC	IS1	CF1	IF	CF2	IS2
H2O (g)	1024	48	103	12.2		25
Styrene (g)			82		95.4	
DVB (g)			20.5		0.96	
SDS (g)	3.24		0.6			
KPS (g)		1.3		0.65		0.75
% crosslinker	20				1	
Diameter (nm)	41				56	
PDI	0.06				0.04	

Latex L5						
	Core				Shell	
	IC	IS1	CF1	IF	CF2	IS2
H2O (g)	900	12.19	42.7	6.1		25
Styrene (g)			34		39.85	
DVB (g)			8.5		0.4	
SDS (g)	3.52		0.24			
KPS (g)		0.325		0.325		0.75
% crosslinker	20				1	
Diameter (nm)	40				49	
PDI	0.07				0.07	

Table A.4. Sequence of addition of the different feeds for latexes L4 and L5.

Latex L4							
Core			Shell				
1h	2h	3h	4h	5h	6h	7h	8h
IC							
IS1							
CF1							
IF1							
					IS2		
					CF2		

Latex L5									
Core					Shell				
1h	2h	3h	4h	5h	6h	7h	8h	9h	10h
IC									
IS1									
CF1									
IF1									
					IS2				
					CF2				

Table A.5. Recipes for the monolith production.

Sample	Latex	Initial Solid Content [%]	Volume [ml]	Volume NaCl [ml]	NaCl Concentration [M]	Percolating Volume [ml]
M1	L1	8%	1	1	0.5	2
M2	L2	8%	1	1	0.4	2
M3	L3	8%	1	1	0.5	2
M4	L4	8%	1	1	0.3	2
M5	L5	8%	1	1	0.3	2
M7	L1	4%	1	1	0.55	2
M6	L1	12%	1	1	0.4	2
M8	L2	12%	1	1	0.4	2



Figure A.1. Picture of the vial used for the production of the monoliths.

Appendix B - Chapter 3

Latex Synthesis

Table B.1. Recipes used for the synthesis of latexes L80/90, L90/110 and L100/110.

Latex L80/110						
	Core				Shell	
	IC	IS1	CF1	IF	CF2	IS2
H2O (g)	250	25	29.1	74		20
Styrene (g)			23.3		35.64	
DVB (g)			5.8		0.324	
SDS (g)	0.375		0.58			
KPS (g)		0.75		1.24		0.2
wt% crosslinker	20				1	
Diameter (nm)	80				107	
PDI	0.03				0.002	

Latex L90/110						
	Core				Shell	
	IC	IS1	CF1	IF	CF2	IS2
H2O (g)	250	25	36	50		45
Styrene (g)			28.5		23.76	
DVB (g)			7.1		0.24	
SDS (g)	0.375		0.39			
KPS (g)		0.75		1.25		0.75
wt% crosslinker	20				1	
Diameter (nm)	89				113	
PDI	0.03				0.01	

Latex L100/110						
	Core				Shell	
	IC	IS1	CF1	IF	CF2	IS2
H2O (g)	250	25	37.5	95.6		20
Styrene (g)			30		11.88	
DVB (g)			7.5		0.12	
SDS (g)	0.375		0.75			
KPS (g)		0.75		1.6		0.2
wt% crosslinker	20				1	
Diameter (nm)	98				111	
PDI	0.09				0.04	

Table B.2. Sequence of addition of the different feeds for latexes L80/110, L90/110 and L100/110.

Latex L80/110																								
Core														Shell										
1h	2h	3h	4h	5h	6h	7h	8h	9h	10h	11h	12h	13h	14h	15h	16h	17h	18h	19h	20h					
IC																								
IS1																								
CF1																								
IF1																								
														IS2										
														CF2										

Latex L90/110																				
Core																Shell				
1h	2h	3h	4h	5h	6h	7h	8h	9h	10h	11h	12h	13h	14h	15h	16h	17h	18h	19h	20h	
IC																				
IS1																				
CF1																				
IF1																				
																IS2				
																CF2				

Latex L100/110																				
Core																	Shell			
1h	2h	3h	4h	5h	6h	7h	8h	9h	10h	11h	12h	13h	14h	15h	16h	17h	18h	19h	20h	
IC																				
IS1																				
CF1																				
IF1																				
																	IS2			
																	CF2			

Table B.3. Recipes used for the synthesis of latexes L41/56 and L53/73.

Latex L41/56						
	Core				Shell	
	IC	IS1	CF1	IF	CF2	IS2
H ₂ O (g)	1024	48	103	12.2		25
Styrene (g)			82		95.4	
DVB (g)			20.5		0.96	
SDS (g)	3.24		0.6			
KPS (g)		1.3		0.65		0.75
wt% crosslinker	20				1	
Diameter (nm)	41				56	
PDI	0.06				0.04	

Latex L53/73						
	Core				Shell	
	IC	IS1	CF1	IF	CF2	IS2
H ₂ O (g)	250	25	23	65		25
Styrene (g)			18		27	
DVB (g)			5		0.27	
SDS (g)	0.375		0.5			
KPS (g)		0.75		1.29		0.5
wt% crosslinker	20				1	
diameter (nm)	53				73	
PDI	0.05				0.04	

Table B.4. Sequence of addition of the different feeds for latexes L41/56 and L53/73.

Latex L41/56							
Core			Shell				
1h	2h	3h	4h	5h	6h	7h	8h
IC							
IS1							
CF1							
IF1							
					IS2		
					CF2		

Latex L53/73																
Core												Shell				
1h	2h	3h	4h	5h	6h	7h	8h	9h	10h	11h	12h	13h	14h	15h	16h	17h
IC																
IS1																
CF1																
IF1																
												IS2				
												CF2				

Appendix C - Chapter 4

Atomic Charges and Parameterization

Polystyrene (PS), polyethylene glycol (PEG) and sodium dodecyl sulfate (SDS) have been parameterized by means of General Amber Force Field (GAFF)¹⁷³ which proved to be a suitable choice for polymer systems^{174,175}. Atomic charges have been computed through Restrained Electrostatic Potentials method (RESP)^{176,177}, according to the adopted force field. In particular, for PS and PEG, atomic charges have been obtained starting from oligomers with 6 repeating units; for polystyrene, a syndiotactic chain has been employed. First of all, molecular structures have been optimized *in vacuo* by means of density functional theory (DFT) calculations, at B3LYP/6-31G(d,p) level of theory. Electrostatic potentials have been subsequently obtained at HF/6-31G* level of theory *in vacuo* and used to fit atomic charges using a two-steps protocol. In the first phase, atomic charges have been obtained by assigning a proper value of the overall charge (0 for PS and PEG, 6 for protonated PEG and -1 for SDS); in the second step, charge equivalence for chemically equivalent atoms is imposed. All calculations have been carried out by means of Gaussian 09. This parameterization procedure led to the creation of libraries of initial, terminal and central units for the polymer chains; atomic coordinates, atom types and atomic charges for each unit and for SDS are listed in Tables C.1 – C.10. TIP3P water model has been here employed¹⁷⁸, while parameters for sodium and chloride ions have been taken from Joung and Cheatham works^{179,180}.

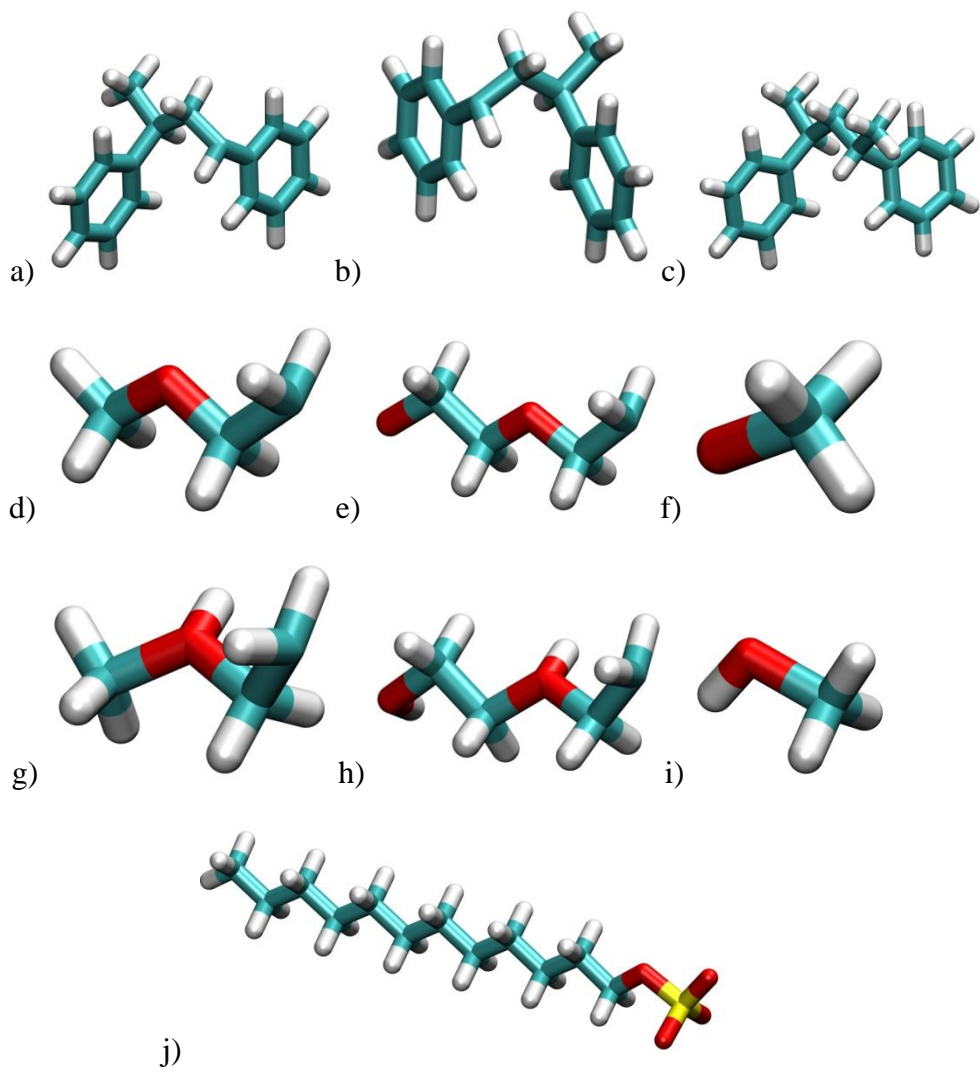


Figure C.1. Initial (a), central (b) and terminal (c) polystyrene fragments. Initial (d), central (e) and terminal (f) polyethylene glycol fragments. Initial (g), central (h) and terminal (i) protonated polyethylene glycol fragments. SDS structure (j).

Table C.1. Atom names, atom types, atomic coordinates and charges for initial unit of polystyrene chain.

Atom name	Atom type	X	Y	Z	Charge
C6	c3	-3.867	0.623	0.941	-0.028071
C7	c3	-4.962	0.715	2.031	-0.068535

C8	ca	-3.852	1.854	0.042	-0.010314
H6	hc	-4.101	-0.243	0.311	0.062813
C9	c3	-6.413	0.831	1.515	0.022099
H7	hc	-4.881	-0.167	2.68	0.036102
H8	hc	-4.756	1.581	2.675	0.036102
C10	c3	-7.38	1.1	2.684	-0.147219
H9	hc	-6.456	1.699	0.846	0.050306
C11	ca	-6.856	-0.382	0.705	0.031702
H10	hc	-8.408	1.211	2.326	0.036911
H11	hc	-7.368	0.278	3.409	0.036911
H12	hc	-7.103	2.017	3.215	0.036911
C17	ca	-4.11	1.74	-1.331	-0.086723
C18	ca	-4.106	2.862	-2.163	-0.196338
C19	ca	-3.844	4.126	-1.635	-0.10889
C20	ca	-3.585	4.256	-0.269	-0.196338
C21	ca	-3.589	3.133	0.557	-0.086723
H18	ha	-4.315	0.759	-1.751	0.113478
H19	ha	-4.309	2.746	-3.225	0.142309

H20	ha	-3.84	5	-2.28	0.130859
H21	ha	-3.377	5.236	0.153	0.142309
H22	ha	-3.385	3.256	1.618	0.113478
C22	ca	-7.296	-0.234	-0.617	-0.095617
C23	ca	-7.729	-1.333	-1.363	-0.219549
C24	ca	-7.73	-2.607	-0.796	-0.095067
C25	ca	-7.296	-2.771	0.521	-0.199362
C26	ca	-6.866	-1.671	1.261	-0.095617
H23	ha	-7.295	0.755	-1.067	0.109689
H24	ha	-8.064	-1.19	-2.386	0.150244
H25	ha	-8.065	-3.464	-1.373	0.126642
H26	ha	-7.293	-3.759	0.973	0.145809
H27	ha	-6.534	-1.819	2.286	0.109689

Table C.2. Atom names, atom types, atomic coordinates and charges for central unit of polystyrene chain.

Atom name	Atom type	X	Y	Z	Charge
C1	c3	0	0	1.466	-0.095499
H1	hc	-0.064	-0.874	2.128	0.037551
H2	hc	0.064	0.874	2.128	0.037551
C2	c3	1.308	-0.107	0.647	-0.016159
C3	c3	-1.308	0.107	0.647	-0.016159
H3	hc	-1.218	0.98	-0.009	0.070841
C4	ca	-1.534	-1.112	-0.241	-0.005738
C5	c3	-2.495	0.362	1.607	-0.095499
H4	hc	-2.6	-0.498	2.282	0.037551
H5	hc	-2.24	1.217	2.248	0.037551
C12	ca	-1.579	-0.982	-1.636	-0.081932
C13	ca	-1.785	-2.091	-2.459	-0.202964
C14	ca	-1.953	-3.357	-1.9	-0.108869
C15	ca	-1.911	-3.504	-0.512	-0.202964
C16	ca	-1.703	-2.394	0.306	-0.081932

H13	ha	-1.45	0.002	-2.078	0.114619
H14	ha	-1.815	-1.963	-3.537	0.143478
H15	ha	-2.114	-4.222	-2.537	0.13392
H16	ha	-2.04	-4.486	-0.065	0.143478
H17	ha	-1.673	-2.529	1.384	0.114619
C27	ca	1.534	1.112	-0.241	-0.005738
H28	hc	1.218	-0.98	-0.009	0.070841
C35	ca	1.579	0.982	-1.636	-0.081932
C36	ca	1.785	2.091	-2.459	-0.202964
C37	ca	1.953	3.357	-1.9	-0.108869
C38	ca	1.911	3.504	-0.512	-0.202964
C39	ca	1.703	2.394	0.306	-0.081932
H35	ha	1.45	-0.002	-2.078	0.114619
H36	ha	1.815	1.963	-3.537	0.143478
H37	ha	2.114	4.222	-2.537	0.13392
H38	ha	2.04	4.486	-0.065	0.143478
H39	ha	1.673	2.529	1.384	0.114619

Table C.3. Atom names, atom types, atomic coordinates and charges for terminal unit of polystyrene chain.

Atom name	Atom type	X	Y	Z	Charge
C28	c3	2.495	-0.362	1.607	-0.064285
C29	c3	3.867	-0.623	0.941	-0.008729
H29	hc	2.6	0.498	2.282	0.027025
H30	hc	2.24	-1.217	2.248	0.027025
C30	c3	4.962	-0.715	2.031	-0.06435
C31	ca	3.852	-1.854	0.042	0.003771
H31	hc	4.101	0.243	0.311	0.056036
C32	c3	6.413	-0.831	1.515	0.025776
H32	hc	4.881	0.167	2.68	0.031581
H33	hc	4.756	-1.581	2.675	0.031581
C33	c3	7.38	-1.1	2.684	-0.124687
H34	hc	6.456	-1.699	0.846	0.039554
C34	ca	6.856	0.382	0.705	0.022399
H40	hc	8.408	-1.211	2.326	0.031385
H41	hc	7.368	-0.278	3.409	0.031385

H42	hc	7.103	-2.017	3.215	0.031385
C40	ca	4.11	-1.74	-1.331	-0.08303
C41	ca	4.106	-2.862	-2.163	-0.204925
C42	ca	3.844	-4.126	-1.635	-0.110338
C43	ca	3.585	-4.256	-0.269	-0.204925
C44	ca	3.589	-3.133	0.557	-0.08303
H43	ha	4.315	-0.759	-1.751	0.110441
H44	ha	4.309	-2.746	-3.225	0.145552
H45	ha	3.84	-5	-2.28	0.133637
H46	ha	3.377	-5.236	0.153	0.145552
H47	ha	3.385	-3.256	1.618	0.110441
C45	ca	7.296	0.234	-0.617	-0.096693
C46	ca	7.729	1.333	-1.363	-0.203346
C47	ca	7.73	2.607	-0.796	-0.08865
C48	ca	7.296	2.771	0.521	-0.203346
C49	ca	6.866	1.671	1.261	-0.096693
H48	ha	7.295	-0.755	-1.067	0.112204
H49	ha	8.064	1.19	-2.386	0.142317

H50	ha	8.065	3.464	-1.373	0.123459
H51	ha	7.293	3.759	0.973	0.142317
H52	ha	6.534	1.819	2.286	0.112204

Table C.4. Atom names, atom types, atomic coordinates and charges for initial unit of polyethylene glycol chain.

Atom name	Atom type	X	Y	Z	Charge
C1	c3	-0.396	25.394	0	0.120997
O1	os	0.389	26.569	0	-0.40145
C2	c3	0.556	24.207	0	0.161543
H1	h1	-1.047	25.347	0.888	0.04075
H2	h1	-1.047	25.347	-0.888	0.04075
C3	c3	-0.389	27.747	0	0.035249
H3	h1	1.205	24.253	-0.888	0.034427
H4	h1	1.205	24.253	0.888	0.034427
H5	h1	0.302	28.593	0	0.053147
H6	h1	-1.032	27.812	-0.892	0.053147
H7	h1	-1.032	27.812	0.892	0.053147

Table C.5. Atom names, atom types, atomic coordinates and charges for central unit of polyethylene glycol chain.

Atom name	Atom type	X	Y	Z	Charge
O2	os	-0.229	23.029	0	-0.45201
C4	c3	0.545	21.845	0	0.151617
C5	c3	-0.419	20.669	0	0.151357
H8	h1	1.194	21.793	-0.888	0.037727
H9	h1	1.194	21.793	0.888	0.037727
O3	os	0.354	19.484	0	-0.45439
H10	h1	-1.068	20.72	0.888	0.037384
H11	h1	-1.068	20.72	-0.888	0.037384
C6	c3	-0.429	18.306	0	0.152203
C7	c3	0.526	17.122	0	0.147673
H12	h1	-1.078	18.259	0.888	0.037527
H13	h1	-1.078	18.259	-0.888	0.037527
H14	h1	1.175	17.169	-0.888	0.038921
H15	h1	1.175	17.169	0.888	0.038921
O2	os	-0.229	23.029	0	-0.45201

C4	c3	0.545	21.845	0	0.151617
C5	c3	-0.419	20.669	0	0.151357
H8	h1	1.194	21.793	-0.888	0.037727
H9	h1	1.194	21.793	0.888	0.037727
O3	os	0.354	19.484	0	-0.45439
H10	h1	-1.068	20.72	0.888	0.037384
H11	h1	-1.068	20.72	-0.888	0.037384
C6	c3	-0.429	18.306	0	0.152203
C7	c3	0.526	17.122	0	0.147673
H12	h1	-1.078	18.259	0.888	0.037527
H13	h1	-1.078	18.259	-0.888	0.037527
H14	h1	1.175	17.169	-0.888	0.038921
H15	h1	1.175	17.169	0.888	0.038921

Table C.6. Atom names, atom types, atomic coordinates and charges for terminal unit of polyethylene glycol chain.

Atom name	Atom type	X	Y	Z	Charge
O16	os	-0.389	-26.569	0	-0.40145
C32	c3	0.389	-27.747	0	0.035249

H64	h1	-0.302	-28.593	0	0.053147
H65	h1	1.032	-27.812	-0.892	0.053147
H66	h1	1.032	-27.812	0.892	0.053147

Table C.7. Atom names, atom types, atomic coordinates and charges for initial unit of protonated polyethylene glycol chain.

Atom name	Atom type	X	Y	Z	Charge
C1	c3	30.018	3.363	-0.29	-0.08287
O1	oh	29.059	2.228	0.306	-0.39107
C2	c3	27.94	1.684	-0.479	-0.11841
C3	c3	26.74	1.648	0.513	-0.04432
H1	h1	27.772	2.378	-1.304	0.220158
H2	h1	28.223	0.7	-0.865	0.220158
H3	h1	26.93	1.067	1.418	0.262615
H4	h1	26.321	2.634	0.72	0.262615
H5	h1	30.687	3.56	0.549	0.225086
H6	h1	30.505	2.923	-1.16	0.225086
H7	h1	29.345	4.191	-0.501	0.225086
H67	ho	29.616	1.533	0.722	0.539402

Table C.8. Atom names, atom types, atomic coordinates and charges for central unit of protonated polyethylene glycol chain.

Atom name	Atom type	X	Y	Z	Charge
O2	oh	25.493	0.897	-0.196	-0.33635
C4	c3	24.202	0.724	0.562	-0.18237
C5	c3	23.031	0.7	-0.482	0.027241
O3	oh	21.704	0.115	0.223	-0.30369
C6	c3	20.369	0.111	-0.533	-0.21218
C7	c3	19.186	0.078	0.512	0.00665
H8	h1	24.283	-0.194	1.154	0.2246
H9	h1	24.138	1.592	1.219	0.2246
H10	h1	22.708	1.696	-0.785	0.242497
H11	h1	23.204	0.039	-1.335	0.242497
H12	h1	20.377	1.043	-1.1	0.241764
H13	h1	20.387	-0.751	-1.206	0.241764
H14	h1	19.331	-0.631	1.331	0.245252
H15	h1	18.913	1.071	0.869	0.245252
H68	ho	25.8	0.048	-0.586	0.514647

H69	ho	21.894	-0.77	0.606	0.507516
O2	oh	25.493	0.897	-0.196	-0.33635
C4	c3	24.202	0.724	0.562	-0.18237
C5	c3	23.031	0.7	-0.482	0.027241
O3	oh	21.704	0.115	0.223	-0.30369
C6	c3	20.369	0.111	-0.533	-0.21218
C7	c3	19.186	0.078	0.512	0.00665
H8	h1	24.283	-0.194	1.154	0.2246
H9	h1	24.138	1.592	1.219	0.2246
H10	h1	22.708	1.696	-0.785	0.242497
H11	h1	23.204	0.039	-1.335	0.242497
H12	h1	20.377	1.043	-1.1	0.241764
H13	h1	20.387	-0.751	-1.206	0.241764
H14	h1	19.331	-0.631	1.331	0.245252
H15	h1	18.913	1.071	0.869	0.245252
H68	ho	25.8	0.048	-0.586	0.514647
H69	ho	21.894	-0.77	0.606	0.507516

Table C.9. Atom names, atom types, atomic coordinates and charges for terminal unit of protonated polyethylene glycol chain.

Atom name	Atom type	X	Y	Z	Charge
O16	oh	-29.059	2.227	-0.307	-0.39107
C32	c3	-30.018	3.364	0.289	-0.08287
H64	h1	-30.687	3.559	-0.55	0.225086
H65	h1	-30.505	2.923	1.159	0.225086
H66	h1	-29.345	4.191	0.5	0.225086
H82	ho	-29.616	1.532	-0.722	0.539402

Table C.10. Atom names, atom types, atomic coordinates and charges for SDS.

Atom name	Atom type	X	Y	Z	Charge
S1	s6	6.566	-0.075	0.011	1.220915
O1	o	6.609	-0.929	-1.197	-0.659133
O2	o	7.442	1.107	-0.028	-0.659133
O3	o	6.591	-0.833	1.282	-0.659133
O4	os	5.035	0.653	-0.028	-0.459882
C1	c3	3.922	-0.247	-0.011	0.106768
C2	c3	2.643	0.579	-0.02	0.032322

H1	h1	3.968	-0.903	-0.888	0.041588
H2	h1	3.972	-0.874	0.888	0.041588
C3	c3	1.381	-0.292	-0.014	0.01695
H3	hc	2.644	1.241	0.853	0.006552
H4	hc	2.646	1.225	-0.906	0.006552
C4	c3	0.08	0.519	-0.012	0.035573
H5	hc	1.391	-0.954	-0.89	-0.017762
H6	hc	1.396	-0.949	0.865	-0.017762
C5	c3	-1.183	-0.349	-0.012	0.027937
H7	hc	0.067	1.178	0.866	-0.017851
H8	hc	0.066	1.18	-0.888	-0.017851
C6	c3	-2.486	0.458	-0.005	0.015052
H9	hc	-1.17	-1.006	-0.892	-0.011381
H10	hc	-1.165	-1.013	0.862	-0.011381
C7	c3	-3.747	-0.413	-0.008	0.021411
H11	hc	-2.501	1.113	0.876	-0.00875
H12	hc	-2.504	1.124	-0.878	-0.00875
C8	c3	-5.052	0.392	0.002	0.028188

H13	hc	-3.733	-1.066	-0.89	-0.01082
H14	hc	-3.728	-1.08	0.864	-0.01082
C9	c3	-6.312	-0.481	-0.003	0.007977
H15	hc	-5.068	1.045	0.885	-0.013107
H16	hc	-5.072	1.06	-0.869	-0.013107
C10	c3	-7.618	0.323	0.009	0.011157
H17	hc	-6.297	-1.132	-0.886	-0.008889
H18	hc	-6.292	-1.149	0.867	-0.008889
C11	c3	-8.878	-0.55	0.003	0.049324
H19	hc	-7.635	0.974	0.893	-0.002411
H20	hc	-7.639	0.993	-0.86	-0.002411
C12	c3	-10.177	0.261	0.016	-0.066432
H21	hc	-8.862	-1.199	-0.881	-0.007617
H22	hc	-8.857	-1.22	0.872	-0.007617
H23	hc	-11.056	-0.39	0.011	0.010345
H24	hc	-10.239	0.894	0.907	0.010345
H25	hc	-10.244	0.915	-0.859	0.010345

Creation of the Molecular System

Polystyrene surface has been created according to the following protocol, used for other similar system^{181–184}. First of all, a simulation box containing 15 PS linear chains (each composed of 22 monomers) has been built. After energy minimization, 1 ns molecular dynamics (MD) simulation has been carried out in NVT ensemble at 500 K in order to obtain a homogeneous mixing of polymer chains. This box has been replicated four times on xy plane, in order to obtain 4 cells aimed at modeling an infinite PS surface by means of periodic boundary conditions. Again, after initial energy minimization, 1 ns MD simulation in NVT ensemble at 500 K has been carried out in order to assure a complete mixing between the 60 PS chains. Subsequently, 5 ns MD simulation at 300 K using semi-isotropic scaling *in vacuo* have been performed, allowing the system to reach the equilibrium density at 1 atm, equal to 0.99 g cm^{-3} . Finally, 1 ns MD in NVT ensemble at 300 K has been carried out increasing the length of the box in z direction, in order to adjust the arrangement of the chains on the surface. This approach led to a PS surface with $x \times y \times z$ dimensions of $8.87 \times 7.91 \times 6.63 \text{ nm}$.

Computational Protocol

All simulations have been performed by means of GROMACS 5.0.2¹⁸⁵ software, adopting the following protocol. First of all, energy minimization has been carried out in order to remove bad solvent/solvent and solvent/solute contacts, due to the random placement of ions and water explicit molecules. The temperature has been raised to 300 K by means of 20 ps in NVT ensemble; a weak harmonic restraint has been applied to the solute in order to avoid wild fluctuations. The system has been further equilibrated through 1 ns in NPT ensemble at 1 atm and 300 K, adopting a semi-isotropic barostat. Finally, molecular dynamics simulations have been performed in NPT ensemble at 1 atm and 300 K; temperature and pressure have been controlled by means of velocity rescale algorithm¹⁸⁶ and Parrinello - Rahman¹⁸⁷ semi-isotropic barostat, respectively. Cut-off value for long range interactions has been set equal to 1.2 \AA ;

electrostatic long-range interactions have been computed through Particle Mesh Ewald (PME) method¹⁸⁸. All covalent bonds involving hydrogen atoms have been restrained with LINCS algorithm¹⁸⁹; this allowed to use a time step for integration equal to 2 fs, along with Leap - Frog algorithm and periodic boundary conditions. Data have been collected every 20 ps. Simulation campaign has been performed as follows. A relaxed arrangement for both protonated and unprotonated PEG has been achieved by means of 40 ns MD simulations with explicit water molecules and ions for assuring electroneutrality (in this framework, an isotropic pressure scaling has been used). Polystyrene surface has been placed in xy plane and solvated along z axis (only on the top, in order to mimic a semi-infinite water/polymer interface) with explicit water molecules; explicit sodium dodecyl sulfate molecules have been added (along with Na^+ ions, in order to assure electroneutrality), and 100 ns molecular dynamics simulations have been performed in order to achieve surfactant adsorption on polymer surface. In the initial system configuration, 250 SDS molecules have been placed close to the surface with the aliphatic chain parallel to z axis and pointing towards polystyrene. The final system arrangement, where all SDS molecules are adsorbed on PS, corresponds to a surface density of 1.7 mg m^{-2} . The obtained value is consistent with literature data^{150,151} in terms of adsorption isotherms of SDS on polystyrene latexes and surfaces. In addition, the simulation led to a complete coverage of the surface by the surfactant, which can be expected because of the very low polymer content with respect to SDS. The obtained system has been used as input in order to study the pH-dependent binding with PEG model chain.

Two different systems have been here considered: one with protonated PEG (representative of a low environmental pH) and one with a neutral PEG (mimicking neutral/basic pH). For each system, two simulations have been carried out, since two different initial configurations have been adopted. In the first one the previously equilibrated structure of PEG model chain has been placed in the simulation box, while in the second one a fully stretched conformation has been considered. This procedure allows

In general, PS / SDS / PEG system has been solvated with explicit water molecules, and a proper amount of explicit ions has been added to assure electroneutrality. 100 ns MD simulations have been carried out for each system, in order to obtain a reasonable equilibrated PEG arrangement on the surface. Binding energy has been computed by means of Molecular Mechanics Poisson Boltzmann Surface Area method (*vide infra*) using the last 20 ns of the molecular trajectories. All performed simulations are summarized in Table C.11.

Table C.11. Summary of performed simulations. ^aAverage box size relative to the equilibrated system during MD simulation in NPT ensemble.

System	Box size [nm x nm x nm] ^a	Water molecules	SDS molecules	Ions	Total number of atoms	Simulation length [ns]
PEG	6.5 x 11.5 x 6.4	15684	-	-	47166	40
Protonated PEG	12.1 x 6.8 x 6.5	17605	-	16 (Cl ⁻)	52961	40
PS / SDS	8.8 x 7.9 x 20.4	28818	250	250 (Na ⁺)	136990	100
PS / SDS / PEG (relaxed)	8.8 x 7.9 x 20.1	28772	250	250 (Na ⁺)	137104	100
PS / SDS / PEG (stretched)	8.8 x 7.9 x 20.1	28772	250	250 (Na ⁺)	137104	100
PS / SDS / Protonated PEG (relaxed)	8.8 x 7.9 x 20.1	28772	250	234 (Na ⁺)	137104	100
PS / SDS / Protonated PEG (stretched)	8.8 x 7.9 x 20.1	28772	250	234 (Na ⁺)	137104	100

Molecular Mechanics Poisson Boltzmann Surface Area (MMPBSA) method

According to Molecular Mechanics Poisson Boltzmann Surface Area (MMPBSA) approach¹⁹⁰, interaction energy ΔE_{int} is given by the sum of two contributions:

$$\Delta E_{\text{int}} = \Delta E_{\text{gas}} + \Delta G_{\text{solv}} \quad (1)$$

where ΔE_{gas} is the gas phase energy given by the adopted force field and ΔG_{solv} is the solvation free energy. The first term on the right side in eq. 1 is in turn determined by three different terms: internal energy $\Delta E_{\text{internal}}$ (which accounts for bonds, angle and torsions), electrostatic interactions ΔE_{elec} and Van der Waals interactions ΔE_{vdw} :

$$\Delta E_{\text{gas}} = \Delta E_{\text{internal}} + \Delta E_{\text{elec}} + \Delta E_{\text{vdw}} \quad (2)$$

Solvation free energy is computed through a sum of a two contributions:

$$\Delta G_{\text{solv}} = \Delta G_{\text{pol}} + \Delta G_{\text{np}} \quad (3)$$

where ΔG_{pol} is the polar contribution to the solvation free energy, obtained by solving Poisson - Boltzmann equation (an implicit solvent model), and ΔG_{np} is the non polar contribution, computed as a function of Solvent Accessible Surface Area (SASA):

$$\Delta G_{\text{np}} = a \cdot \text{SASA} + b \quad (4)$$

where a is equal to $0.00542 \text{ kcal mol}^{-1} \text{ \AA}^{-2}$ and b is equal to $0.92 \text{ kcal mol}^{-1}$.

References

- (1) Hunter, R. J. *Foundation of Colloid Science 2nd Ed.*, 2nd ed.; Oxford University Press, Ed.; Oxford, 2001.
- (2) Tadros, T. F. Control of the Properties of Suspensions. *Colloids and Surfaces* **1986**, *18*, 137–173.
- (3) Derjaguin, B.; Landau, L. Theory of the Stability of Strongly Charged Lyophobic Sols and of the Adhesion of Strongly Charged Particles in Solutions of Electrolytes. *Prog. Surf. Sci.* **1993**, *43* (1–4), 30–59.
- (4) Verwey, E. J. W.; Overbeek, J. T. G. *Theory of Stability of Lyophobic Colloids*; Elsevier, Ed.; Amsterdam, 1948.
- (5) Hamaker, H. C. The London—van Der Waals Attraction between Spherical Particles. *Physica* **1937**, *4* (10), 1058–1072.
- (6) Lyklema, J. Principles of the Stability of Lyophobic Colloidal Dispersions in Non-Aqueous Media. *Adv. Colloid Interface Sci.* **1968**, *2*, 67–114.
- (7) Smoluchowski, M. v. Drei Vorträge Über Diffusion, Brownisch Molekularbewegung Und Koagulation von Kolloidteilchen. *Phys. Zeitschr.* **1916**, *17*, 557–571.
- (8) Smoluchowski, M. v. Versuch Einer Mathematischen Theorie Der Koagulationskinetik kolloider Lösungen. *Kolloid-Zeitschrift* **1917**, *21* (3), 98–104.
- (9) Fuchs, N. Über Die Stabilität Und Aufladung Der Aerosole. *Z. Phys.* **1934**, *89*, 736–743.
- (10) Reerink, H.; Overbeek, J. T. G. The Rate of Coagulation as a Measure of the Stability of Silver Iodide Sols. *Discuss. Faraday Soc.* **1954**, *18*, 74.
- (11) Tadros, T. F. *Emulsions : Formation, Stability, Industrial Applications*; De Gruyter, Ed.; Berlin, 2016.
- (12) Ottewill, R. H.; Rastogi, M. C. The Stability of Hydrophobic Sols in the Presence of Surface-Active Agents. Part 3. *Trans. Faraday Soc.* **1960**, *56*, 880–892.
- (13) Holthoff, H.; Schmitt, A.; Fernández-Barbero, A.; Borkovec, M.; Cabrerizo-Vílchez, M. A.; Schurtenberger, P.; Hidalgo-Álvarez, R. Measurement of Absolute Coagulation Rate Constants for Colloidal Particles: Comparison of Single and Multiparticle Light Scattering Techniques. *J. Colloid Interface Sci.* **1997**, *192* (2), 463–470.
- (14) Forrest, S. R.; Witten, T. A. Long-Range Correlations in Smoke-Particle Aggregates. *J. Phys. A Math. Gen.* **1979**, *12* (5), L109–L117.
- (15) Lin, M. Y.; Lindsay, H. M.; Weitz, D. A.; Ball, R. C.; Klein, R.; Meakin, P. Universality in Colloid Aggregation. *Nature* **1989**, *339* (6223), 360–362.
- (16) Wu, H.; Morbidelli, M. Gelation of Polymeric Nanoparticles. *Particuology* **2014**, *14*, 1–11.
- (17) Koumakis, N.; Moghimi, E.; Besseling, R.; Poon, W. C. K.; Brady, J. F.; Petekidis, G. Tuning Colloidal Gels by Shear. *Soft Matter* **2015**, *11* (23), 4640–4648.
- (18) Zaccarelli, E.; Buldyrev, S. V.; Nave, E. La; Moreno, A. J.; Sciortino, F.; Tartaglia, P. Model for Reversible Colloidal Gelation. *Phys. Rev. Lett.* **2005**, *94*, 218301.
- (19) Schmidt, D. F.; du Fresne von Hohenesche, C.; Weiss, A.; Schädler, V. Colloidal Gelation as a General Approach to the Production of Porous Materials. *Chem. Mater.* **2008**, *20*, 2851–2853.
- (20) Marti, N.; Quattrini, F.; Butté, A.; Morbidelli, M. Production of Polymeric Materials with Controlled Pore Structure: The Reactive Gelation Process. *Macromol. Mater. Eng.* **2005**, *290*, 221–229.
- (21) Brand, B.; Morbidelli, M.; Soos, M. Shear-Induced Reactive Gelation. *Langmuir* **2015**, *31*, 12727–12735.
- (22) Bechtle, M.; Butté, A.; Storti, G.; Morbidelli, M. Preparation of Macroporous Methacrylate-Based

- Monoliths for Chromatographic Applications by the Reactive Gelation Process. *J. Chromatogr. A* **2010**, *1217* (28), 4675–4681.
- (23) Lamprou, A.; Köse, I.; Storti, G.; Morbidelli, M.; Soos, M. Synthesis of Macroporous Polymer Particles Using Reactive Gelation under Shear. *Langmuir* **2014**, *30* (23), 6946–6953.
- (24) Wu, H.; Zaccone, A.; Tsoutsoura, A.; Lattuada, M.; Morbidelli, M. High Shear-Induced Gelation of Charge-Stabilized Colloids in a Microchannel without Adding Electrolytes. *Langmuir* **2009**, *25* (8), 4715–4723.
- (25) Lattuada, M.; Zaccone, A.; Morbidelli, M. Population-Balance Description of Shear-Induced Clustering, Gelation and Suspension Viscosity in Sheared DLVO Colloids. *Soft Matter* **2016**, *12*, 5313–5324.
- (26) Meng, X.; Wu, H.; Morbidelli, M. Kinetics and Cluster Morphology Evolution of Shear-Driven Aggregation of Well-Stabilized Colloids. *Langmuir* **2015**, *31* (3), 1113–1119.
- (27) Soos, M.; Ehrl, L.; Bäbler, M. U.; Morbidelli, M. Aggregate Breakup in a Contracting Nozzle. *Langmuir* **2010**, *26* (1), 10–18.
- (28) Harshe, Y. M.; Lattuada, M.; Soos, M. Experimental and Modeling Study of Breakage and Restructuring of Open and Dense Colloidal Aggregates. *Langmuir* **2011**, *27*, 5739–5752.
- (29) Harshe, Y. M.; Lattuada, M. Universal Breakup of Colloidal Clusters in Simple Shear Flow. *J. Phys. Chem. B* **2016**, *120*, 7244–7252.
- (30) Lazzari, S.; Nicoud, L.; Jaquet, B.; Lattuada, M.; Morbidelli, M. Fractal-like Structures in Colloid Science. *Adv. Colloid Interface Sci.* **2016**, *235*, 1–13.
- (31) Xie, D.; Wu, H.; Zaccone, A.; Braun, L.; Chen, H.; Morbidelli, M. Criticality for Shear-Induced Gelation of Charge-Stabilized Colloids. *Soft Matter* **2010**, *6*, 2691–2698.
- (32) Langmuir, I. The Role of Attractive and Repulsive Forces in the Formation of Tactoids, Thixotropic Gels, Protein Crystals and Coacervates. *J. Chem. Phys.* **1938**, *6* (12), 873–896.
- (33) Pieranski, P. Colloidal Crystals. *Contemp. Phys.* **1983**, *24* (1), 25–73.
- (34) Sacanna, S.; Pine, D. J.; Yi, G. Engineering Shape: The Novel Geometries of Colloidal Self-Assembly. *Soft Matter* **2013**, *9*, 8096–8106.
- (35) Pickering, S. U. Emulsions. *J. Chem. Soc. Trans.* **1907**, *91*, 2001–2021.
- (36) Wood, M. a. Colloidal Lithography and Current Fabrication Techniques Producing in-Plane Nanotopography for Biological Applications. *J. R. Soc. Interface* **2007**, *4* (12), 1–17.
- (37) Caruso, F.; Caruso, R. A.; Möhwald, H. Nanoengineering of Inorganic and Hybrid Hollow Spheres by Colloidal Templating. *Science* (80-.). **1998**, *282* (5391), 1111–1114.
- (38) Yuan, Q.; Cayre, O. J.; Fujii, S.; Armes, S. P.; Williams, R. A.; Biggs, S. Responsive Core-Shell Latex Particles as Colloidosome Microcapsule Membranes. *Langmuir* **2010**, *26* (23), 18408–18414.
- (39) Li, Z.; Ngai, T. Macroporous Polymer from Core-Shell Particle-Stabilized Pickering Emulsions. *Langmuir* **2010**, *26* (7), 5088–5092.
- (40) Velev, O. D.; Lenhoff, A. M. Colloidal Crystals as Templates for Porous Materials. *Curr. Opin. Colloid Interface Sci.* **2000**, *5*, 56–63.
- (41) Stanley, M. The Biochemistry of Viruses. *Annu. Rev. Biochem.* **1940**, *9*, 545–570.
- (42) Bernal, J. D.; Fankuchen, I. X-Ray and Crystallographic Studies of Plant Virus Preparations: I. Introduction and Preparation of Specimens II. Modes of Aggregation of the Virus Particles. *J. Gen. Physiol.* **1941**, *25* (1), 111–146.
- (43) Li, Z.; Wang, J.; Song, Y. Self-Assembly of Latex Particles for Colloidal Crystals. *Particuology* **2011**, *9* (6), 559–565.
- (44) Loiseau, E.; Niedermair, F.; Albrecht, G.; Frey, M.; Hauser, A.; Rühs, P. A.; Studart, A. R. Strong Microcapsules with Permeable Porous Shells Made through Phase Separation in Double

- Emulsions. *Langmuir* **2017**, *33* (9), 2402–2410.
- (45) Yi, G. R.; Jeon, S. J.; Thorsen, T.; Manoharan, V. N.; Quake, S. R.; Pine, D. J.; Yang, S. M. Generation of Uniform Photonic Balls by Template-Assisted Colloidal Crystallization. *Synth. Met.* **2003**, *139* (3), 803–806.
- (46) Patoka, P.; Giersig, M. Self-Assembly of Latex Particles for the Creation of Nanostructures with Tunable Plasmonic Properties. *J. Mater. Chem.* **2011**, *21*, 16783–16796.
- (47) Vignati, E.; Piazza, R.; Lockhart, T. P. Pickering Emulsions: Interfacial Tension, Colloidal Layer Morphology, and Trapped-Particle Motion. *Langmuir* **2003**, *19* (17), 6650–6656.
- (48) Lockhart, T. P.; Correra, S. Sistemi Colloidal. *Enciclopedia degli Idrocarburi*; Istituto della Enciclopedia Italiana Treccani, 2009.
- (49) Schwenke, K.; Isa, L.; Del Gado, E. Assembly of Nanoparticles at Liquid Interfaces: Crowding and Ordering. *Langmuir* **2014**, *30* (11), 3069–3074.
- (50) Isa, L.; Amstad, E.; Schwenke, K.; Del Gado, E.; Ilg, P.; Kröger, M.; Reimhult, E. Adsorption of Core-Shell Nanoparticles at Liquid–liquid Interfaces. *Soft Matter* **2011**, *7* (17), 7663.
- (51) Dinsmore, A. D.; Hsu, M. F.; Nikolaidis, M. G.; Marquez, M.; Bausch, A. R.; Weitz, D. A. Colloidosomes: Selectively Permeable Capsules Composed of Colloidal Particles. *Science* (80-.). **2002**, *298* (5595), 1006–1009.
- (52) Fortini, A. Clustering and Gelation of Hard Spheres Induced by the Pickering Effect. *Phys. Rev. E - Stat. Nonlinear, Soft Matter Phys.* **2012**, *85* (4), 1–4.
- (53) Cheng, H. L.; Velankar, S. S. Controlled Jamming of Particle-Laden Interfaces Using a Spinning Drop Tensiometer. *Langmuir* **2009**, *25* (8), 4412–4420.
- (54) Subramaniam, A. B.; Abkarian, M.; Stone, H. A. Controlled Assembly of Jammed Colloidal Shells on Fluid Droplets. *Nat. Mater.* **2005**, *4* (7), 553–556.
- (55) Koos, E.; Willenbacher, N. Capillary Forces in Suspension Rheology. *Science* (80-.). **2011**, *331* (6019), 897–900.
- (56) Cates, M. E.; Clegg, P. S. Bijels: A New Class of Soft Materials. *Soft Matter* **2008**, *4*, 2132.
- (57) Thompson, K. L.; Williams, M.; Armes, S. P. Colloidosomes: Synthesis, Properties and Applications. *J. Colloid Interface Sci.* **2015**, *447*, 217–228.
- (58) Storti, G.; Morbidelli, M.; Soos, M.; Lamprou, A.; Brand, B. Method for the Preparation of Macroporous Particles and Macroporous Particles Obtained Using Such a Method. WO 2014079580 A1, 2014.
- (59) Brand, B.; Krättli, M.; Storti, G.; Morbidelli, M. Strong Cation Exchange Monoliths for HPLC by Reactive Gelation. *J. Sep. Sci.* **2011**, *34* (16–17), 2159–2163.
- (60) Coquebert De Neuville, B.; Lamprou, A.; Morbidelli, M.; Soos, M. Perfusive Ion-Exchange Chromatographic Materials with High Capacity. *J. Chromatogr. A* **2014**, *1374*, 180–188.
- (61) Carta, G.; Rodrigues, A. E. Diffusion and Convection in Chromatographic Processes Using Permeable Supports with a Bidisperse Pore Structure. *Chem. Eng. Sci.* **1993**, *48* (23), 3927–3935.
- (62) Afeyan, N. B.; Gordon, N. F.; Mazsaroff, I.; Varady, L.; Fulton, S. P.; Yang, Y. B.; Regnier, F. E. Flow-through Particles for the High-Performance Liquid Chromatographic Separation of Biomolecules: Perfusion Chromatography. *J. Chromatogr. A* **1990**, *519* (1), 1–29.
- (63) Nischang, I. Porous Polymer Monoliths: Morphology, Porous Properties, Polymer Nanoscale Gel Structure and Their Impact on Chromatographic Performance. *J. Chromatogr. A* **2013**, *1287*, 39–58.
- (64) Guiochon, G. Monolithic Columns in High-Performance Liquid Chromatography. *J. Chromatogr. A* **2007**, *1168*, 101–168.
- (65) Garcia, M. C.; Marina, M. L.; To, M. Perfusion Chromatography: An Emergent Technique for the Analysis of Food Proteins. *J. Chromatogr. A* **2000**, *880*, 169–187.

- (66) Müller, W. New Ion Exchangers for the Chromatography of Biopolymers. *J. Chromatogr.* **1990**, No. 5, 133–140.
- (67) Brand, B. Macro-Porous Chromatographic Resins by Controlled Aggregation of Colloid Polymer Particles, ETH Zurich, 2014.
- (68) Rao, J. P.; Geckeler, K. E. Polymer Nanoparticles: Preparation Techniques and Size-Control Parameters. *Prog. Polym. Sci.* **2011**, *36* (7), 887–913.
- (69) Odian, G. *Principles of Polymerization*, 4th ed.; Wiley, J., Ed.; Hoboken, 1991.
- (70) Dinsmore, R. P. Synthetic Rubber and Method of Making It. U. S. 1732795A, 1929.
- (71) Smith, W.; Ewart, R. Kinetics of Emulsion Polymerization. *J. Chem. Phys.* **1948**, *16* (6), 592–599.
- (72) Hearn, J.; Wilkinson, M. C.; Goodall, A. R.; Chainey, M. Kinetics of the Emulsion Polymerization of Styrene: The Post Nucleation Stage. *J. Polym. Sci. Polym. Chem.* **1985**, *23*, 1869–1883.
- (73) Thickett, S. C.; Gilbert, R. G. Emulsion Polymerization: State of the Art in Kinetics and Mechanisms. *Polymer (Guildf)*. **2007**, *48*, 6965–6991.
- (74) Evans, C. E.; Lovell, P. A. Click Chemistry as a Route to Surface Functionalization of Polymer Particles Dispersed in Aqueous Media. *ChemComm* **2009**, 2305–2307.
- (75) Ouadahi, K.; Allard, E.; Oberleitner, B.; Larpent, C. Synthesis of Azide-Functionalized Nanoparticles by Microemulsion Polymerization and Surface Modification by Click Chemistry in Aqueous Medium. *J. Polym. Sci. Part A Polym. Chem.* **2012**, *50*, 314–328.
- (76) Breed, D. R.; Thibault, R.; Xie, F.; Wang, Q.; Hawker, C. J.; Pine, D. J. Functionalization of Polymer Microspheres Using Click Chemistry. *Langmuir* **2009**, *25* (8), 4370–4376.
- (77) Okubo, M. Control of Particle Morphology in Emulsion Polymerization. *Makromol. Chem., Macromol. Symp.* **1990**, *35/36*, 307–325.
- (78) Lazzari, S.; Jaquet, B.; Colonna, L.; Storti, G.; Lattuada, M.; Morbidelli, M. Interplay between Aggregation and Coalescence of Polymeric Particles : Experimental and Modeling Insights. *Langmuir* **2015**, *31*, 9296–9305.
- (79) Van Berkel, K. Y.; Hawker, C. J. Tailored Composite Polymer-Metal Nanoparticles by Miniemulsion Polymerization and Thiol-Ene Functionalization. *J. Polym. Sci. Part A Polym. Chem.* **2010**, *48* (7), 1594–1606.
- (80) Rodionov, V.; Gao, H.; Scroggins, S.; Unruh, D. A.; Avestro, A.; Frechet, J. M. J. Easy Access to a Family of Polymer Catalysts from Modular Star Polymers. *J. Am. Chem. Soc.* **2010**, *132* (8), 2570–2572.
- (81) Chen, Y.-C.; Dimonie, V. L.; El-Aasser, M. S. Interfacial Phenomena Controlling Particle Morphology. *J. Appl. Polym. Sci.* **1991**, *42*, 1049–1063.
- (82) Sciortino, F.; Zaccarelli, E. Reversible Gels of Patchy Particles. *Curr. Opin. Solid State Mater. Sci.* **2011**, *15* (6), 246–253.
- (83) Dobler, E.; Lambla, M.; Holl, Y. Coalescence Mechanisms of Polymer Colloids. *Prog. Colloid Polym. Sci.* **1993**, *52*, 51–52.
- (84) Rosenzweig, N.; Narkis, M. Coalescence Phenomenology of Spherical Polymer Particles by Sintering. *Polym. (United Kingdom)* **1980**, *21* (9), 988–989.
- (85) Jaquet, B.; Lazzari, S.; Colonna, L.; Colonna, G.; Soos, M.; Morbidelli, M. Effects of Coalescence on Shear-Induced Gelation of Colloids. *Langmuir* **2017**, *33* (5), 1180–1188.
- (86) Chen, G.-F.; Peisheng, L. General Introduction to Porous Materials. In *Porous Materials: Processing and Applications*; 2014; pp 1–19.
- (87) Barrande, M.; Beurroies, I.; Denoyel, R.; Tatárová, I.; Gramblička, M.; Polakovič, M.; Joehnck, M.; Schulte, M. Characterisation of Porous Materials for Bioseparation. *J. Chromatogr. A* **2009**, *1216*, 6906–6916.
- (88) Sorensen, C. M. Light Scattering by Fractal Aggregates: A Review. *Aerosol Sci. Technol. Am.*

- Assoc. Aerosol Res.* **2001**, *35*, 648–687.
- (89) Lattuada, M.; Wu, H.; Morbidelli, M. A Simple Model for the Structure of Fractal Aggregates. *J. Colloid Interface Sci.* **2003**, *268*, 106–120.
- (90) Lee, C.; Kramer, T. A. Prediction of Three-Dimensional Fractal Dimensions Using the Two-Dimensional Properties of Fractal Aggregates. *Adv. Colloid Interface Sci.* **2004**, *112* (1–3), 49–57.
- (91) Brunauer, S.; Emmett, P. H.; Teller, E. Adsorption of Gases in Multimolecular Layers. *J. Am. Chem. Soc.* **1938**, *60* (2), 309–319.
- (92) Giesche, H. Mercury Porosimetry: A General (Practical) Overview. *Part. Part. Syst. Charact.* **2006**, *23*, 9–19.
- (93) Anovitz, L. M.; Cole, D. R. Characterization and Analysis of Porosity and Pore Structures. *Rev. Mineral. Geochemistry* **2015**, *80* (1), 61–164.
- (94) Dephills, P.; Lenhoff, A. M. Pore Size Distributions of Cation-Exchange Adsorbents Determined by Inverse Size-Exclusion Chromatography. *J. Chromatogr. A* **2000**, *883*, 39–54.
- (95) Brown, W. *Light Scattering*; Clarendon Press, Ed.; Oxford, 1996.
- (96) Lattuada, M.; Wu, H.; Morbidelli, M. Hydrodynamic Radius of Fractal Clusters. *J. Colloid Interface Sci.* **2003**, *268*, 96–105.
- (97) Rouquerol, J.; Baron, G.; Denoyel, R.; Giesche, H.; Groen, J.; Klobes, P.; Levitz, P.; Neimark, A. V.; Rigby, S.; Skudas, R.; Sing, K.; Thommes, M.; Unger, K. Liquid Intrusion and Alternative Methods for the Characterization of Macroporous Materials (IUPAC Technical Report). *Pure Appl. Chem.* **2011**, *84* (1), 107–136.
- (98) He, H.; Guo, Z.; Stroeven, P.; Stroeven, M.; Sluys, L. J. Characterization of the Packing of Aggregate in Concrete by a Discrete Element Approach. *Mater. Charact.* **2009**, *60* (10), 1082–1087.
- (99) Baranau, V.; Tallarek, U. Random-Close Packing Limits for Monodisperse and Polydisperse Hard Spheres. *Soft Matter* **2014**, *10*, 3826–3841.
- (100) Ta Aro, I.; Gramblička, M.; Antoško, M.; Polakovič, M. Characterization of Pore Structure of Chromatographic Adsorbents Employed in Separation of Monoclonal Antibodies Using Size-Exclusion Techniques. *J. Chromatogr. A* **2008**, *1193*, 129–135.
- (101) Halász, I.; Martin, K. Porengrößen von Festkörpern. *Angew. Chemie* **1978**, *90*, 954–961.
- (102) Armstrong, J. K.; Wenby, R. B.; Meiselman, H. J.; Fisher, T. C. The Hydrodynamic Radii of Macromolecules and Their Effect on Red Blood Cell Aggregation. *Biophys. J.* **2004**, *87* (6), 4259–4270.
- (103) Hagel, L.; Östberg, M.; Andersson, T. Apparent Pore Size Distributions of Chromatography Media. *J. Chromatogr. A* **1996**, *743* (1), 33–42.
- (104) Pawley, J. B. *Handbook of Biological Confocal Microscopy*, 2nd ed.; Springer, Ed.; New York, 2006.
- (105) Egerton, R. F. *Physical Principles of Electron Microscopy*; Springer, Ed.; New York, 2005.
- (106) Smith, K. C. A.; Oatley, C. W. The Scanning Electron Microscope and Its Fields of Application. *Br. J. Appl. Phys.* **1955**, *6* (11), 391–399.
- (107) Hentze, H. P.; Antonietti, M. Porous Polymers and Resins for Biotechnological and Biomedical Applications. *Rev. Mol. Biotechnol.* **2002**, *90* (1), 27–53.
- (108) Magistris, A.; Quartarone, E.; Mustarelli, P.; Saito, Y.; Kataoka, H. PVDF-Based Porous Polymer Electrolytes for Lithium Batteries. *Solid State Ionics* **2002**, *152*, 347–354.
- (109) Kaur, P.; Hupp, J. T.; Nguyen, S. T. Porous Organic Polymers in Catalysis: Opportunities and Challenges. *ACS Catal.* **2011**, 819–835.
- (110) Lu, W.; Yuan, D.; Zhao, D.; Schilling, C. I.; Plietzsch, O.; Muller, T.; Bräse, S.; Guenther, J.;

- Blümel, J.; Krishna, R.; Li, Z.; Zhou, H. C. Porous Polymer Networks: Synthesis, Porosity, and Applications in Gas Storage/separation. *Chem. Mater.* **2010**, *22* (21), 5964–5972.
- (111) Gokmen, M. Talha; Du Prez, F. E. Porous Polymer particles—A Comprehensive Guide to Synthesis, Characterization, Functionalization and Applications. *Prog. Polym. Sci.* **2012**, *37*, 365–405.
- (112) Maniglio, D.; Ding, Y.; Wang, L.; Migliaresi, C. One-Step Process to Create Porous Structures in Cross-Linked Polymer Films via Breath-Figure Formations during in Situ Cross-Linking Reactions. *Polymer (Guildf)*. **2011**, *52* (22), 5102–5106.
- (113) Saba, S. A.; Mousavi, M. P. S.; Bühlmann, P.; Hillmyer, M. A. Hierarchically Porous Polymer Monoliths by Combining Controlled Macro- and Microphase Separation. *J. Am. Chem. Soc.* **2015**, *137* (28), 8896–8899.
- (114) Svec, F. Porous Polymer Monoliths: Amazingly Wide Variety of Techniques Enabling Their Preparation. *J. Chromatogr. A* **2010**, *1217* (6), 902–924.
- (115) Maya, F.; Svec, F. A New Approach to the Preparation of Large Surface Area Poly(styrene-Co-Divinylbenzene) Monoliths via Knitting of Loose Chains Using External Crosslinkers and Application of These Monolithic Columns for Separation of Small Molecules. *Polym. (United Kingdom)* **2014**, *55* (1), 340–346.
- (116) Svec, F.; Frechet, J. M. J. Kinetic Control of Pore Formation in Macroporous Polymers. Formation of “Molded” Porous Materials with High Flow Characteristics for Separations or Catalysis. *Chem. Mater.* **1995**, *7* (6), 707–715.
- (117) Jones, B. H.; Lodge, T. P. From Block Polymer Confinement within Bicontinuous Microemulsion-Derived Nanoporous Polyethylene. *ACS Nano* **2011**, No. 11, 8914–8927.
- (118) Valkama, S.; Nykänen, A.; Kosonen, H.; Ramani, R.; Tuomisto, F.; Engelhardt, P.; Ten Brinke, G.; Ikkala, O.; Ruokolainen, J. Hierarchical Porosity in Self-Assembled Polymers: Post-Modification of Block Copolymer-Phenolic Resin Complexes by Pyrolysis Allows the Control of Micro- and Mesoporosity. *Adv. Funct. Mater.* **2007**, *17* (2), 183–190.
- (119) Chen, J. H.; Ruckenstein, E. Generation of Porous Polymer Surfaces by Solvent Nonsolvent Treatment. *J. Appl. Polym. Sci.* **1992**, *45* (3), 377–386.
- (120) Cuadros, T. R.; Aguilera, J. M. Gels as Precursors of Porous Matrices for Use in Foods: A Review. *Food Biophys.* **2015**, *10* (4), 487–499.
- (121) Lamprou, A.; Köse, I.; Peña Aguirre, Z.; Storti, G.; Morbidelli, M.; Soos, M. Macroporous Polymer Particles via Reactive Gelation under Shear: Effect of Primary Particle Properties and Operating Parameters. *Langmuir* **2014**, *30*, 13970–13978.
- (122) Hrubesh, L. W.; Pekala, R. W. Thermal Properties of Organic and Inorganic Aerogels. *J. Mater. Res.* **1994**, *9* (3), 731–738.
- (123) Chow, S. Molecular Interpretation of the Glass Transition Temperature of Polymer-Diluent Systems. *Macromolecules* **1980**, *364* (12), 362–364.
- (124) Arosio, P.; Xie, D.; Wu, H.; Braun, L.; Morbidelli, M. Effect of Primary Particle Morphology on the Structure of Gels Formed in Intense Turbulent Shear. *Langmuir* **2010**, *26* (9), 6643–6649.
- (125) Smith, D. M. Pore Size Analysis of Wet Materials via Low-Field NMR. *Charact. Porous Solids II* **1991**, 301–310.
- (126) Carta, G.; Jungbauer, A. *Downstream Processing of Biotechnology Products*; 2010.
- (127) Guiochon, G. Basic Principles of Chromatography. In *Ulmann's Encyclopedia of Industrial Chemistry*; -VCH, Wiley, 2012.
- (128) Sherrington, D. C. Preparation, Structure and Morphology of Polymer Supports. *Chem. Commun.* **1998**, No. 21, 2275–2286.
- (129) Chen, G.-F.; Peisheng, L. Applications of Polymer Foams. In *Porous Materials: Processing and*

Applications; Butterworth-Heinemann, Ed.; 2014; pp 383–410.

- (130) Galia, M.; Svec, F.; Frechet, J. M. J. Monodisperse Polymer Beads as Packing Material for High-Performance Liquid Chromatography: Effect of Divinylbenzene Content on the Porous and Chromatographic Properties of Poly(styrene-Co-Divinylbenzene) Beads Prepared in Presence of Linear Polystyrene as. *J. Polym. Sci. Part A Polym. Chem.* **1994**, *32* (11), 2169–2175.
- (131) Zaccone, A.; Gentili, D.; Wu, H.; Morbidelli, M.; Gado, E. Del. Shear-Driven Solidification of Dilute Colloidal Suspensions. *Phys. Rev. Lett.* **2011**, *106*, 138301.
- (132) Wu, H.; Tsoutsoura, A.; Lattuada, M.; Zaccone, A.; Morbidelli, M. Effect of Temperature on High Shear-Induced Gelation of Charge-Stabilized Colloids without Adding Electrolytes. *Langmuir* **2010**, *26* (4), 2761–2768.
- (133) Xie, D.; Wu, H.; Zaccone, A.; Braun, L.; Chen, H.; Morbidelli, M. Criticality for Shear-Induced Gelation of Charge-Stabilized Colloids. *Soft Matter* **2010**, *6*, 2692–2698.
- (134) Lamprou, A. Synthesis and Application of Novel Polymeric Materials: Short Surfactants via ATRP and Functional Macroporous Particles via Reactive Gelation under Shear, ETH Zurich, 2012.
- (135) Zaccone, A.; Gentili, D.; Wu, H.; Morbidelli, M. Shear-Induced Reaction-Limited Aggregation Kinetics of Brownian Particles at Arbitrary Concentrations. *J. Chem. Phys. J. Rheol* **2010**, *132* (43), 134903–673.
- (136) Bollhorst, T.; Rezwani, K.; Maas, M. Colloidal Capsules: Nano- and Microcapsules with Colloidal Particle Shells. *Chem. Soc. Rev.* **2017**, *46* (8), 2091–2126.
- (137) Velez, O. D.; Furusawa, K.; Nagayama, K. Assembly of Latex Particles by Using Emulsion Droplets as Templates. 1. Microstructured Hollow Spheres. *Langmuir* **1996**, *12* (10), 2374–2384.
- (138) Sim, J. Y.; Choi, J. H.; Lim, J. M.; Cho, S.; Kim, S. H.; Yang, S. M. Microfluidic Molding of Photonic Microparticles with Engraved Elastomeric Membranes. *Small* **2014**, *10* (19), 3979–3985.
- (139) Fan, J.; Kim, S. H.; Chen, Z.; Zhou, S.; Amstad, E.; Lin, T.; Weitz, D. A. Creation of Faceted Polyhedral Microgels from Compressed Emulsions. *Small* **2017**, 1–7.
- (140) Yow, H. N.; Routh, A. F. Release Profiles of Encapsulated Actives from Colloidosomes Sintered for Various Durations. *Langmuir* **2009**, *25* (1), 159–166.
- (141) Chen, Y.; Wang, C.; Chen, J.; Liu, X.; Tong, Z. Growth of Lightly Crosslinked PHEMA Brushes and Capsule Formation Using Pickering Emulsion Interface-Initiated ATRP. *J. Polym. Sci. Part A Polym. Chem.* **2009**, *47*, 1354–1367.
- (142) Lin, Y.; Skaff, H.; Böker, A.; Dinsmore, A. D.; Emrick, T.; Russell, T. P. Ultrathin Cross-Linked Nanoparticle Membranes. *J. Am. Chem. Soc.* **2003**, *125* (42), 12690–12691.
- (143) Wang, B.; Prinsen, P.; Wang, H.; Bai, Z.; Wang, H.; Luque, R.; Xuan, J. Macroporous Materials: Microfluidic Fabrication, Functionalization and Applications. *Chem. Soc. Rev.* **2017**, *46* (3), 855–914.
- (144) Lin, M. Y.; Lindsay, H. M.; Weitz, D. A.; Ball, R. C.; Klein, R.; Meakin, P. Universality in Colloid Aggregation. *Nature* **1989**, *339*, 360–362.
- (145) Agresti, J. J.; Weitz, D. A.; Hutchison, J. B.; Gifiths, A.; El Harrak, A.; Miller, O. J.; Barat, J.-C.; Taly, V.; Merton, C.; Holtze, C.; Agresti, J. J.; A, W. D.; Ahn, K.; Hutchison, J. B.; Gifiths, A.; Miller, O. J.; Ryckelynck, M. Fluorocarbon Emulsion Stabilizing Surfactants. **2010**, *1* (60), 1–44.
- (146) Baret, J.-C. Surfactants in Droplet-Based Microfluidics. *Lab Chip* **2012**, *12* (3), 422–433.
- (147) Guo, W.; Sun, Y. W.; Luo, G. S.; Wang, Y. J. Interaction of PEG with Ionic Surfactant SDS to Form Template for Mesoporous Material. *Colloids Surfaces A Physicochem. Eng. Asp.* **2005**, *252* (1), 71–77.
- (148) Bernazzani, L.; Borsacchi, S.; Catalano, D.; Gianni, P.; Mollica, V.; Vitelli, M.; Asaro, F.; Feruglio, L. On the Interaction of Sodium Dodecyl Sulfate with Oligomers of Poly(ethylene

- Glycol) in Aqueous Solution. *J. Phys. Chem. B* **2004**, *108* (26), 8960–8969.
- (149) Majumder, M.; Rendall, C. S.; Eukel, J. A.; Wang, J. Y. L.; Behabtu, N.; Pint, C. L.; Liu, T. Y.; Orbaek, A. W.; Mirri, F.; Nam, J.; Barron, A. R.; Hauge, R. H.; Schmidt, H. K.; Pasquali, M. Overcoming The “coffee-Stain” effect by Compositional Marangoni-Flow-Assisted Drop-Drying. *J. Phys. Chem. B* **2012**, *116* (22), 6536–6542.
- (150) Meconi, G. M.; Ballard, N.; Asua, J. M.; Zangi, R. Adsorption and Desorption Behavior of Ionic and Nonionic Surfactants on Polymer Surfaces. *Soft Matter* **2016**, *12* (48), 9692–9704.
- (151) Turner, S. F.; Clarke, S. M.; Rennie, A. R.; Thirtle, P. N.; Cooke, D. J.; Li, Z. X.; Thomas, R. K. Adsorption of Sodium Dodecyl Sulfate to a Polystyrene/Water Interface Studied by Neutron Reflection and Attenuated Total Reflection Infrared Spectroscopy. *Langmuir* **1999**, *15* (4), 1017–1023.
- (152) Elgebrandt, R. C.; Romagnoli, J. A.; Fletcher, D. F.; Gomes, V. G.; Gilbert, R. G. Analysis of Shear-Induced Coagulation in an Emulsion Polymerisation Reactor Using Computational Fluid Dynamics. *Chem. Eng. Sci.* **2005**, *60* (7), 2005–2015.
- (153) Boer, G. B. J.; Hoedemakers, G. F. M.; Thoenes, D. Coagulation in Turbulent Flow: Part I. *Chem Eng Res Des.* 1989, p 6.
- (154) Serra, T.; Casamitjana, X. Structure of the Aggregates During the Process of Aggregation and Breakup Under a Shear Flow. *J. Colloid Interface Sci.* **1998**, *206* (2), 505–511.
- (155) Serra, T.; Casamitjana, X. Effect of the Shear and Volume Fraction on the Aggregation and Breakup of Particles. *AIChE J.* **1998**, *44* (8), 1724–1730.
- (156) Soos, M.; Moussa, A. S.; Ehrl, L.; Sefcik, J.; Wu, H.; Morbidelli, M. Effect of Shear Rate on Aggregate Size and Morphology Investigated under Turbulent Conditions in Stirred Tank. *J. Colloid Interface Sci.* **2008**, *319* (2), 577–589.
- (157) Ehrl, L.; Soos, M.; Morbidelli, M. Dependence of Aggregate Strength, Structure, and Light Scattering Properties on Primary Particle Size under Turbulent Conditions in Stirred Tank. *Langmuir* **2008**, *24*, 3070–3081.
- (158) Israelachvili, J. *Intermolecular and Surface Forces*; 2011.
- (159) Moussa, A. S.; Lattuada, M.; Conchuir, B.; Zaccone, A.; Morbidelli, M.; Soos, M. Flow-Induced Aggregation and Breakup of Particle Clusters Controlled by Surface Nanoroughness. *Langmuir* **2013**, *29*, 14386–14395.
- (160) Hodges, C. S.; Cleaver, J. A. S.; Ghadiri, M.; Jones, R.; Pollock, H. M. Forces between Polystyrene Particles in Water Using the AFM: Pull-off Force vs Particle Size. *Langmuir* **2002**, *18* (15), 5741–5748.
- (161) Hodges, C. S.; Looi, L.; Cleaver, J. A. S.; Ghadiri, M. Use of the JKR Model for Calculating Adhesion between Rough Surfaces. *Langmuir* **2004**, *20* (22), 9571–9576.
- (162) Ouesnel, D. J.; Rimai, D. S.; DeMejo, L. P. Molecular Dynamic Simulation of Adhesional Release of Particles from Surfaces. *Am. Chem. Soc. Polym. Prepr. Div. Polym. Chem.* **1996**, *37* (2), 59–60.
- (163) Klein, J.; Briscoe, W. H.; Chen, M.; Eiser, E.; Kampf, N.; Raviv, U.; Tadmor, R.; Tsarkova, L. Polymer Brushes and Surface Forces. *Polym. Adhes. Frict. Lubr.* **2013**, 135–176.
- (164) Brandrup, J.; Immergut, E. H.; Grulke, E. A. *Polymer Handbook*; John Wiley & Sons, Ed.; New York, 1999.
- (165) Cova, L.; Bigini, P.; Diana, V.; Sitia, L.; Ferrari, R.; Pesce, R. M.; Khalaf, R.; Bossolasco, P.; Ubezio, P.; Lupi, M.; Tortarolo, M.; Colombo, L.; Giardino, D.; Silani, V.; Morbidelli, M.; Salmona, M.; Moscatelli, D. Biocompatible Fluorescent Nanoparticles for in Vivo Stem Cell Tracking. *Nanotechnology* **2013**, *24* (24), 245603.
- (166) Lee, K. C.; Wi, H. A. Synthesis of Crosslinked Polystyrene Particles by Seeded Batch

- Polymerization with Monomer Absorption. *Trans. Nonferrous Met. Soc. China (English Ed.* **2011**, 21 (SUPPL. 1), s153–s159.
- (167) Soos, M.; Kaufmann, R.; Winteler, R.; Kroupa, M.; Lüthi, B. Determination of Maximum Turbulent Energy Dissipation Rate Generated by a Rushton Impeller through Large Eddy Simulation. *AIChE J.* **2013**, 59, 3642–3658.
- (168) Kim, S. H.; Hollingsworth, A. D.; Sacanna, S.; Chang, S. J.; Lee, G.; Pine, D. J.; Yi, G. R. Synthesis and Assembly of Colloidal Particles with Sticky Dimples. *J. Am. Chem. Soc.* **2012**, 134 (39), 16115–16118.
- (169) Sacanna, S.; Korpics, M.; Rodriguez, K.; Colón-Meléndez, L.; Kim, S.-H.; Pine, D. J.; Yi, G.-R. Shaping Colloids for Self-Assembly. *Nat. Commun.* **2013**, 4, 1688.
- (170) Friedlander, S. K. *Smoke, Dust and Haze Fundamentals of Aerosol Dynamics*, 2nd ed.; Oxford University Press, Ed.; New York, 2000.
- (171) Sorensen, C. M.; Roberts, G. C. The Prefactor of Fractal Aggregates. *J. Colloid Interface Sci.* **1997**, 186 (2), 447–452.
- (172) Bäbler, M. U. A Collision Efficiency Model for Flow-Induced Coagulation of Fractal Aggregates. *AIChE J.* **2008**, 54, 1748–1760.
- (173) Wang, J. M.; Wolf, R. M.; Caldwell, J. W.; Kollman, P. a; Case, D. a. Development and Testing of a General Amber Force Field. *J. Comput. Chem.* **2004**, 25 (9), 1157–1174.
- (174) Colombo, C.; Gatti, S.; Ferrari, R.; Casalini, T.; Cuccato, D.; Morosi, L.; Zucchetti, M.; Moscatelli, D. Self-Assembling Amphiphilic PEGylated Block Copolymers Obtained through RAFT Polymerization for Drug-Delivery Applications. *J. Appl. Polym. Sci.* **2016**, 133 (11), 1–8.
- (175) Baker, M. B.; Albertazzi, L.; Voets, I. K.; Leenders, C. M. A.; Palmans, A. R. A.; Pavan, G. M.; Meijer, E. W. Consequences of Chirality on the Dynamics of a Water-Soluble Supramolecular Polymer. *Nat. Commun.* **2015**, 6, 6234.
- (176) Cornell, W. D.; Cieplak, P.; Bayly, C. I.; Kollman, P. A. Application of RESP Charges To Calculate Conformational Energies, Hydrogen Bond Energies, and Free Energies of Solvation. *J. Am. Chem. Soc.* **1993**, 115 (21), 9620–9631.
- (177) Bayly, C. I.; Cieplak, P.; Cornell, W.; Kollman, P. A. A Well-Behaved Electrostatic Potential Based Method Using Charge Restraints for Deriving Atomic Charges: The RESP Model. *J. Phys. Chem.* **1993**, 97 (40), 10269–10280.
- (178) Jorgensen, W. L.; Chandrasekhar, J.; Madura, J. D.; Impey, R. W.; Klein, M. L.; Jorgensen, W. L.; Chandrasekhar, J.; Madura, J. D.; Impey, R. W.; Klein, M. L. Comparison of Simple Potential Functions for Simulating Liquid Water Comparison of Simple Potential Functions for Simulating Liquid Water. *J. Chem. PhysicsJournal* **1983**, 79, 926.
- (179) Joung, I. S.; Cheatham, T. E. Determination of Alkali and Halide Monovalent Ion Parameters for Use in Explicitly Solvated Biomolecular Simulations. *J. Phys. Chem. B* **2008**, 112 (30), 9020–9041.
- (180) Joung, I. S.; Cheatham, T. E. Molecular Dynamics Simulations of the Dynamic and Energetic Properties of Alkali and Halide Ions Using Water-Model-Specific Ion Parameters. *J. Phys. Chem. B* **2009**, 113, 13279–13290.
- (181) Doni, G.; Nkoua Ngavouka, M. D.; Barducci, A.; Parisse, P.; De Vita, A.; Scoles, G.; Casalis, L.; Pavan, G. M. Structural and Energetic Basis for Hybridization Limits in High-Density DNA Monolayers. *Nanoscale* **2013**, 5 (20), 9988.
- (182) Rotella, C.; Bosco, A.; Pavan, G. M.; Castronovo, M.; De Vita, A.; Casalis, L.; Doni, G.; Parisse, P. Site Accessibility Tailors DNA Cleavage by Restriction Enzymes in DNA Confined Monolayers. *Nanoscale* **2017**, 9 (19), 6399–6405.
- (183) Enciso, A. E.; Doni, G.; Nifosi, R.; Palazzesi, F.; Gonzalez, R.; Ellsworth, A. A.; Coffey, J. L.;

- Walker, A. V.; Pavan, G. M.; Mohamed, A. A.; Simanek, E. E. Facile Synthesis of Stable, Water Soluble, Dendron-Coated Gold Nanoparticles. *Nanoscale* **2017**, *9* (9), 3128–3132.
- (184) Prigodich, A. E.; Lee, O.-S.; Daniel, W. L.; Seferos, D. S.; Schatz, G. C.; Mirkin, C. A. Tailoring DNA Astructure To Increase Target Hydrization Kinetics on Surface. *J. Am. Chem. Soc.* **2010**, *132*, 10638–10641.
- (185) Pronk, S.; Páll, S.; Schulz, R.; Larsson, P.; Bjelkmar, P.; Apostolov, R.; Shirts, M. R.; Smith, J. C.; Kasson, P. M.; Van Der Spoel, D.; Hess, B.; Lindahl, E. GROMACS 4.5: A High-Throughput and Highly Parallel Open Source Molecular Simulation Toolkit. *Bioinformatics* **2013**, *29* (7), 845–854.
- (186) Bussi, G.; Donadio, D.; Parrinello, M. Canonical Sampling through Velocity Rescaling. *J. Chem. Phys.* **2007**, *126* (1).
- (187) Parrinello, M.; Rahman, A. Polymorphic Transitions in Single Crystals: A New Molecular Dynamics Method. *J. Appl. Phys.* **1981**, *52*, 7182.
- (188) Essmann, U.; Perera, L.; Berkowitz, M. L.; Darden, T.; Lee, H.; Pedersen, L. G. A Smooth Particle Mesh Ewald Method. *J. Chem. Phys.* **1995**, *103* (19), 8577–8593.
- (189) Hess, B.; Bekker, H.; Berendsen, H. J. C.; Fraaije, J. G. E. M. LINCS: A Linear Constraint Solver for Molecular Simulations. *J. Comput. Chem.* **1997**, *18* (12), 1463–1472.
- (190) Miller, B. R.; McGee, T. D.; Swails, J. M.; Homeyer, N.; Gohlke, H.; Roitberg, A. E. MMPBSA.py: An Efficient Program for End-State Free Energy Calculations. *J. Chem. Theory Comput.* **2012**, *8* (9), 3314–3321.

Curriculum Vitae

Alberto Cingolani

Nationality: Italian

Date and place of birth: 16.01.1990, Milano (IT)

Private Contact: afcingolani@gmail.com

Education

- | | |
|----------------------|---|
| Sep.2014 – current | PhD studies at the Institute for Chemical and Bioengineering, ETH Zurich
<i>Thesis: Morphology Control of Porous Polymeric Materials via Primary Particle Architecture</i> |
| Sep. 2012 – Jul.2014 | Master's Degree in Chemical and Bioengineering at ETH Zurich
<i>Thesis: Production of Cyclic Polyethylene Furfural Monomers for Ring Opening Polymerization</i> |
| Sep. 2009 – Jul.2012 | Bachelor's Degree in Chemical Engineering at Politecnico di Milano |
| Sep. 2004 – Jun.2009 | High School Diploma, Liceo Scientifico "F. Severi", Milano |

Publications

R. Ferrari, A. Cingolani D. Moscatelli. Solvent Effect in PLA-PEG Based Nanoparticles Synthesis through Surfactant Free Polymerization, *Macromolecular Symposia* **2013**, 324, 107-113.

A. Cingolani, D. Cuccato, G. Storti, M. Morbidelli. Control of Pore Structure in Polymeric Monoliths Prepared from Colloidal Dispersions, *Macromol. Mater. Eng.* **2017**, 1700417

S. Caimi⁴, A. Cingolani⁴, B. Jaquet⁴, M. Siggel, M. Lattuada, M. Morbidelli. Tracking of fluorescently labeled polymer particles reveals surface effects during shear-controlled aggregation, *Langmuir* **2017**, Article ASAP

A. Cingolani, D. Baur, S. Caimi, G. Storti, M. Morbidelli. Preparation of Ultra-Perfusive Chromatographic Materials via Shear-Induced Reactive Gelation, *submitted*.

⁴ Equal contribution

Conferences

A. Cingolani, G. Storti, M. Morbidelli. Shear-induced Reactive Gelation: synthesis of perfusive macro-porous materials, *Ion Chromatography Conference Herisau*, Metrohm International Headquarters, Herisau, Switzerland, 1 - 3 July 2015 (invited lecture).

A. Cingolani, S. Caimi, G. Storti, M. Morbidelli. Macro-porous materials by controlled aggregation of colloidal polymer particles, *EuroMOF2015 - 1st European Conference on Metal Organic Frameworks and Porous Polymer*, Kongresshotel Potsdam am Templiner See, Germany, 11 - 14 October 2015 (poster presentation).

A. Beltzung, A. Cingolani, H. Wu, G. Storti, M. Morbidelli. Porous polymer materials by reactive gelation: from preparation to applications, *Pacifichem 2015*, Honolulu, USA, 15-20 December 2015 (poster presentation).

A. Cingolani, M. Lorenz, S. Caimi, G. Storti, M. Morbidelli. Synthesis of macro-porous materials by controlled aggregation of colloidal polymer particles, *ECIS 2016 - 30th Conference of the European Colloid and Interface Society*, Università di Roma “La Sapienza”, Rome, Italy, 4 – 9 September 2016 (poster presentation).

M. Lorenz, A. Cingolani, G. Storti, M. Morbidelli. Synthesis of macro-porous materials for purification of therapeutic proteins via controlled aggregation of colloidal polymer particles, *Single-use Technologies II: Bridging Polymer Science to Biotechnology Applications*, Tomar, Portugal, 7 – 10 May 2017 (poster presentation, awarded participation).

M. Lorenz, A. Cingolani, G. Storti, M. Morbidelli. Synthesis of macro-porous materials for purification of therapeutic proteins via controlled aggregation of colloidal polymer particles, *PREP 2017*, Philadelphia, PA, USA, 16-19 July 2017 (poster presentation).

S. Caimi, A. Cingolani, B. Jaquet, M. Morbidelli, M. Lattuada. Tracking of fluorescently labelled polymer particles reveals surface effects during shear-controlled aggregation. *ECIS 2017 - 31th Conference of the European Colloid and Interface Society*, Madrid, Spain, 3-8 September 2017 (oral presentation).